University of Stavanger

Faculty of Science and Technology

MASTER'S THESIS

Study program/Specialization: Petroleum Geosciences Engineering	Spring, 2019 Open
Writer: Subhankar Choudhury	
Faculty supervisor: Arild Buland External supervisor: Ole Johannes Rossebø	
Title of thesis: Reservoir Characterization of the Snorre field: A pseudo wells based inversion approach	
Credits (ECTS): 30	
Keywords: Colored Inversion, Extended Elastic Impedance, Rock Physics, Pseudo-wells, One Dimensional Stochastic Inversion	Pages: 141 Stavanger, June 14,2019

Reservoir Characterization of the Snorre Field:

A pseudo wells-based inversion approach

by

Subhankar Choudhury

MSc Thesis

Presented to the Faculty of Science and Technology

University of Stavanger

2019

Acknowledgements

We are very grateful to Cegal for providing the application ODiSI, and to Equinor and other license partners for the dataset.

I take this opportunity to express my heartfelt gratitude and regards to my first supervisor Arild Buland for excellent guidance through various challenges that I encountered during the thesis. I am also grateful to my second supervisor Ole Johannes Rossebø for his exemplary guidance, monitoring and constant encouragement throughout the course of this project.

I also take this opportunity to express a deep sense of gratitude to Bruce Chalmers, Richard Neale and Lisa Casteleyn for their cordial support, valuable information and guidance, which helped me in completing this task through various stages.

I appreciate the support from family and friends, while working on this thesis.

Reservoir Charcterization of the Snorre Field: A pseudo wells based inversion approach.

Subhankar Choudhury[1], Arild Buland[2], Ole Johannes Rossebø[3]

1: Department of Energy Resources, University of Stavanger,4036 Stavanger, Norway

2: Equinor ASA, Forusbeen 50, 4035, Stavanger, Norway

3: Cegal AS, Vestre Svanholmen 4, 4313 Sandnes, Norway

Abstract

Complex reservoirs make hydrocarbon exploration challenging, and therefore improvement of methods for discovering and producing hydrocarbons is desired. Consequently, various seismic inversion algorithms have been developed to provide better characterization of the reservoir. One Dimensional Stochastic Inversion (ODiSI) is one such method that has been applied in the study which inverts seismic data by matching to large number of pseudo wells.

Inversion studies have been applied to a producing sandstone field, with the objective to improve the reservoir characterization and acquire accurate estimations of facies and reservoir properties together with the associated uncertainities. The study area is the Snorre field in the Norwegian sector of the North Sea. The reservoir has complex geology due to presence of several large fault blocks and is grouped into various zones containing sandstones of the Statfjord and Lunde Formations. The reservoir is highly heterogeneous with varying reservoir quality (i.e. net to gross, porosity).

The inversion study includes building pseudo wells which essentially encompasses an acceptable sampling of the area of interest. Lithofacies columns are populated using geologically realistic bed-thickness distributions. Each pseudowell is built with a full suite of well log curves generated from a rock physics model. The rock physics model/trend depends on porosity depth trends, moduli relationships and velocity trends from calibration well. In addition, seismic data are color inverted to be accepted as input for the inversion process. Synthetics based on Extended Elastic Impedance are used in the matching process. Finally, inversion is carried out resulting estimates of facies probabilities and reservoir properties.

Only one well containing S-sonic functions as the calibration well. Based on rock physics analysis, it is observed that the reservoir and non-reservoir facies is distinguishable in impedance domain. Different combinations of color inverted chi angle stacks such as near-mid and mid-far were used as an input. The blind well predictions were considerably accurate. However, predictions in mid-far combination came out to be more consistent in comparison to that of near-mid.

In addition, the study illustrates the quality of algorithm which generates laterally stable results.

Table of contents

List of tables

List of figures

1. Introduction

The process of reservoir characterization encompasses the integration of seismic data with other forms of data including well log data, rock physics models, and geological models. A key factor to consider when integrating various data is uncertainty. Assigning uncertainties to all the data helps in estimating a better probabilistic result. Therefore, proper weighting is necessary to avoid any sort of bias. Data with low uncertainty should be weighted up; data with high uncertainty should be weighted down.

Probabilistic seismic inversion algorithms based on Bayes' theorem initiated in the early 2000's (Buland and Omre, 2003; Gunning and Glinsky, 2004) and were continuously improved within academia and oil companies (Leguijt, 2009; Grana and Della Rose, 2010; Riise et al., 2012; Connolly and Hughes, 2016; Connolly and O'Brien, 2017).

In the past decade, single step inversion methods, also known as petrophysical inversion, in which reservoir properties are estimated directly, have been preferred (e.g. Bosch et al., 2009) over a two-step process of initially estimating elastic properties and then mapping these to reservoir properties. These two approaches have been combined (Buland et al., 2008) and have become more widely accessible (Riise et al., 2012; Kemper and Gunning, 2014; Connolly and O'Brien, 2017).

Connolly and Hughes (2016) describe an approach which can estimate facies probabilities and reservoir properties with associated uncertainties within what can be interpreted as a Bayesian framework known as One Dimensional Stochastic Inversion (ODiSI). This approach has been applied in many fields globally with proven results (Grant and Zheng, 2016).

1.1 Aim of the Study

The aim of this study to improve reservoir characterization of the Snorre field through a one-dimensional stochastic inversion (ODiSI).

1.2 Objectives

The objectives of the study are as follows:

- Develop the geological/elastic understanding of the area by performing a rock physics study.
- Estimation of reservoir properties through inversion such as net to gross and lithofacies probability.
- Examine if this approach is beneficial in understanding uncertainities in general.
- Examine if this approach improves reservoir characterization of the Snorre field and in general fluvial reservoirs.

1.3 Background literature

Seismic reservoir characterization is a method to estimate reservoir properties, such as net to gross and porosity directly from seismic data. The shortcomings of deterministic inversions have been well documented (Francis 2006a, 2006b) and it is recommended to avoid the bias introduced by building low frequency models from sparse well data (Grant, 2013). The output of deterministic inversions is only a mean estimation of a reservoir property and it often neglects the importance of quantifying associated uncertainties (Grant and Zheng, 2016).

Stochastic inversion methodologies in reservoir characterization have become more popular in recent years (Ayeni et al., 2008; Bosch et al., 2010; Connolly and Hughes, 2013). Many different approaches have been proposed, such as optimization techniques

(Bosch et al., 2009; Grana et al.,2012) while others are based on Markov chain Monte Carlo (MCMC) methods (Larsen et al., 2006, Ulvmoen and Omre, 2010, Rimstad et al., 2012).

ODiSI is a pragmatic process where the estimation process is stochastic in a clear and conceptually simple way. This inversion method has several distinctive characteristics in comparison to routine stochastic inversion methods. Firstly, lateral statistics are not included in the prior model, which prevents bias. Secondly, the trace matching process is one dimensional, operating on one trace separately. Constraints on spatial correlation are provided by the seismic data in this method. This restricts the maximum frequency to that of the seismic data and makes the algorithm highly parallelizable which allows larger datasets to be inverted in a time-effective manner. In addition, it is a joint inversion scheme, which provides reservoir properties and litho-facies as outputs. It is also simultaneous in the sense that multiple volumes of seismic angle stacks may be used in the inversion to fully exploit the amplitude variation with offset (AVO) information (Grant and Zheng, 2016).

ODiSI has been applied to several fields globally; it has been applied in a field in the Nile delta (Figure 1.1) with the aim of providing net to gross volume to help in well planning and improve the volumetric estimates during the field development stage (Grant and Dutton, 2016). In addition, it was applied in a field offshore West Africa, where the prior was built using one well, but good results were acquired in blind well locations (Connolly and Hughes 2016).

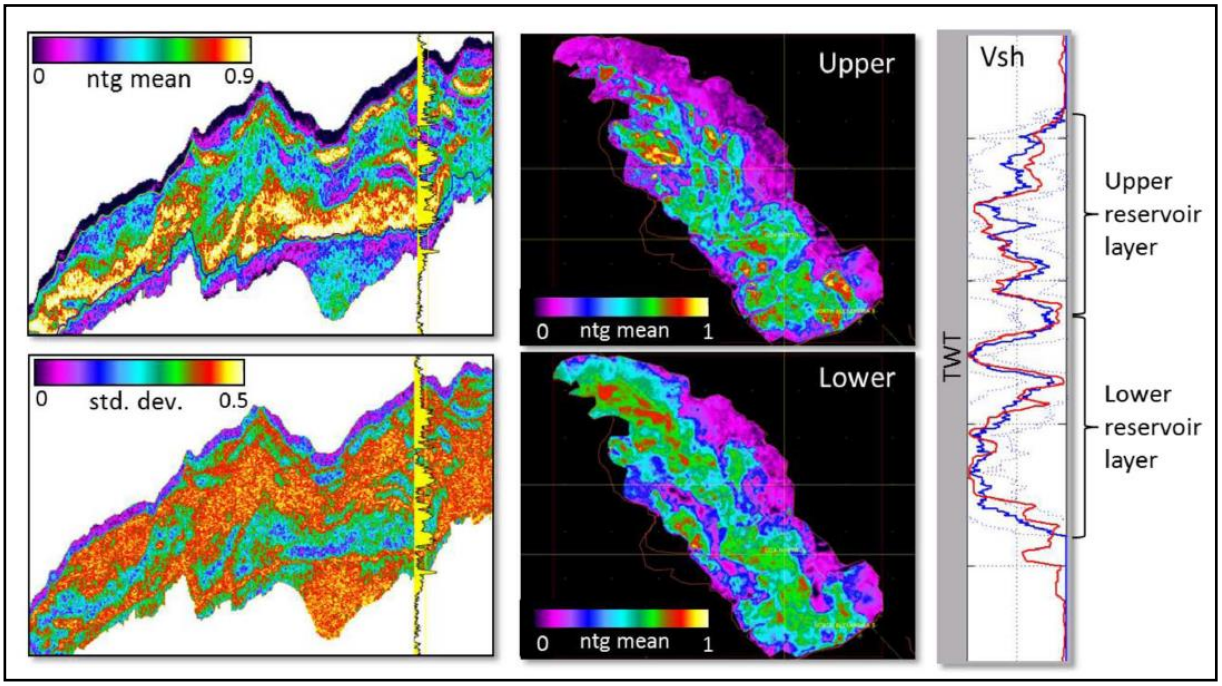

***Figure 1.1**: Predicted net to gross of a field in west Nile delta. Figures on the left show the mean NtG and standard deviation output along a section; figures in the middle show the average NtG maps over the two reservoir intervals; figure on the right shows the match between smoothed measured Vsh log (red) and inverted means Vsh (solid blue) with its standard deviation (dotted blue). Grant and Dutton (2016).*

2. Geological setting

This chapter provides a brief overview of the regional geology and structural evolution of the Snorre field, including the description of the reservoir of the field.

2.1 Regional geology and structural evolution

The North Sea is an intracratonic basin with a complicated tectonic and geological history (Figure 2.1; Figure 2.2). The evolution of the North Sea can be broadly classified into five primary events, the Caledonian geosyncline during the Cambrian-Silurian; the Variscan geosyncline, during the Devonian-Carboniferous; an

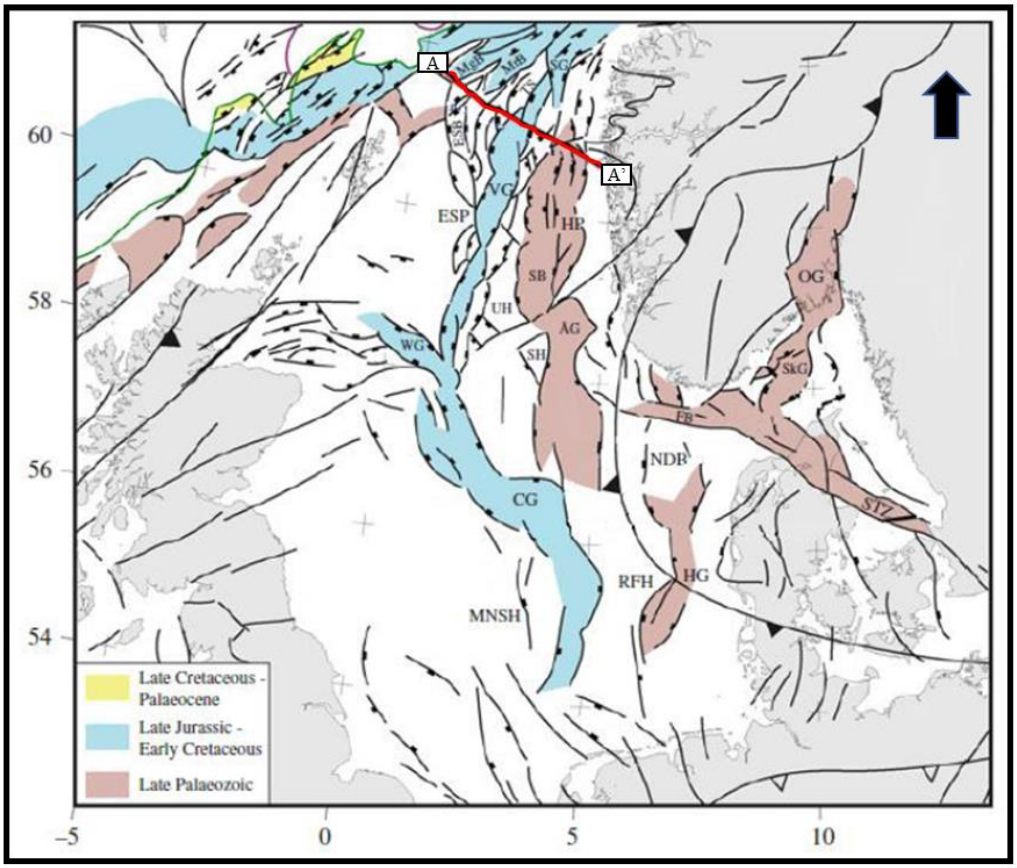

***Figure 2.1**: The major structural elements of the northern North Sea and adjacent areas. Adapted from Faleide et al. (2015); Hameed (2016).*

intracratonic stage during the Permian-Triassic; rifting during the Jurassic-Cretaceous; and post-rifting during the Cenozoic (Ziegler, 1975).

2.1.1 Carboniferous-Permian

The North Sea was majorly affected by principal episodes of rifting and thorough volcanism during the Carboniferous-Permian times (Figure 2.2). The extension resulted the deposition of reddish sandstones of the Rotliegend Group, which were of eolian and fluvial origin (Figure 2.4; Halland et al., 2013).

2.1.2 Triassic

Subsequent to the Permian rifting, there was an episode of regional subsidence that existed during most of the Triassic and to the Lower Jurassic (Figure 2.2; Figure 2.4). Huge amounts of sediments associated with the Hegre Group were concentrated in the subsiding continental basin throughout the Triassic. The Hegre Group, in particular, contains fluctuating intervals of interbedded sandstones, shales, claystones, and mudstones associated with sequences of mainly sandstone or shale. It is categorized by

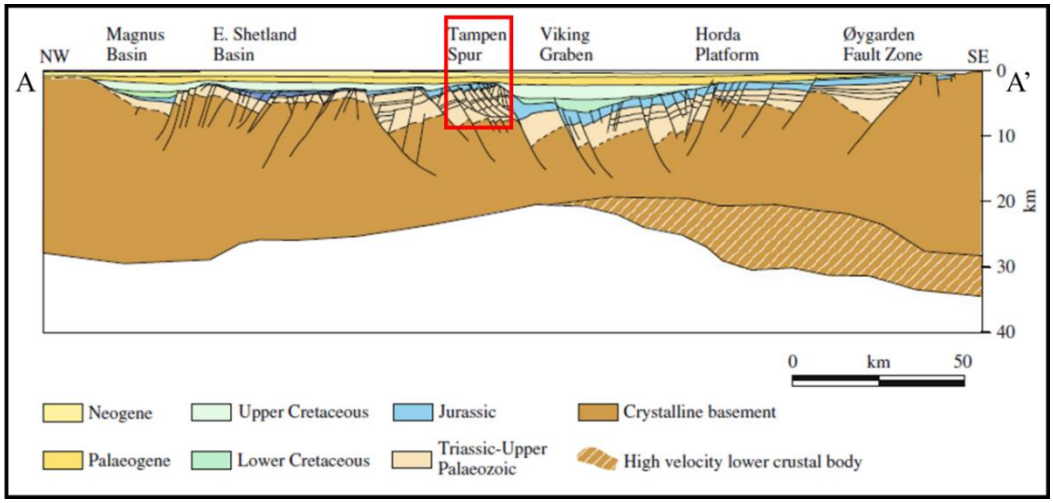

***Figure 2.2**: Regional seismic profile from northern North Sea area., location of the seismic line is highlighted on Figure 2.1 (Red line). The line is interpreted by Christiansson et al. (2000) and cited in Faleide et al. (2015). Study area is highlighted on figure. Adapted from Faleide et al. (2015); Hameed (2016).*

three formations; the Teist Formation, the Lomvi Formation, and the Lunde Formation (Dahl et al., 1993; Lervik 2006; Thorgersen, 2011).

2.1.3 Jurassic

The subsidence subsequent to the Permian rifting in the Triassic proceeded into the Lower Jurassic with a decline in the rate of subsidence. The sands of the Statfjord Formation are collected as braided stream deposits on an alluvial plain (Nystuen et al., 1989). Succeeding marine transgression placed the Dunlin Group over the Statfjord Formation, where the latter comprised of shallow marine siltstones and shales.

During the Middle Jurassic, the cooling of the crust post rifting attained thermal equilibrium and the Brent delta evolved and spread northwards into the marine basin (Dahl et al., 1993; Thorgersen, 2011).

A second dominant rifting episode commenced during the end of the Middle Jurassic (Figure 2.4). The rifting resulted in the thinning of the crust which was succeeded by syn-rift subsidence, leading to the formation of the Viking Graben. The syn-tectonic marine shales in Heather Formation were deposited in relative sea-level rise period. The crustal extension of the Middle Jurassic not only affected the easterly dipping faults of North-northeast (NNE) - South-southwest (SSW) to North East (NE) - South West (SW) orientation, but also reactivated the N-S striking faults (Figure 2.2). During this period, the Snorre Fault Block was rotated in southwest direction, and the crest of the block was uplifted above the erosive base. In addition, the pre-rift sediments were eroded in the northern part of the Snorre Field and the Triassic sediments of the Lomvi Formation were directly overlain by Cretaceous sediments. The Viking Group primarily encompasses marine mudstones of the Heather and Draupne Formation (Dahl et al., 1993; Thorgersen, 2011; Figure 2.4).

2.1.4 Cretaceous

During Lower Cretaceous, uplift and a relative sea-level drop resulted in exposure of newly deposited sediments to erosion. The succeeding marine transgression caused the Snorre Fault Block to be enwrapped by the carbonate sediments of the Lower Cromer Knoll Group.

During Upper Cretaceous, shales of the Lower Shetland Group were deposited. The deposition of the Upper Shetland Group took place after the hiatus of Santonian age. Most of the topography of the Snorre Fault Block was covered with sediments during the end of the Cretaceous (Dahl et al., 1993; Thorgersen, 2011).

2.1.5 Tertiary

During Tertiary, the fault activity persisted along the Inner Snorre Fault, in addition to NW-SE faults. Further, a minor interruption in subsidence of the basin due to a short episode of uplift and erosion, resulted in the deposition of the Rogaland and Hordaland Group. There was a decline in fault activity in Tertiary, and seismically detectable faults were absent in the area from Oligocene. A prime episode of relative uplift and erosion in the Miocene was succeeded by deposition of sands of the Utsira Formation of the Nordland Group (Dahl et al., 1993; Thorgersen, 2011)

2.2 Snorre Field:

Snorre Field is a producing oil field situated on the Tampen Spur area in the Norwegian sector of the northern North Sea (Figure 2.3). The field is located in block 34/4 and 34/7.

The Snorre field comprises of several large fault blocks in the reservoir zone (Smith et al., 2001). The first drilling activity in Snorre field took place in 1979 and oil was

discovered in Lunde Formation (Jorde and Diesen, 1990). The current owners of Snorre field are Equinor Energy ASA (33.27%, operator), Petoro AS (30%), ExxonMobil (17.44%), Idemitsu Petroleum Norge AS (9.60%), DEA Norge AS (8.57%), Vår Energy AS (1.10%) (Norwegian Petroleum Directorate (NPD), 2019).

2.3 General Stratigraphy of the Snorre field reservoir

The fundamental reservoir formations in the Snorre field are Triassic Lunde and Jurassic Statfjord Formations of the Hegre Group (Figure 2.4; Caillet, 1993). The reservoir interval in the Snorre field is approximately 1300 meters (Hollander, 1987). Lunde Formation is the main reservoir unit in the Snorre field with almost 75 % of the total hydrocarbons with the remaining found in the Statfjord Formation (Horstad et al., 1995). The Lunde Formation is classified into Lower, Middle and Upper members (Hollander, 1987; Nystuen and Fält, 1995; Nystuen et al., 1989). A general overview of the reservoir formations is discussed in the following sections.

2.3.1 Hegre Group

The Hegre Group belongs to the Triassic age (Figure 2.4). The Hegre Group contains interbedded sandstones, claystones and shales together with sequences of largely sandstone or shale/claystone (Lervik, 2006). The Hegre Group is separated into three formations: Teist Formation in the base, Lomvi Formation in the middle and Lunde Formation on the top (Hameed, 2016; Figure 2.4).

Lunde Formation

As previously mentioned, Lunde Formation is the principal reservoir unit in the Snorre field. Vollset and Doré, (1984), proposed that the Lunde Formation is of continental

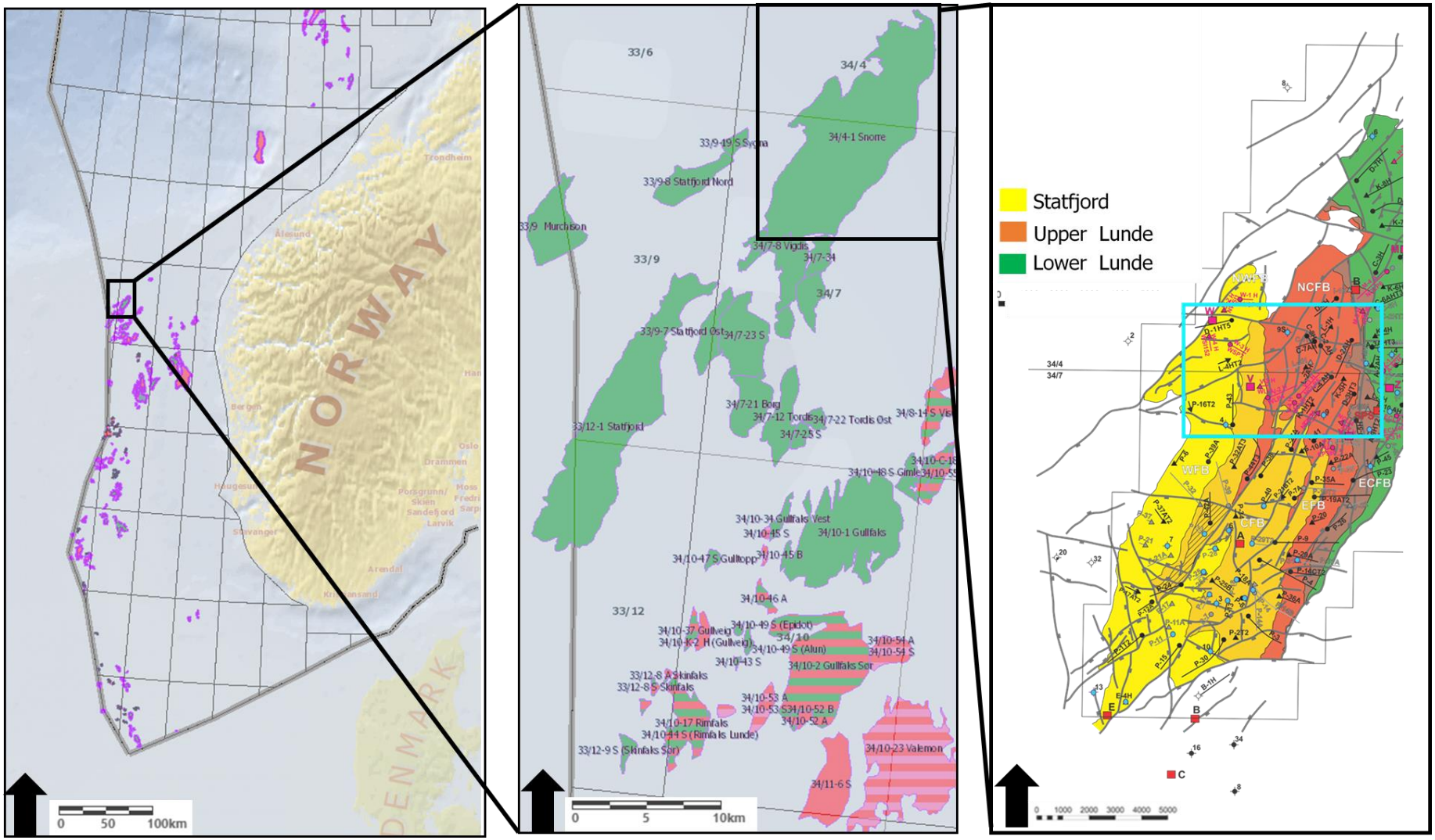

***Figure 2.3**: Location of the study area in Snorre Field. Adapted from NPD (2019) and Byberg (2009).*

origin and accumulated in lacustrine and fluvial environments containing interbedded sequences of very fine to coarse grained sandstones, claystones, marls and shales. The Lunde Formation is grouped into three units: Lower, Middle and Upper members (Jorde and Diesen, 1990; Nystuen and Fält, 1995). The Lower and Middle members contain claystones, mudstones and fine-grained sandstones while the upper member is abundant in fluvial channel sandstones except the uppermost part which is dominated by mudstone (Nystuen and Fält, 1995; Hameed, 2016).

2.3.2 Statfjord Formation

The Statfjord Formation contains fluvial sandstone and mudstone deposited via braided river on alluvial plain (Jorde and Diesen, 1990). The bottom part of Statfjord Formation has great similarity with the upper part of Lunde Formation and displays gradational change (Jorde and Diesen, 1990). The topmost part of the Statfjord Formation contains coarse grain glauconitic sandstone with marine fossils which advocate a shallow marine environment (Nystuen and Fält, 1995; Vollset and Doré, 1984; Hameed, 2016). The Base cretaceous unconformity (BCU) truncates the upper member of the Lunde formation and the Statfjord formation in the northern and eastern part of the field. (Seldal et al., 2008; Byberg, 2009).

2.4 Reservoir Description of the Snorre field

The Snorre (SN) reservoir has been divided into various zones based on a conceptual geological model. (Seldal et al., 2008; Byberg, 2009; Thorgersen, 2011). Detailed description of the various zones is discussed in the following sections.

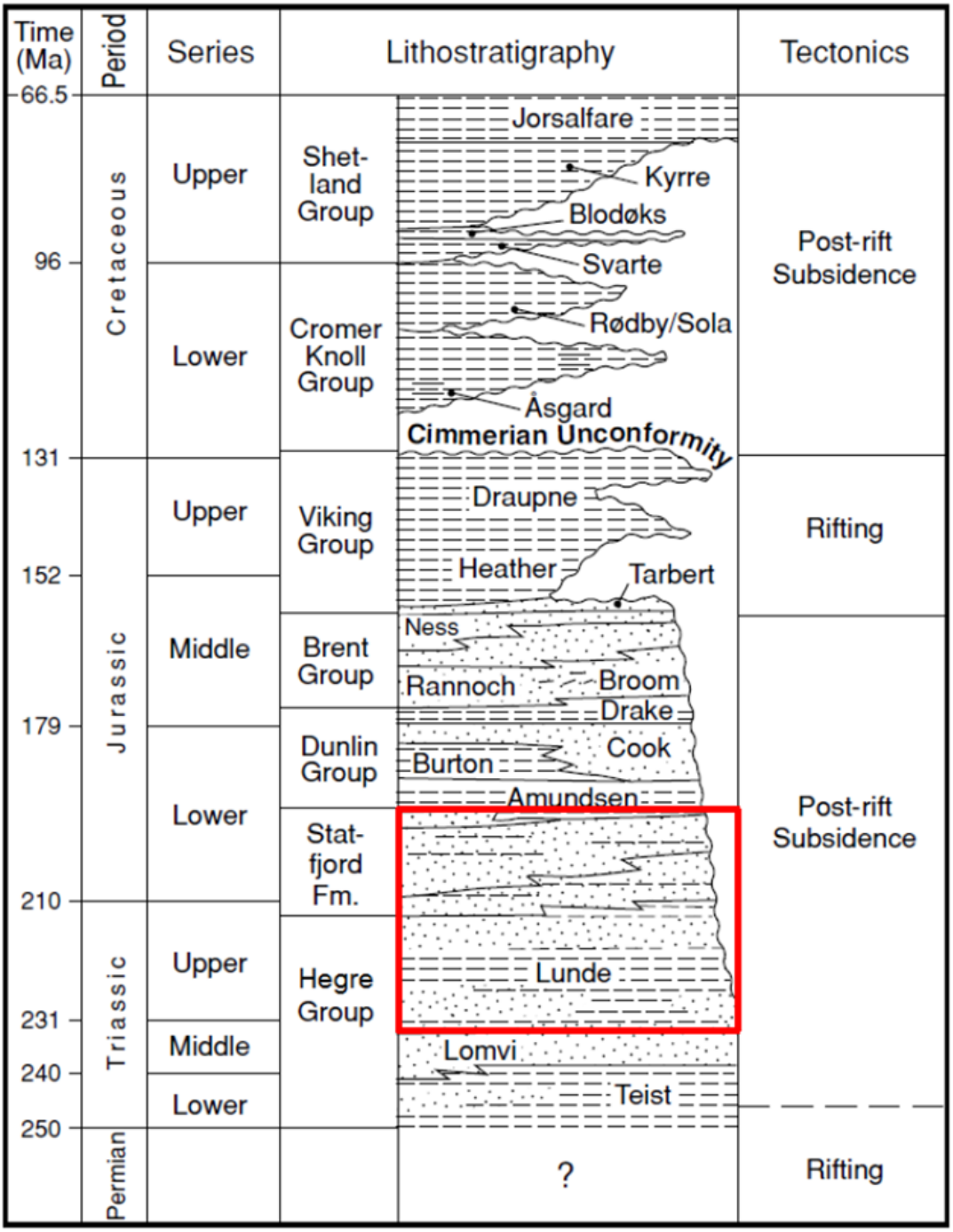

***Figure 2.4**: General stratigraphy of Tampen Spur area. Reservoir formations of the Snorre field are highlighted. Adapted from Ketzer et al. (2002)*

The Upper Member of the Lunde Formation (SN1-SN10.3)

The Upper Member of the Lunde Formation is categorized into ten reservoir zones (SN1- SN10.3) in the stratigraphic model of the Snorre reservoir (Figure 2.5). These zones are further sub-divided into smaller sub-zones. This formation contains interbedded, medium grained, white, pink or grey channel belt sandstones. Additionally, the sandstones are interbedded with red brown to green caliche-rich siltstones and mudstones of continental origin. (Seldal et al., 2008; Byberg, 2009; Thorgersen, 2011).

SN1-SN7: Braided Channel Systems on Upper Alluvial Plain

The zones SN1-SN7 contains channel sandstones accumulated in braided shallow channels (Figure 2.5). The dimension of these sandstones alters vertically, but nearly all are in the fine to medium range. Fining upward units, vertically stacked sandstone bodies and coarse-grained channels are also frequent in these zones (Seldal et al., 2008; Byberg, 2009; Thorgersen, 2011).

SN8-SN10: Meandering Channel and Distributary Channels on Lower Alluvial Plain.

The channel sandstones in SN8 – SN10 are understood to have accumulated in an environment dominated by meandering and distributary channels (Figure 2.5). The meandering channels are extremely sinuous and accumulate most of the bed load in the inside of the meander curves. The principal channel on the lower alluvial plain is likely to be separated into multiple distributary channels as it is moves towards the upper delta plain. The distributary channel sandstones are represented by low sinuosity and appear frequently in the upper part of SN9 (SN9.3 and SN9.4) and SN10 (SN10.2, SN10.3 and SN10.4) (Seldal et al., 2008; Byberg, 2009; Thorgersen, 2011).

The Statfjord Formation in the stratigraphic model (SN10.3-SN11)

The Statfjord Formation is categorized into one prime reservoir zone (SN10.3-SN11) in the stratigraphic model. The Statfjord Formation includes more carbonaceous silt and mudstones, which point towards a more coastal plain depositional setting. The net to gross increases upwards with primarily meandering fluvial sequences progressing upwards into braided stream deposits in the Statfjord Formation. The sandstones in the Statfjord Formation contain coarser grains than that of in the Upper Lunde Member. Alterations in lateral thickness in the middle to upper part of the Statfjord Formation are also observed (Seldal et al., 2008; Byberg, 2009; Thorgersen, 2011).

SN11: Coastal Plain

The Statfjord Formation (SN11) contains highly permeable sandstones which are laterally continuous. The sandstones are understood to be gathered on the coastal plain, with a depositional environment containing embayment deposits, coastal plain channels and crevasse splays (Seldal et al., 2008; Byberg, 2009; Thorgersen; 2011).

2.5 Reservoir Properties of the Snorre field

Table 4.2 provides the average petrophysical properties of the previously mentioned zones in the Snorre reservoir. The available petrophysical properties are Net to Gross (NtG) and Density-Porosity (φD). The properties differ in various zones.

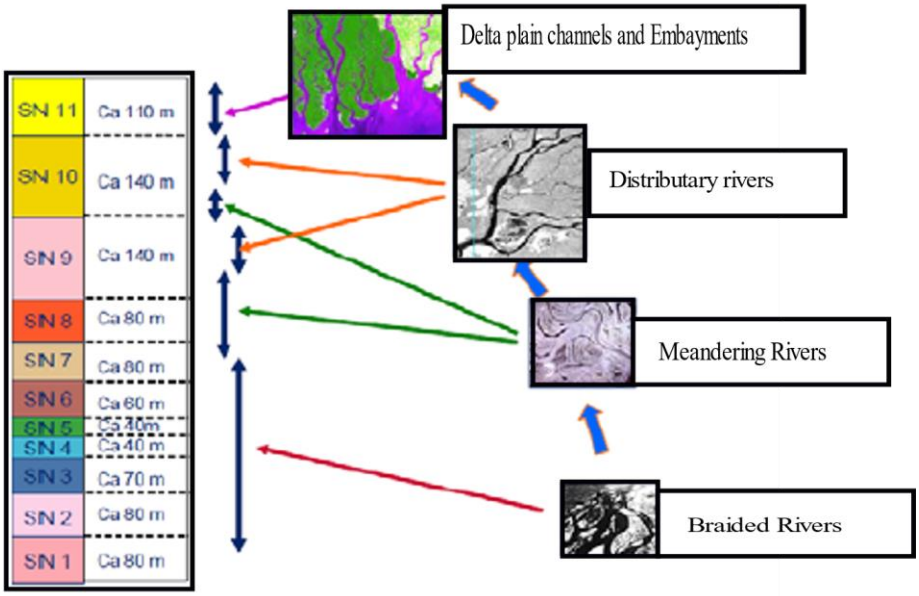

***Figure 2.5**: Depositional settings in different Snorre zones. Byberg (2009).*

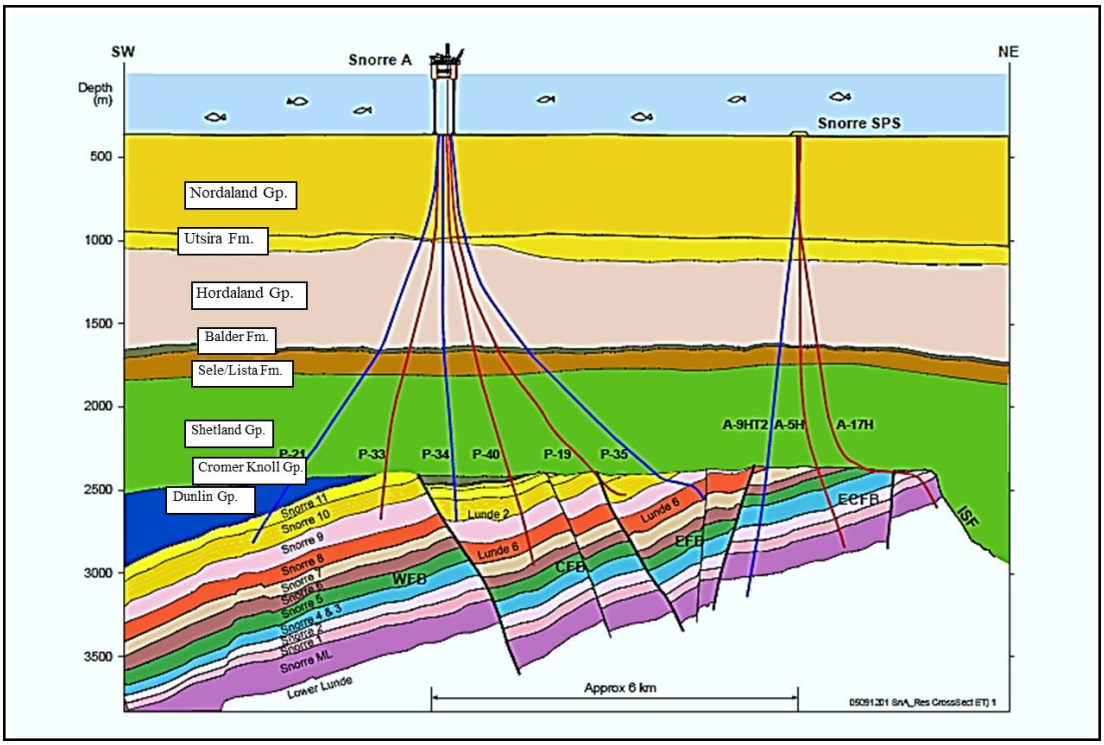

***Figure 2.6**: SW-NE crossection through the southern part of the Snorre Field Byberg (2009).*

***Table 1**: Petrophysical properties of the Snorre field (Seldal et al. (2008); Byberg (2009))*

Snorre Zones	NtG (%)	PHID(%)
SN 11	36	24
SN 10	21	24
SN 9	27	25
SN 8	42	24
SN 7	44	24
SN 6	47	23
SN 5	47	25
SN 4	52	24
SN 3	56	25
SN 2	54	25
SN 1	64	25
SN ML	21	21

2.6 Previous work on the Snorre field

An overview of the published seismic inversion studies on the Snorre field is given in this section.

Hansen and Magnus (1997) discussed the application of InverMod scheme to perform seismic inversion in the Snorre field to improve the reservoir characterization and well planning in the field. They conducted the study on the Statfjord formation in the Snorre field. They used a combination of density with either velocity or impedance in order to separate the reservoir and non-reservoir facies instead of conventionally using only impedance. A priori model was used as a basis for the inversion. They observed that the inverted section introduces further heterogeneity to the reservoir model, which also corresponded with the log. Although, one major heterogeneity in the top of the Statfjord Formation was not captured, possibly due to incorrect priori model for that area. In

general, the blind tests confirmed that the inverted model describes the reservoir better than the apriori model, and in some areas was able to predict well- resolved sand bodies with thicknesses as small as 5-10 m. However, some sands were inaccurately mapped due to several issues such as the use of incorrect horizon interpretations, varying petrophysical properties, low resolution, presence of noise in the seismic data set, and other effects. They concluded that InverMod technique is useful as a lithology predictor on the Snorre Field as several wells, drilled after inversion, quantified that this technique could successfully predict lithology from seismic data in the Snorre Field.

Dahle et al. (2008) performed geostatistical AVA (Amplitude vs. Angle) inversion for facies estimation in the Snorre field. Initially, they inverted the seismic data for elastic parameters using the Bayesian AVA inversion method of Buland et al. (2003). They established a relationship between the facies and seismic data by comparing filtered logs with facies logs, which together with elastic parameters from initial inversion was used to estimate the facies probabilities for the entire volume. Their results document that the prediction of facies shows good agreement with the well logs and the blind test showed that they were able to predict the major sands and shales, however, there were some alignment problems in the centre part of the log. They confirmed that the Bayesian AVA inversion approach is effective in order to obtain facies probabilities for geomodeling. They concluded that the algorithm was fast and handled the uncertainty in the inversion correctly.

3. Theory

This chapter provides a concise summary of the theory and concepts used in this thesis.

3.1 Seismic angle stacks

Acquisition of seismic data involves different receiver arrangements / different offsets. After exercising static and dynamic corrections, full stack seismic is produced by stacking the individual seismic traces. The changes in seismic amplitudes as a function of offset (AVO) can provide relevant information about the attributes of reservoir such as fluid and lithology. AVO analysis is typically carried out using different angle stacks (Figure 3.1), which are commonly stacked depending on their angle of incidence.

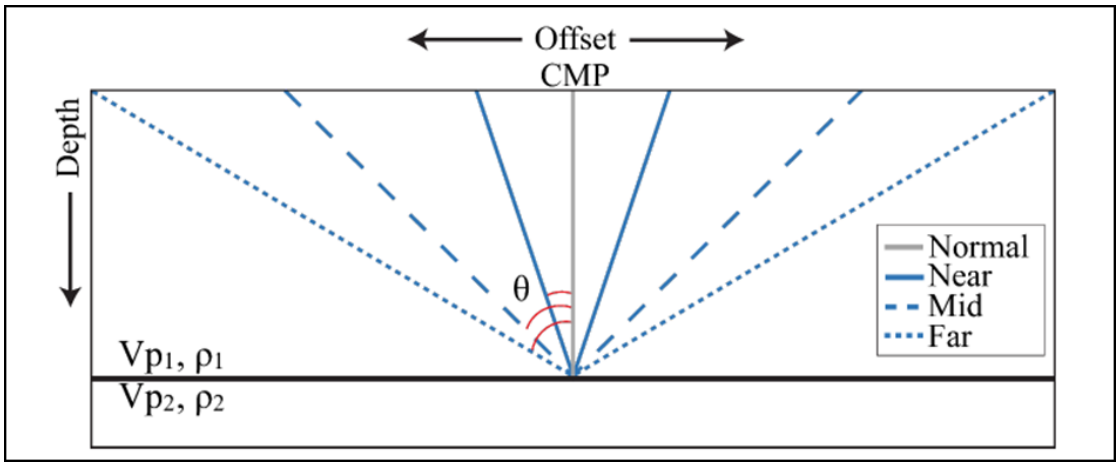

***Figure 3.1**: Schematic figure of reflected seismic waves. Different offset (near, mid, and far) corresponds to a different angle of incidence, θ. Tomasgaard (2018).*

3.2. Rock Physics

Seismic data provides knowledge of the subsurface, specifically rock type and pore content through travel time, reflection amplitude and phase variations. Numerous seismic properties such as P-wave velocity (Vp), S-wave velocity (Vs) and Density (Rho) are influenced by different factors such as pressure, temperature, porosity,

saturation and type of fluid (Wang, 2001). For better understanding of the subsurface, it is crucial to understand how these same factors reflect changes in the aforementioned properties. Rock physics brings together petrophysical, geomechanical, and seismic measurements which subsequently helps bridging the gap between the seismic properties and the elastic reservoir rock properties derived at the wells.

3.2.1. Elastic Moduli

The bulk modulus (K), shear modulus (μ) are elastic parameters that define the stress-strain relationships of rocks.

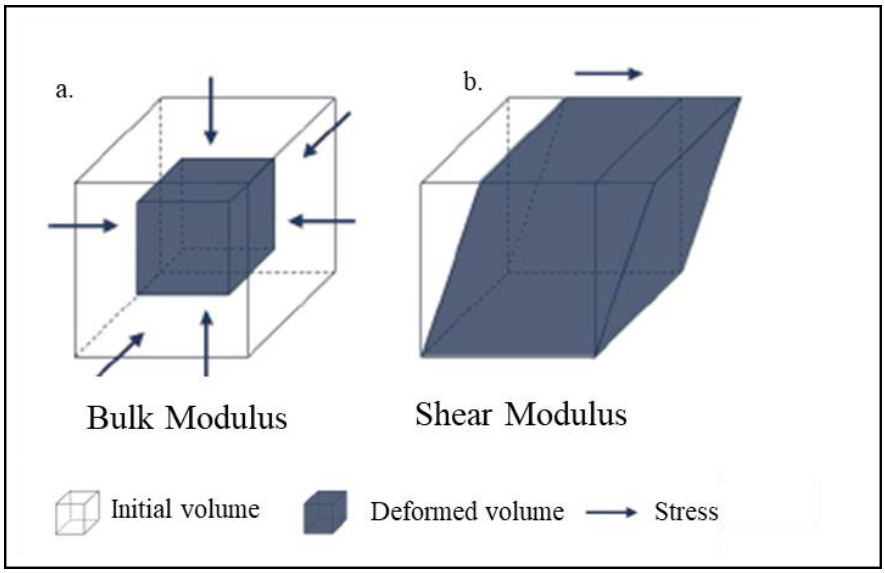

***Figure 3.2**: Elastic parameters. a) Bulk modulus, b) Shear modulus. Frette (2018)*

The bulk modulus (K) is defined as the ability of a material to resist change in volume under stress (Figure 3.2a). The Shear Modulus (μ) is defined as the ability of a material to resist shear deformations under stress (Figure 3.2b).

3.2.2. Seismic Velocity

The wave velocities of Primary/ Compressional (α) waves and Secondary/Shear (β) waves are expressed as:

$$\alpha = Vp = \sqrt{\frac{K + \frac{4}{3}\mu}{\rho}} \quad (1)$$

and

$$\beta = Vs = \sqrt{\frac{\mu}{\rho}} \quad (2)$$

where K, μ, and ρ are bulk modulus, shear modulus, and density, respectively.

3.2.3 Impedance

Elastic properties are usually discussed in seismic data via Acoustic Impedance (Zp) and Shear Impedance (Zs) in addition to density (ρ), where the acoustic impedance is:

$$Zp = \alpha\rho \quad (3)$$

and the shear (gradient) impedance is:

$$Zs = \beta\rho \quad (4)$$

3.3 Reflection coefficient

Reflectivity is influenced by factors such as incident angle of the propagating wave and the impedance variation at the reflection boundary. With regards to a normally incident wave, the reflection coefficient (Rc) is represented as:

$$R_c = \frac{Z_2 - Z_1}{Z_2 + Z_1} \quad (5)$$

where Z_1 and Z_2 are the impedances above and below the boundary respectively. In relation to a non-normal incident wave, a pair of P and S waves is reflected at the interface. The reflection coefficients for the two waves in such case are explained by the Zoeppritz's equations. These equations are complicated and unworkable in computations. Hence, the linear approximations were introduced.

3.3.1 Reflection coefficient approximation

The nature of seismic waves when reflected at an interface between two different geological layers is given by the Zoeppritz's equation. Numerous attempts to derive linear approximation for Zoeppritz's equation were made by several authors (e.g., Aki and Richards, 1980; Fatti et al., 1994; Shuey, 1985; Smith and Gidlow, 1987; Wang, 1999). The objective of the approximations was to simplify the perception of the cause and effect involved in variation of seismic amplitudes with offset. Aki and Richards (1980) approximation utilizes three different terms to discriminate rock properties into density, P-wave and S-wave velocities. Shuey (1985) modified the P-P reflection coefficient equation of Aki and Richards and arranged it in three terms as intercept (A), gradient (B) and curvature(C).

$$R(\theta) \approx A + B\,sin^2\theta + C\,sin^2\theta\,tan^2\theta \quad (6)$$

where θ is the angle of incidence. The Shuey three-term equation is also represented by the first two terms, which is credible for the incidence angle at which it diverges from the three-terms and the full Zoeppritz equation (Simm and Bacon, 2014).

$$R(\theta) \approx A + B\,sin^2\theta \quad (7)$$

In this study, the approximation given by Shuey (1985) has been used.

3.3.2 Intercept & Gradient

The reflection coefficient at zero offset ($R\ (\theta = 0) \approx A$) describes Intercept. It relies on the P-wave velocity and density of the layers above and below a boundary. The equation for intercept (A) is given by:

$$A = \frac{1}{2}\left(\frac{\Delta V_p}{V_p} + \frac{\Delta \rho}{\rho}\right) \tag{8}$$

The gradient (B) explains the change in reflection coefficient with incident angle (i.e., the rate of change of the curve in the $R(\theta) - \theta$ domain). It considers the S-wave velocity in addition to the P-wave velocity and density, and is given by:

$$B = \frac{1}{2}\frac{\Delta V_p}{V_p} - 4k^2\frac{\Delta V_s}{V_s} - 2k^2\frac{\Delta \rho}{\rho}, \quad k = \frac{V_s}{V_p} \tag{9}$$

It is visible from the above expressions, that the intercept and gradient is strongly linked with acoustic impedance and Vp/Vs ratio respectively. This suggests that the intercept is a measure of the relative difference in acoustic impedance across an interface between two layers, and the gradient is associated with the relative difference in Vp/Vs ratio (Tomasgaard, 2018).

3.4 Data Conditioning

Data conditioning steps are required to optimize the quality of pre and post-stack seismic data prior to use for impedance, amplitude versus offset (AVO) and seismic facies inversion applications. A master stack is defined, and the properties of the slave stacks are matched to the properties of master trace/stack. The data conditioning steps are as follows:

Phase matching: Non – linear phase differences between the master stack and the slave stack are being corrected in this step.

Amplitude spectra matching: In this step, the frequency bandwidth of the slave stack is made identical to that of the master stack.

Time Alignment: In this step, a chosen reflector is aligned on the slave stack to the corresponding reflector in the master stack

3.5 Seismic Inversion

As previously mentioned, seismic inversion is broadly classified into two types: deterministic and stochastic (Simm and Bacon, 2014). Several approaches for deterministic seismic inversion exist (e.g. recursive inversion, sparse spike inversion and model-based inversion). The scope of these approaches is discussed by Russell (1988). Seismic inversion is defined as the method of determining the elastic rock properties (e.g. acoustic impedance, shear impedance) from the seismic. Thus, the fundamental objective of inversion is to shift from the reflectivity domain of the seismic

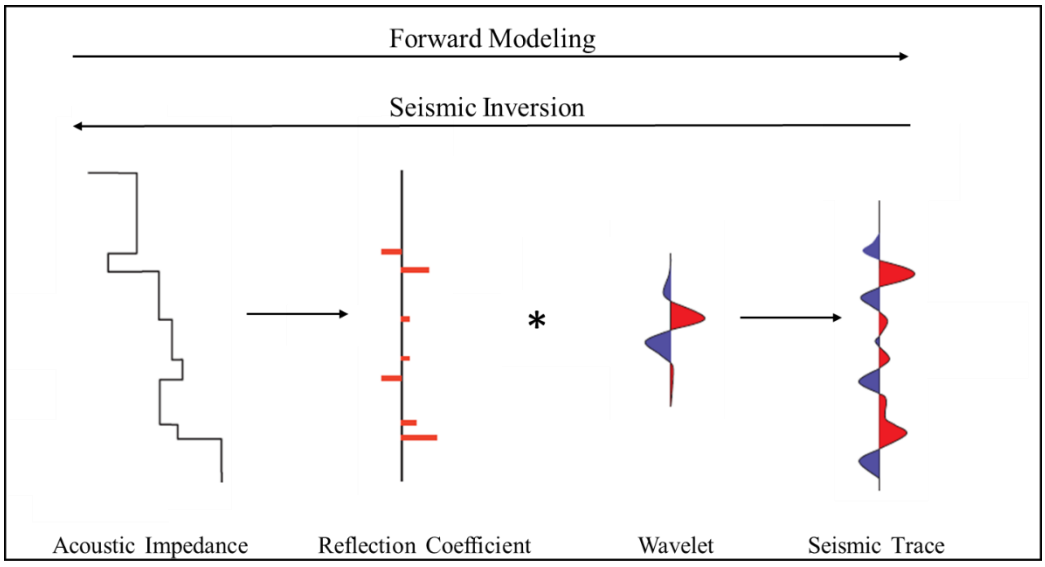

***Figure 3.3**: Process of forward modeling (left to right) versus seismic inversion (right to left) Frette (2018).*

to dependable estimates of layer elastic properties (Figure 3.3). The benefits of inverted data include more interpretable lithological and fluid/gas effects, attributed to the introduction of layers instead of reflections (Simm and Bacon, 2014).

3.6 Coloured inversion

Lancaster and Whitcombe (2000) introduced the method known as coloured inversion, which allows relatively quick and precise inversion of seismic traces. Colored Inversion is a combination of band limited trace integration together with shaping the amplitude spectrum.

3.6.1 Band-limited trace integration

Seismic data is normally band-limited, it lacks high and low frequencies, which are the primary concern with seismic inversion. It indicates that seismic data doesn't contain the information which is present in well data. Information about the absolute impedance values are not available in the seismic data. Thus, an integrated seismic trace provides a smooth form of the impedance.

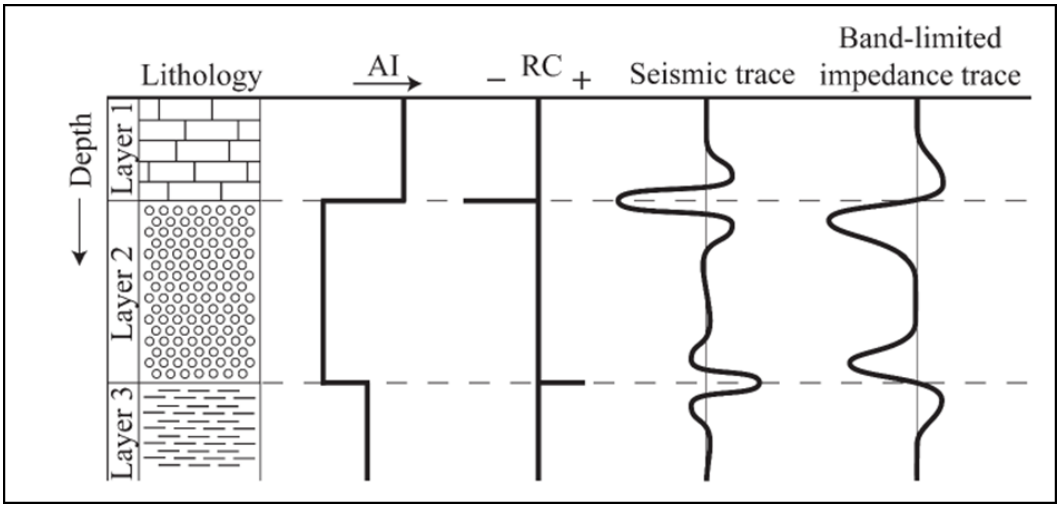

Figure 3.4: *Schematic illustration of how band-limited impedance relates to seismic data. Tomasgaard (2018).*

Figure 3.4 shows the relation of a band-limited integrated trace to impedance and seismic data. The change in layers is distinct on the zero-crossing in the band-limited impedance trace, although the seismic trace is zero-phase. This happens as a (-90°) phase rotation of the seismic data is applied in this process. In addition, it is also observed that the band-limited impedance tends to zero where there is absence of seismic signal, suggesting that the impedance of the entire layers is not properly captured. This is due to the absence of the low frequency components in the seismic data (Tomasgaard, 2018).

3.6.2 Operator

As already mentioned, trace integration jointly with shaping of the amplitude spectrum is known as Coloured Inversion. A band-limited model of the impedance of the earth is generated in the process. This is accomplished by acquiring the relative impedance from the seismic data with an amplitude spectrum alike the well log data within the seismic resolution (Simm and Bacon, 2014; Tomasgaard, 2018).

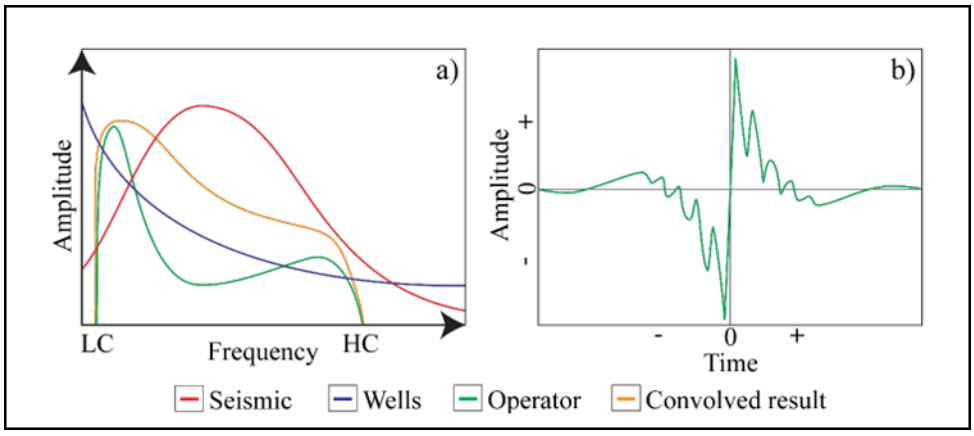

***Figure 3.5**: a) Schematic representation of the amplitude spectrum of a seismic cube, average well data, an operator, and a convolved result (i.e., the coloured inversion result). b) An illustration of an operator displayed in time. Modified after Lancaster and Whitcombe (2000), Tomasgaard (2018).*

Normally, the coloured inversion process involves convolution of the seismic data with an operator (Figure 3.5). The operator has a constant phase of (-90°), presuming that

the seismic data is zero-phase. The acoustic impedance spectrum of the earth is relatively constant at reservoir scale and can be computed by a trend line obtained from well log data. The operator is designed in such a manner that it guides the amplitude spectrum of the mean seismic response to follow this trend (Lancaster and Whitcombe, 2000).

3.7. Elastic impedance

Connolly (1999) brought in the concept of elastic impedance (EI) which was later normalized by Whitcombe (2002) by deriving acoustic impedance for non-normal incidence at a particular angle θ. This provided an approach for the inversion of angle stacks in addition to full-stack data (Frette, 2018).

3.7.1 Extended Elastic Impedance

Whitcombe et al., (2002) extended the EI concept to any angles by introducing extended elastic impedance (EEI). They substituted $\sin^2\theta$ by $\tan\chi$ in Shuey (1985) two-term equation (10), before calibrating this equation by $\cos\chi$, to approve any combination of the intercept and gradient as an add-on of the EI:

$$Rs\,(\chi) = A\,cos\chi + B\,sin\chi \qquad (10)$$

where Rs(χ) is scaled reflectivity, A and B are intercept and gradient, respectively, and χ (chi) is the angle of rotation in the A-B space (Figure 3.7). The calibrated reflectivity ranges from a value of A at $\chi = 0$ (zero incidence reflectivity) to a value of B at $\chi = 90^0$ (gradient reflectivity) (Whitcombe et al., 2002).

Whitcombe et al. (2002) illustrated that the EEI could be adapted (using different χ values) to make it approximate to elastic parameters (e.g. acoustic impedance, bulk modulus, Vp/Vs ratio, shear impedance and shear modulus).

Normally, the EEI method deals with finding an optimal rotation angle in the intercept-gradient (A-B) space (Figure 3.5), to provide the best correlation coefficient with a specific log (e.g. water-saturation, gamma-ray; Figure 3.7), and subsequently produce the equivalent intercept-gradient combination (i.e. the EEI) (Whitcombe et al., 2002).

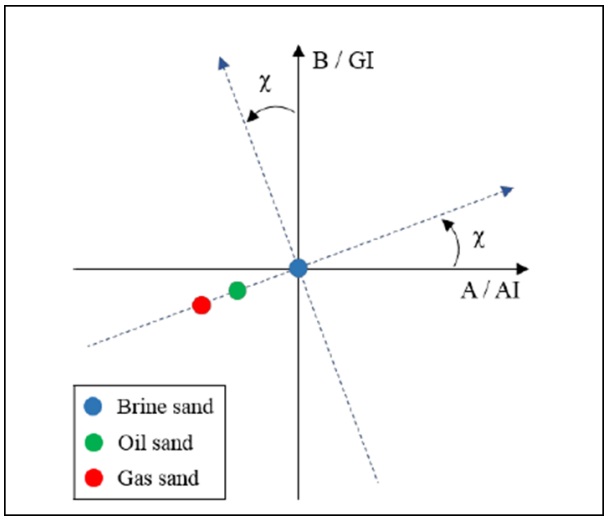

***Figure 3.6**: Rotation in the intercept-gradient (A-B) (or the impedance (AI-GI)) space using angle χ (chi). This particular rotation maximizes the distinction between brine, oil, and gas sands and is equivalent to the Smith and Gidlow (2003) crossplot angle. Modified from Simm and Bacon (2014), Frette (2018).*

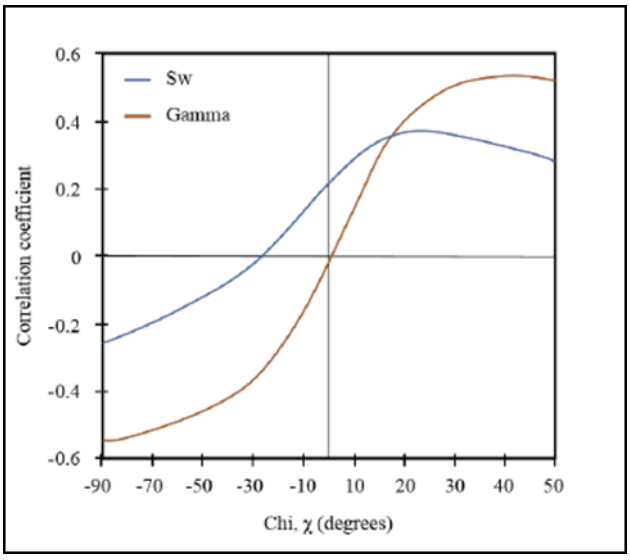

***Figure 3.7**: Correlation coefficient between EEI and gamma-ray and Sw (water-saturation) for a range (-90 to 90 degrees) of χ (chi) values. Modified from Whitcombe et al. (2002), Frette (2018).*

3.8 Bayesian framework

A Bayesian setting is an instinctive choice for many geophysical inverse problems (Buland and Omre, 2003). The posterior distribution p(**m/d**) can be represented using Bayes' theorem (Equation 15), where the prior model p(**m**) is combined with the information about **m** provided by **d** via the likelihood model.

$$p(\mathbf{m} \mid \mathbf{d}) = \frac{p(\mathbf{d} \mid \mathbf{m})\, p(\mathbf{m})}{p(\mathbf{d})}, \tag{11}$$

Where,

$$p(\boldsymbol{d}) = \int \ldots\ldots\ldots \int p(\mathbf{d} \mid \mathbf{m})\, p(\mathbf{m})\, d\mathbf{m}, \tag{12}$$

is the marginal density for **d,** it represents the observations and the unknown parameter vector is expressed by **m**.

3.9 Continuous Time Markov Chain (CTMC)

Markov processes with a continuous time parameter are more adequate for describing sedimentation than discrete time Markov chains as they treat sedimentation as a natural process that happens continuously (Rolke, 1991).

A stochastic process $\{X_t, t \geq 0\}$ is called continuous time Markov process with discrete state space *S*, provided that for any $t, s \geq 0$, and $j \in S$.

$$P\{X_{t+s} = j / X_u, u \leq t\} = P\{X_{t+s} = j \,/\, X_t\} \tag{13}$$

3.10 One Dimensional Stochastic Inversion (ODiSI)

ODiSI is a seismic inversion method which is reasonably simple, but it deals with seismic inverse problems in a robust manner. It follows a quasi-Bayesian framework.

$$p(\mathbf{m} \mid \mathbf{d}) \sim p(\mathbf{m})\, p(\mathbf{d} \mid \mathbf{m}) \tag{14}$$

Where p(**m**/**d**) is the posterior probability distribution containing the solution to inverse problems, p(**m**) is the prior distribution that contains the prior information about the model and p(**d**/**m**) is the likelihood distribution that calculates the data misfit (Grant, 2016; Connolly and Hughes, 2016).

The posterior estimates are not evaluated in this method, which makes it partly Bayesian (Grant and Zheng, 2016). This method is based on the practical approach explained by Connolly and Hughes (2016), where a combination of deterministic and stochastic components is used to approximate the Bayesian inference process. The prior model is defined based on a first order Markov chain. The samples are drawn from the prior model using a 1D Monte Carlo algorithm. The likelihood distribution is obtained through forward modelling using the convolutional model together with gaussian noise. The deterministic matching process is used to collect the best fitting samples which further helps in estimating the output reservoir properties (Grant and Zheng, 2016; Connolly and Hughes, 2016).

The inversion process is operated trace by trace. By sampling the prior model, a large number of pseudo wells are created at each trace location. A genuine Monte Carlo approach is used, to select independent samples from a prior distribution, and subsequently they are tested against the data to either being accepted or rejected. This contrasts with Markov chain Monte Carlo methods in which samples are correlated in

a way the outcome of each match impacts the next sample. One major issue with using Monte Carlo methods is that, the efficiency is compromised if the model space is large. However, the pseudowell approach attains optimal efficiency by putting constraints on the size and spatial dimensionality of the samples. Each sample is a reasonably short (<100ms) 1D vertical stratigraphic profile (Connolly, 2017). A continuous time Markov Chain (CTMC) model is used to simulate the pseudo well lithology columns. The vertical stacking order of the individual litho-facies in the pseudo wells are controlled by a transition probability matrix. The thickness of the beds is determined by sampling from the exponential distribution associated with each facies type, using a rate parameter. Synthetic petrophysical and elastic log suites for all the pseudo wells are determined using the empirically-derived rock property relationships together with Gaussian noise (Grant and Zheng, 2016).

Synthetic seismic traces are generated for each pseudo well, by convolving with a wavelet. In order to find the best match synthetic, the generated synthetic traces are compared against the input trace and indexed by the root-mean-square errors (RMSE). The pseudo wells with the lowest RMSE values are chosen for the particular trace location, and their associated logs are used to determine the mean and standard deviation of the chosen reservoir properties at that trace location. To reduce the RMSE, ODiSI fixes the small static differences by slightly shifting the traces up and down. In a simultaneous setting, two input seismic datasets produce two sets of RMSE. Depending on the relative importance in the inversion process, a weighting factor is applied to each input dataset. The final RMSE, after weighting, is used for selecting the best matching pseudo wells. The process behind the selection of the best pseudo wells is more dependent on the amplitude difference between the synthetic and real seismic

traces than the shape of the waveform when estimating reservoir properties. This process is performed on all the trace locations and it fetches a set of 3D volumes of mean reservoir properties and their associated uncertainties (Grant and Zheng, 2016).

3.10.1 The prior model

The prior model lays the foundation of the inversion; thus, it needs to be formulated properly. The primary tasks in building a prior model includes establishing appropriate rock property relationships and vertical layer statistics. The formation of the pseudo-well lithology columns is dependent on the layer statistics and the synthetic logs which are obtained from the rock property relationships (Connolly, 2017; Grant and Zheng, 2016).

Initially, the lithofacies can be categorized into three classes: reservoir, non-reservoir and an intermediate type based on assuming a binary lamination. The proportion and transition probability of each lithofacies is specified by analyzing the discrete lithology logs in each interval. In addition, a complementary cumulative distribution function (CCDF) is used to obtain a Lambda parameter (see chapter 3.10.2) which fits the observed bed thickness distribution for each litho-facies. The recurrence of litho-facies in the pseudo wells is dependent on the transition probabilities, while the lambda values affect the bed-thickness proportions.

Petrophysical data for each lithofacies is used to create their respective rock property relationships. Rock properties concerned with the reservoir type and non-reservoir type facies are established from various trends (see chapter 3.10.3). Individual fluid properties along with Gassmann's equation, provides saturated bulk modulus, which is further used to construct elastic profiles (Vp, Vs and density). The trends of Elastic

parameters for the non-reservoir class is derived directly from the input well-logs. There are uncertainties associated with each reservoir parameter and are introduced by Gaussian processes. (Connolly, 2017; Grant, 2016)

3.10.2 Pseudo wells:

Pseudo well contains a set of petrophysical and elastic logs (De Groot et al., 1996). The pseudo wells in ODiSI are based on the de Groot's definition. They are selected from a prior model represented by vertical statistics and rock physics trends. The different reservoir properties in the pseudo-well must include all the possibilities of vertical geological profiles that might be encountered in the reservoir. The area of interest is subdivided into a number of macrolayers likely outlined by interpreted horizon-marker. Numerous factors are considered for describing macrolayers. First, in general the lithofacies proportions will vary layer by layer inspite of having global rock property trends and relationships. Second, the trace matching of the pseudo-well synthetics to the input seismic is performed separately in each macrolayer, so depending on the size of macrolayers, a significant number of pseudo-wells will be required to achieve a decent match. These macrolayers contain a stack of stochastic micro-layers, which are generated as a continuous time Markov chain (CTMC). Each micro-layer represents an individual lithofacies. The transition probabilities, generally derived from local well-control are utilized by CTMC for the stochastic ordering of lithofacies (Connolly, 2017). Initially, different lithofacies types are sampled from a (discrete) Markov chain with a transition probability matrix (TPM). The layer thickness is expressed by a random variable chosen from an exponential distribution — an individual distribution for each lithofacies. The application of CTMC to model sedimentation appears to have been first initiated by Rolke (1991). For generating pseudo-wells, this concept provides

control on the lithofacies proportions which is extensively used to match prior information from the geologic model.

Bed thicknesses statistics were insensitive to the geology (Schwarzacher, 1975). Therefore, it enables practical pseudo-wells to be generated without having accurate details of the depositional environment (geology). It is observed that clastic beds repeatedly conform to a long-tailed distribution such as the power law, exponential, or log normal. This is the foundation for the colored inversion (CI) process (Lancaster and Connolly, 2007). The pseudo wells are built by microlayers with a thickness range of less than two orders of magnitude, and within these limits, the differences between these three mentioned distributions are not large. Therefore, an exponential distribution is used which fits the data well and is simple to parameterize. The PDF of an exponential distribution is expressed by $\lambda e^{-\lambda x}$ and the complementary cumulative distribution function (CCDF) by $e^{-\lambda x}$, where x, in this process, is the bed thickness. The mean bed thickness for an infinite distribution is $1/\lambda$. (Connolly and Hughes, 2016). The prior model provides spreads of lithofacies proportions that are expected for each macrolayer. As, the pseudo wells are built from the prior model, they include the same spreads. Pseudo-well lithofacies proportions relies on the interplay between the CTMC parameterization for each lithofacies. Ranges of proportions are controlled by establishing a range of lambda (λ) values for each lithofacies with values being selected randomly from these ranges when generating pseudo-wells. (Connolly and Hughes, 2016)

3.10.3 Rock property relationship

The lithofacies columns are the building blocks for the pseudo-wells. A suite of petrophysical and elastic curves are produced using rock physics trends and calibrated

to real well data. Each lithofacies is modeled individually. Property values can either be kept unchanged or vertical variation can be introduced within each macrolayer by utilizing an autoregressive (AR) model.

For Non-reservoir facies, rock property relationships are established based on trends of depth -Vp, Vp–Vs and Vp-density.

For reservoir facies, rock property relationships are established based on trends of porosity-depth, shear modulus – porosity and dry frame bulk modulus (K_dry) - shear modulus. These elastic properties depend either on the real well data or are estimated from a Vp − Vs relationship similar to Castagna et al. (1985) or Vernik and Fisher (2001). (Connolly and Hughes, 2016)

3.10.4 Trace matching

The extended elastic impedance (EEI) concept (Whitcombe et al., 2002) is primarily used in providing a framework for the trace matching. EEI has been established to be a robust model and is extensively used across the industry (e.g., Neves et al., 2004; Hafez et al., 2014; Westeng et al., 2014; Tyiasning and Cooke, 2015). The trace matching process is between band-limited extended elastic impedance synthetics and seismic traces altered to equivalent band-limited impedance. As previously mentioned, EEI is a two-term AVO model that presumes that the valuable signal component within the data is captured by the combination of intercept and gradient. EEI is parameterized by the rotation angle χ in the intercept-gradient space. Pseudo well Vp, Vs and Rho logs are used in the process of generating the EEI synthetics, using the standard EEI formula and thereby transforming to seismic resolution. Seismic data are prepared from a combination of intercept and gradient, initially the desired χ-angle is obtained, and

subsequently colored inversion is applied for converting to band-limited impedance (Lancaster and Whitcombe, 2000). These data sets are mentioned as χ-angle stacks here as they can be generated as weighted stacks of common midpoint data (Connolly, 1999). Despite the fact, that the matching could be carried out on reflectivity data, inclination is towards band-limited impedance. Colored inversion (CI) is hugely popular across the industry (e.g., Hafez et al., 2014). Color inversion can also be implemented to match spectra from different angle stacks for optimizing the resolution (Connolly et al., 2005). It is possible to invert one or multiple color inverted χ-angle stacks simultaneously. The χ-angles are chosen, depending on the rock property study, in order to have optimal correlation with the desired reservoir properties (Whitcombe and Fletcher, 2001; Hicks and Francis, 2006). Simultaneously inverting two χ-angle stacks is frequently required when estimating lithofacies probability having three facies type or two reservoir properties such as net-to-gross and porosity. The relative amplitudes of the synthetic and the seismic trace are of significance, so a shape-only based metric such as crosscorrelation is not sufficient for estimating reservoir properties. The match quality metric used here is energy of the difference, the root-mean-square (rms) error. There is an assumption that the seismic volumes are consistently scaled, so a single scaling factor is applied to the pseudowell synthetics. (Connolly and Hughes, 2016)

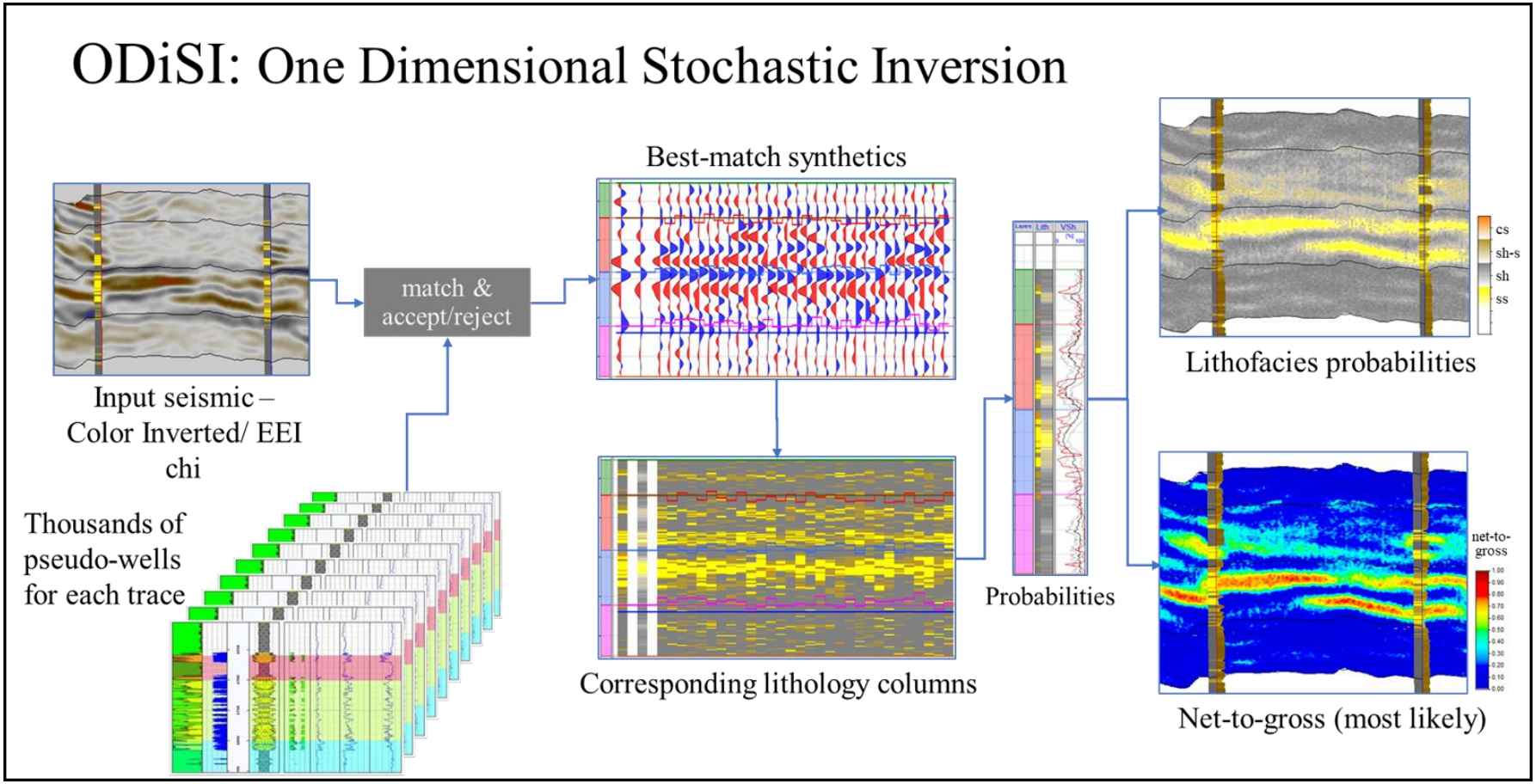

***Figure 3.8**: The ODiSI workflow. Courtesy of Cegal.*

4. Data

The data adopted for this study is provided by Equinor ASA. It encompasses multiple 3D seismic cubes and well data from 3 wells. In this chapter, the data are presented and explained in short.

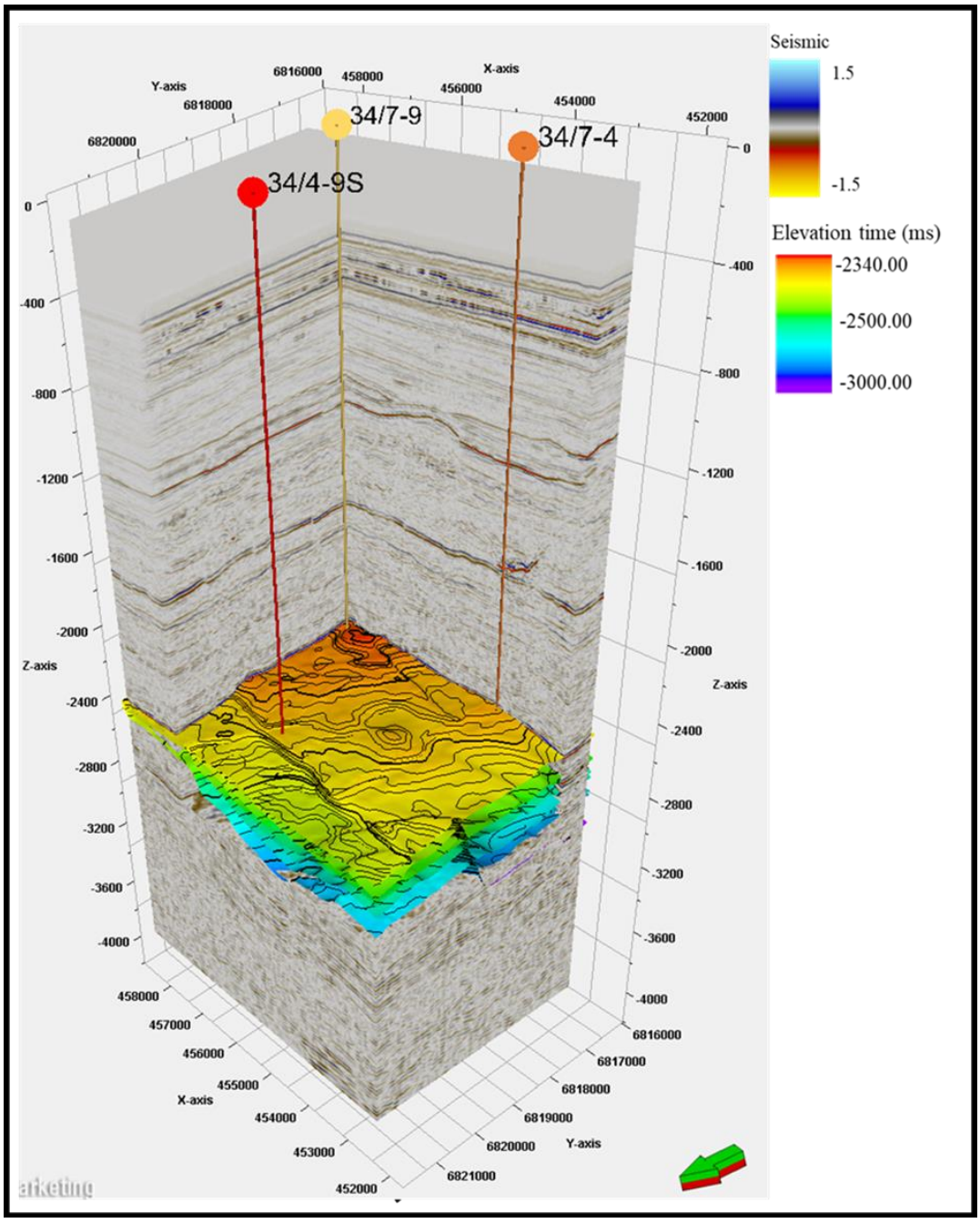

***Figure 4.1**: 1997 near stack seismic cube displayed together with the wells and the available horizons.*

4.1 Seismic

The seismic survey used in the study was acquired in 1997 (Figure 4.1). It covers an area of 535 sq. km. This survey was selected deliberately, since it is not affected by any production effects. The dataset contains multiple 3D seismic cubes (angle stacks). The angle stacks are organized into three following groups: a near-angle stack ($0\text{-}15^0$), a mid-angle stack ($15^0\text{-}30^0$), a far-angle stack ($30^0\text{-}45^0$). The seismic data is of SEG normal polarity, implicating that the positive peak corresponds to increase in acoustic impedance.

***Table 2**: Summary of provided seismic data*

Acquiring year	Polarity	Stack (in time)	Angles, °
1997	SEG - Normal	Near	0-15
		Mid	15-30
		Far	30-45

***Table 3**: Summary of provided wells with some well logs*

Well Type	Well	GR	ρ	Dtp	Dts	φ	Sw
Exploration	34/4-9S	Yes	Yes	Yes	Yes	Yes	Yes
	34/4-9	Yes	Yes	Yes	No	Yes	Yes
	34/7-4	Yes	Yes	Yes	No	Yes	Yes

4.2 Well

Data from three exploration wells are utilized in this study (Table 3). The wells encompass the study area and several logs are available providing crucial knowledge mainly at reservoir interval. In addition, checkshot surveys are available for all the wells. Wells containing P, S - wave sonic and density logs are significant for the study. Well 34/4-9S contain these parameters.

4.3 Additional data

In addition to seismic and well, key interpreted horizons and fluid properties are provided at the reservoir interval in the study area.

***Table 4**: Summary of provided fluid data*

Fluid type	ρ (gm/cm3)	Vp (m/s)	K (kPa*s/m)
Water	1.003	1654.94	2.747
Oil	0.762	1201.009	1.101
Gas	0.382	715.363	0.195

***Table 5**: Summary of provided interpretations*

Domain	Interpretations
Time	SN 11.4
	SN 10..4
	BCU
	SN 9.3
	SN 8.2
	SN 6.2
	Oil Water Contact

5. Methodology

According to the theory mentioned above, several methods were carried out in the study. A generic workflow in figure 5.1 provides an overview of the methods that were applied in the study. Initially, conditioning was performed on the seismic data to make it eligible for further study.

Thereafter, typical well log analysis and seismic analysis were carried out. The successive tasks comprised of performing Colored inversion and Extended elastic impedance to obtain the optimal input which was used for the final step i.e. one-dimensional stochastic inversion.

The different methods are described in this chapter.

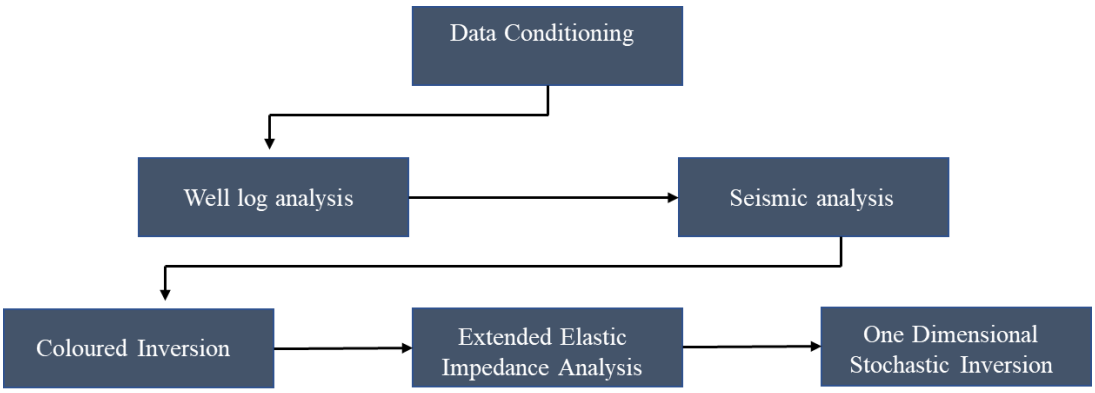

***Figure 5.1**: Workflow of the main methods that were applied in this study.*

5.1 Data Conditioning

Data conditioning is an essential step prior to performing inversion. Phase, amplitude spectra, and time alignment difference between the angle stacks make the data unreliable for future study. Therefore, a conditioning data workflow (Figure 5.2) was carried out to obtain a set of reliable angle stacks fit for inversion study. The near-angle

stack had issues regarding multiples and the far-angle stack had curvature issues, consequently the mid-angle stack was selected as the master stack. The workflow contains three stages:

- Phase Matching
- Amplitude spectra matching
- Time alignment

Avocado is a software platform typically designed for Data Quality Control (QC) and Conditioning. The three angle stacks as mentioned in the chapter 4.1 were loaded in the Avocado software platform to perform the Data Conditioning workflow.

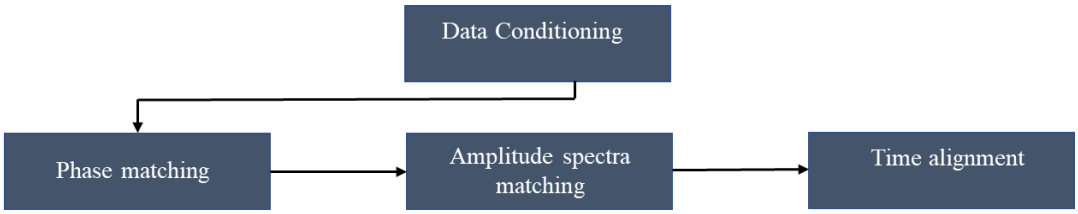

***Figure 5.2**: Workflow of the data conditioning and QC that were applied in this study.*

5.1.1 Phase Matching

Inversion is carried out based on the expectation that the seismic data is of zero phase. The phase analysis window was set at -2000 ms, as this represents the area of interest. Various types of cross correlation algorithms such as general cross correlation, envelope cross-correlation, instantaneous cross-correlation, quad envelope cross-correlation and rotation cross-correlation were carried out between each angle stack and the master stack to check the requirement of phase shift.

5.1.2 Amplitude spectra matching

The purpose of this step is to make one common frequency spectrum for all the angle stacks. The spectra of near and far stack was reshaped to that of the master stack.

5.1.3 Time alignment

The purpose of time alignment is to rectify any time shift between each angle stack. The position of top reservoir (BCU) was aligned in the near and far stack as compared to its position in the mid (master) stack.

5.2 Reservoir Overview

After the data QC and conditioning, routine analysis of well log data and seismic analysis were performed to obtain a basic overview of the reservoir. The analysis involves an elementary interpretation for both well log and seismic data.

5.2.1 Well log data analysis

All of three wells were utilized for the well log interpretation. Initially, a general well log data QC was performed, to have appropriate data values prior to further investigation. A facies log was generated with the help of discrete facies flag and Volume of shale (Vsh) logs. The facies classification was further validated with the help of various crossplots using logs such as gamma ray, density-neutron combination

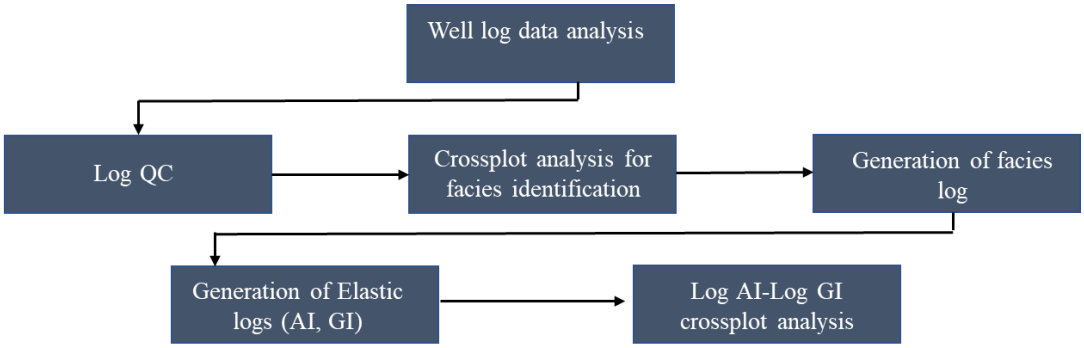

***Figure 5.3**: Workflow of the well log analysis that were applied in this study.*

and porosity. Subsequently, an acoustic impedance (AI) log was calculated for all the wells using P-wave sonic and density. In addition, shear impedance (GI) log was generated for the only well with S-wave sonic. Eventually, crossplots between AI and GI were formed, colored by different parameters such as facies, water saturation (Sw), total porosity and Vsh to observe the segregation of data points in the impedance domain.

5.2.2 Seismic analysis

Seismic well ties were performed to validate the provided interpretations. All the interpretations provided, were used to generate their corresponding surfaces. The seabed was interpreted across the area. The surfaces created were edited in order to avoid any intersection. This was done as a requirement to the later stage. In addition, two sets of intercept and gradient stacks were produced, one set from the near and mid-angle stack, and the other from mid and far-angle stack.

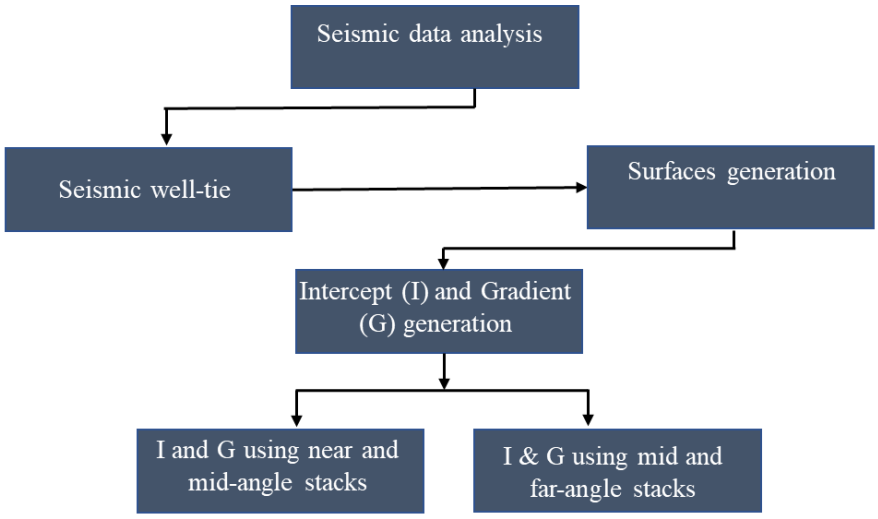

***Figure 5.4**: Workflow of the seismic analysis that were applied in this study*

5.3 Colored Inversion

The following workflow (Figure 5.4) was applied to perform Colored Inversion for this study. The execution of each stage in the workflow is discussed briefly.

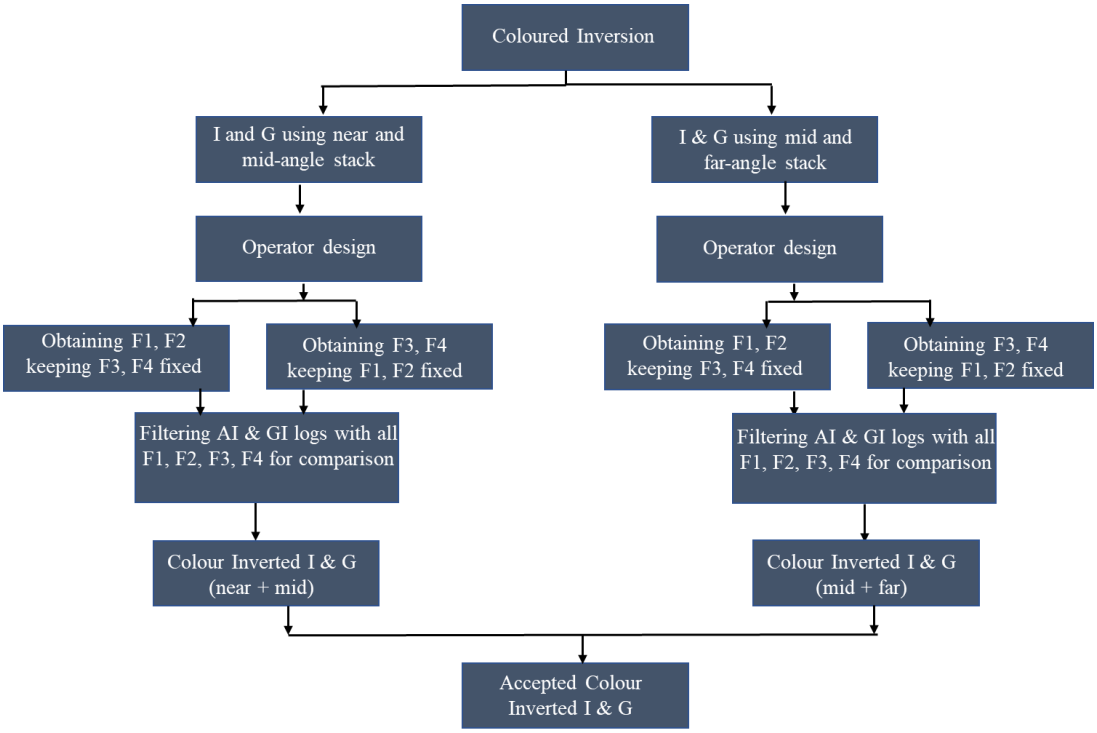

***Figure 5.5**: Workflow of the colored inversion that was applied in this study.*

5.3.1 Input seismic

Initially, colored inversion was applied on intercept and gradient stacks of the two combinations, which were generated previously. The results from both the sets of intercept and gradient proceeded to the later stage.

5.3.2 Operator design

An operator was generated based on impedance from well log data and the input seismic. The frequency range of the operator is defined by four corner point frequencies. F1 (low cut), F2 (low pass), F3 (high pass), F4 (high cut). To obtain the optimal values of F1, F2, F3 and F4, initially, F3 and F4 was kept fixed, and

subsequently, using different values of F1 and F2; the intercept and gradient volume were dynamically color inverted (convolving the operator with the input seismic). After determining optimal F1 and F2 values, correspondingly optimal values for F3 and F4 were obtained by keeping F1 and F2 fixed this time.

5.3.3 Selection of optimal parameters

As discussed earlier, the color inverted volume of intercept and gradient stack represent relative acoustic impedance and relative gradient impedance respectively. Thus, the optimal set of intercept and gradient volume and values of F1, F2, F3, F4 were selected depending on their correlation with relative impedance log values filtered with same frequency corner points. In addition, a visual QC was performed on the basis of resolution, continuity of the impedance layers.

5.4 Extended Elastic Impedance (EEI)

Extended Elastic Impedance was applied to the final cube obtained from the Colored Inversion process. The following workflow was applied in this stage (Figure 5.6).

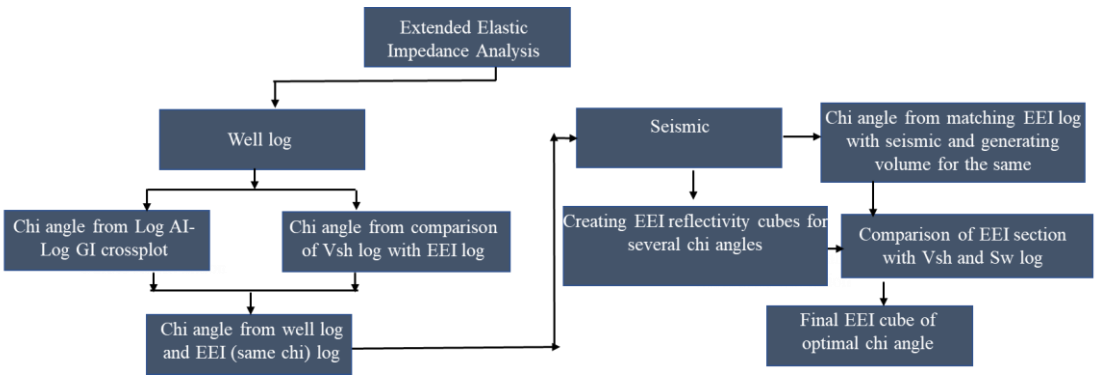

***Figure 5.6**: Workflow of the EEI that was applied in this study.*

5.4.1 Well logs

After performing AI & GI cross plot analysis, a single chi angle was observed, which distinguished the different facies types i.e. sand, shaly sand and shale. In addition, analysis was done to find the optimum chi angle EEI log showing maximum correlation with Vsh log. The chi angle for which the EEI logs had maximum correlation against the raw logs were selected for analysis in the next part.

5.4.2 Seismic

The optimum chi angle EEI log was compared with the EEI reflectivity cubes to obtain the optimum chi angle for seismic. In addition, the optimal chi angle cubes were chosen depending on how well the EEI seismic section was contrasting facies as observed in the well logs. The optimal cube selected in this stage was the input for the stochastic inversion.

5.5 ODiSI

After the preparation of seismic for stochastic inversion, ODiSI is implemented with the following workflow. Well 34/4-9S is the only well which contained Vs log, thus this well was used for the complete parametrization for ODiSI. In this chapter, well 34/4-9S is regarded as the input well. All the input parameters including input well, elastic, petrophysical, and fluid properties were introduced in the platform. In addition, sand litho-facies was categorized as reservoir, whereas shaly sand and shale lithofacies were categorized as non-reservoir.

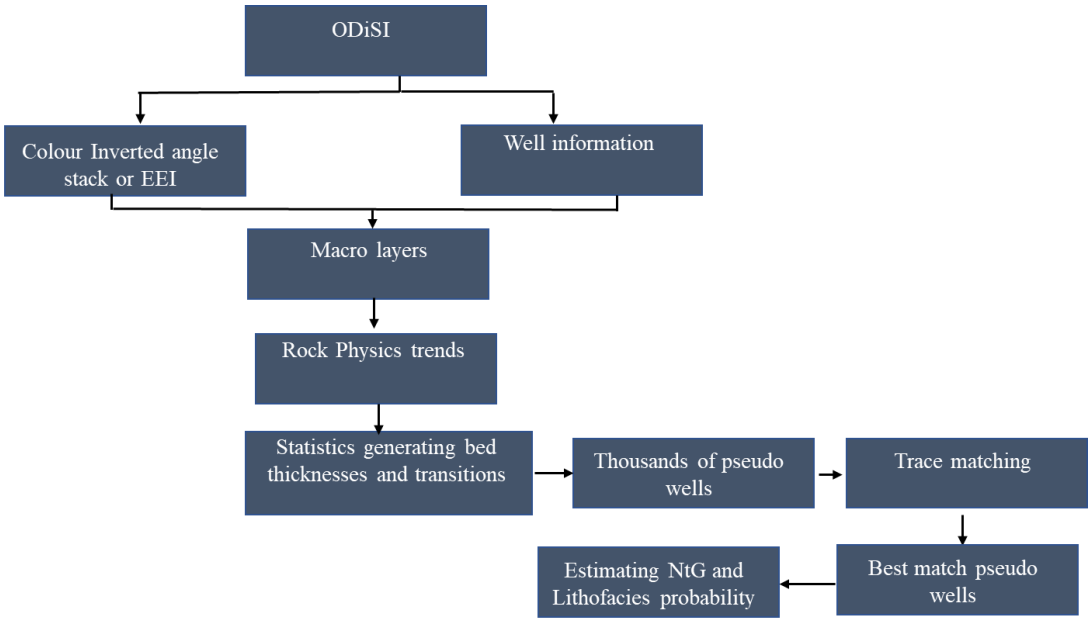

***Figure 5.7**: Workflow of the ODiSI that was applied in this study*

5.5.1 Macro Layers

The area of interest was grouped into 8 macro-layers with 9 boundaries. Care was taken to ensure that the width of each macrolayer was not more than ~ 50ms in order to extract reliable information from each macro-layer. In addition, a fluid contact was also introduced in this stage and EEI constants were defined. Higher variability was introduced in all the macrolayers as the facies type were repetitive and scattered in the area of interest.

5.5.2 Rock Physics

For both reservoir and non-reservoir type, rock physics trends were parametrized for each litho-facies type to predict the elastic properties for the pseudo wells. They were eventually used to build petrophysical well logs in the pseudo wells. For reservoir facies, trends of porosity-depth, porosity-shear modulus and shear-bulk modulus were defined and for non-reservoir, simple trends as depth-Vp, Vp-Vs and density-Vp were

defined. This was because Gassmann fluid substitution was used in the reservoir facies to add in fluids. The well logs data generated by the pseudo well rock physics trends were investigated using several quality control techniques. Initially, the petrophysical log suites of both input and pseudo well were examined to observe the extent of correlation among them. Further, elastic properties were examined by cross-plotting the same parameters for both input and pseudo well to visualize their match. The trends were modified in order to make the pseudo well logs data behave similar to that of the input well in the well location.

5.5.3 Transitions and Thickness

The well data was used as a guide in estimating thickness estimation and probability of facies for each macro layer. Thereafter it was expanded in order to allow ODiSI to explore the full range of thickness possibilities. In order to allow for that the maximum possible thicknesses exceeded that of what is observed in the well. Lambda values controlled the distribution of possible thicknesses and weight between thick and thin, and thus were assigned appropriately. Transition governed the probability or likelihood of which facies is encountered as one moves from one facies to other. The lithofacies column for pseudo wells were generated from the vertical statistics (bed thicknesses and transitions probabilities). The vertical statistics were adjusted in a manner so that the distributions of beds, facies, porosity and net to gross for 100 pseudo wells maintain the desired range of values covered in each macro layer.

5.5.4 Trace matching

The number of pseudo wells used for inversion was 10000 out of which 100 were averaged. Inversion was performed on the trace on all the well locations. Single inversions were performed using the optimal EEI cubes obtained in the previous stages. Subsequently, a similar set of parameters such as petrophysical logs, synthetic seismic traces, lithology columns were generated at the same location of the input well and was compared with the corresponding input parameters.

5.5.5 Inversion Realization

In the trace matching process, inversion realization was performed only in the individual EEI cubes individually. In the beginning, various 2D lines passing through the wells were realized to obtain lithofacies probability, net to gross, porosity and water saturation. Finally, the entire cube was realized to obtain inverted cubes of lithofacies probability and net mean (net to gross).

6. Results

6.1 Data Conditioning

As discussed above, the seismic data conditioning and QC was performed, the provided surfaces in the study interval and seismic angle stacks were utilized for this analysis. As mentioned earlier, the mid-angle stack was used as the master stack. The results are presented below.

6.1.1 Phase matching

Figure 6.1 and 6.2 show the phase analysis of near and far angle stack with the master stack respectively. It is displayed in both the mentioned figures that the phase of each angle stack with the master stack is symmetrical and consistent along the study area. Accordingly, no phase rotation was applied to angle stacks as observed in the rotation cross-correlation in figure 6.1 and 6.2.

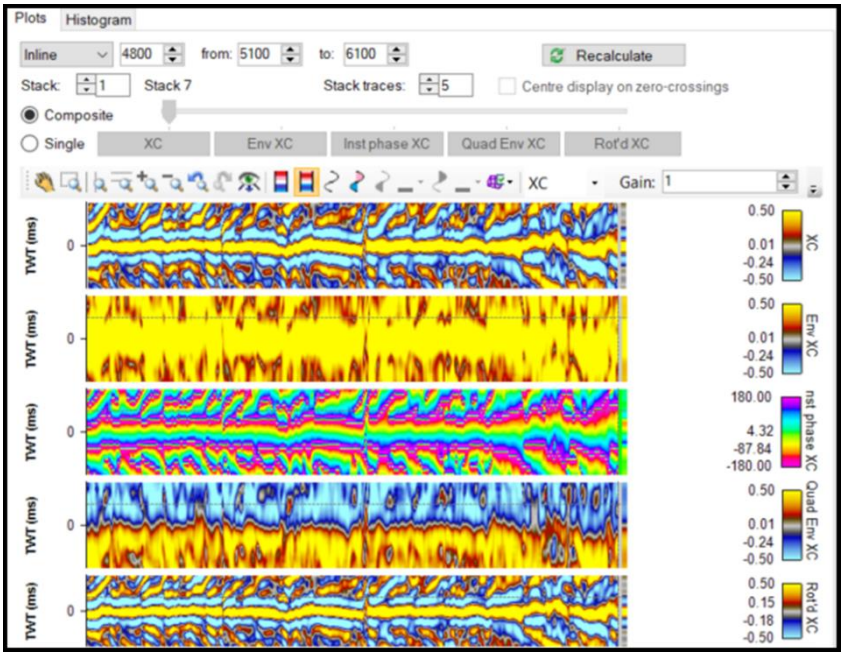

***Figure 6.1**: The composite of phase analysis between near and mid (master) stack.*

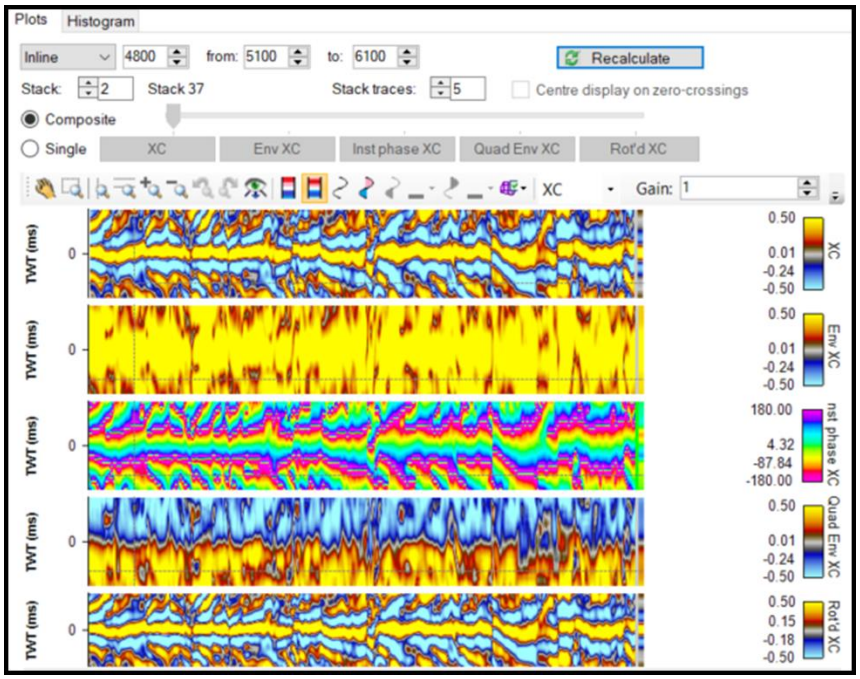

***Figure 6.2**: The composite of phase analysis between far and mid (master)*

6.1.2 Amplitude spectra matching

Figure 6.3 shows the initial amplitude spectrum of the three different angle stacks of the study area. The spectrum of near and far angle stack was optimally transformed to that of the master stack. (Figure 6.4).

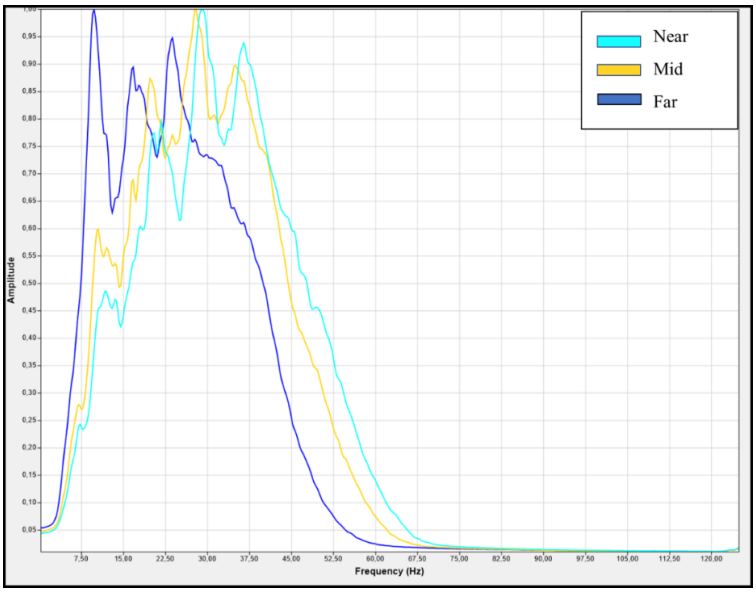

***Figure 6.3**: Frequency spectrum of the three angle stacks (before matching).*

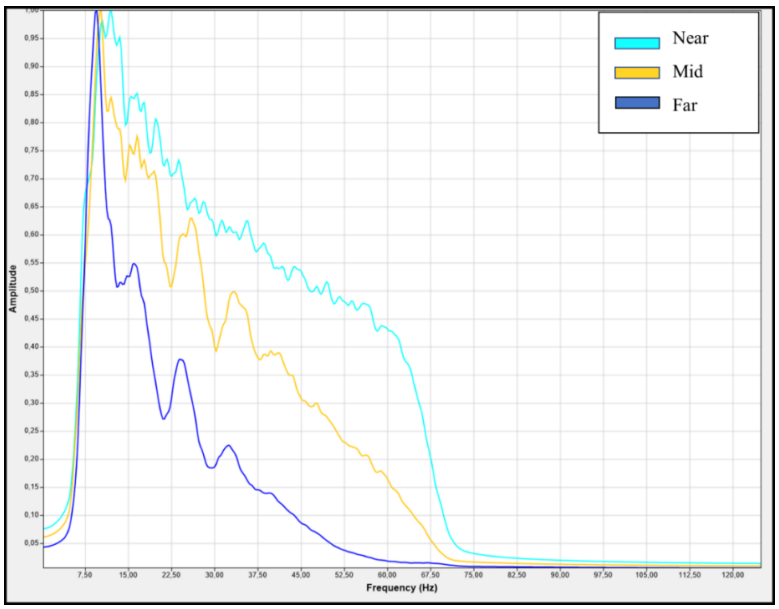

***Figure 6.4**: Frequency spectrum of the three angle stacks (after matching).*

6.1.3 Time Alignment

All the interpretations available in the study area were used for this step. Figure 6.6 and 6.7 shows the gathers of before and after applying time alignment between near and the master stack respectively. Similarly, figure 6.8 and 6.9 displays the gathers of before and after applying time alignment between far and the master stack respectively. The time shift for the near stack and far stack is not significantly different as compared to the master stack (Figure 6.5). Maximum threshold time shift was set at 20 ms and cross correlation cutoff was 0.01. The time alignment was performed for making the input stacks fit for further study.

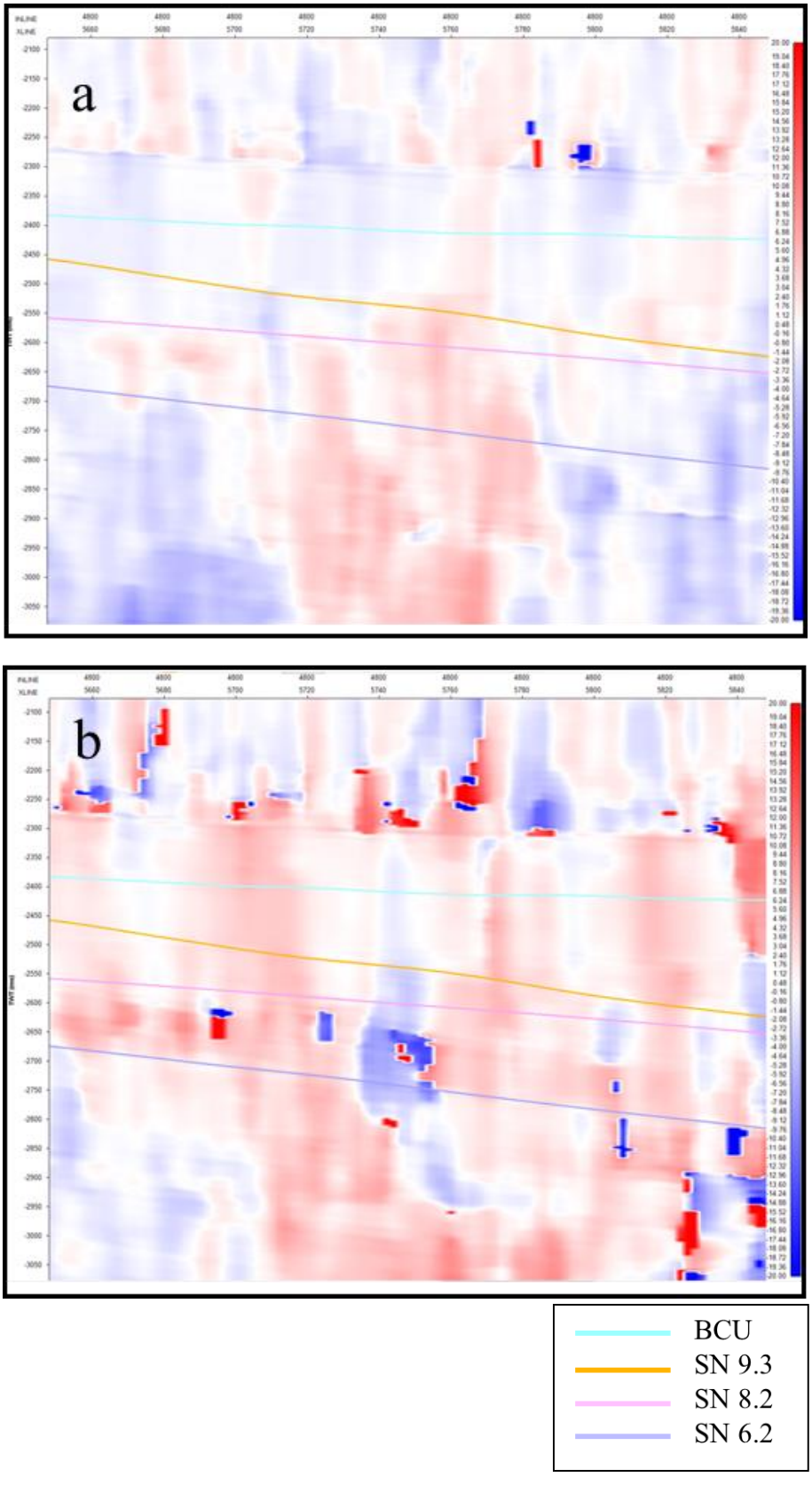

***Figure 6.5**: Time shift map of a.) near with mid stack. b.) far with mid stack*

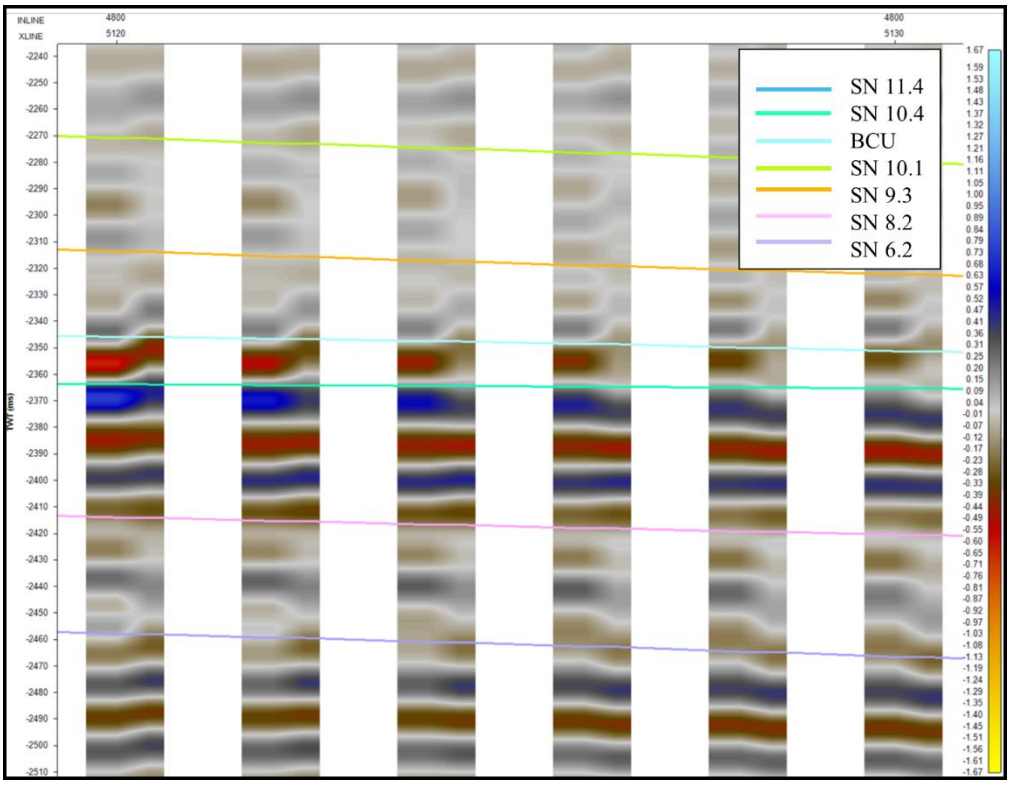

***Figure 6.6**: Comparison between gathers of near and mid (master) stack before time alignment.*

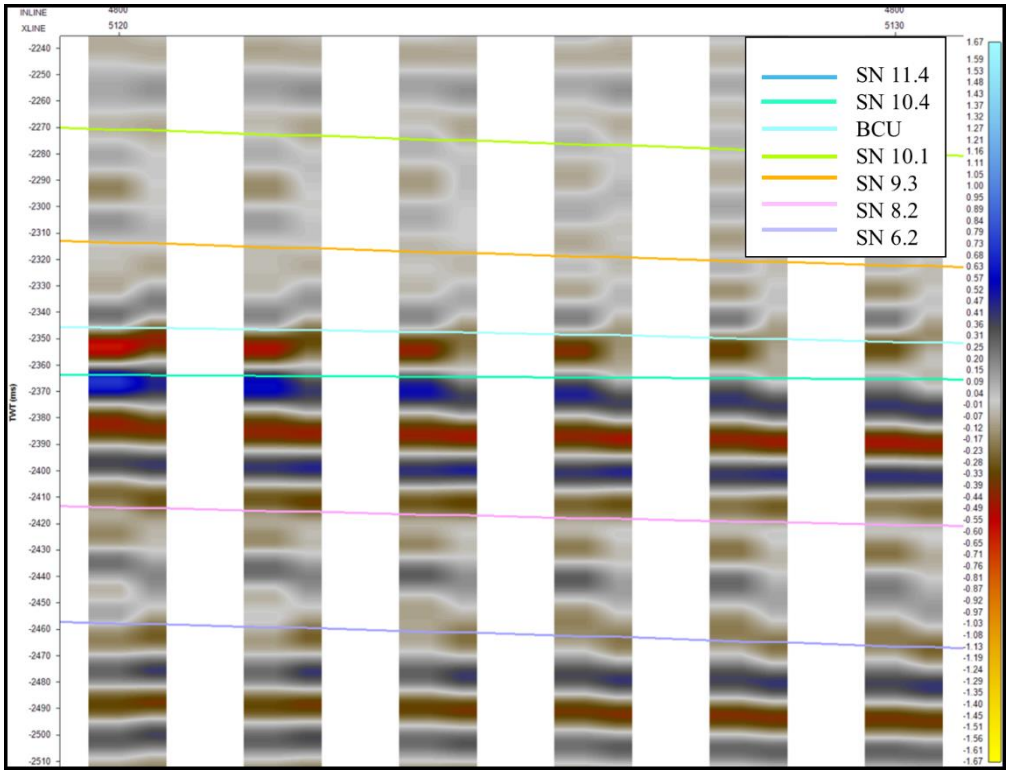

***Figure 6.7**: Comparison between gathers of near and mid (master) stack after time alignment.*

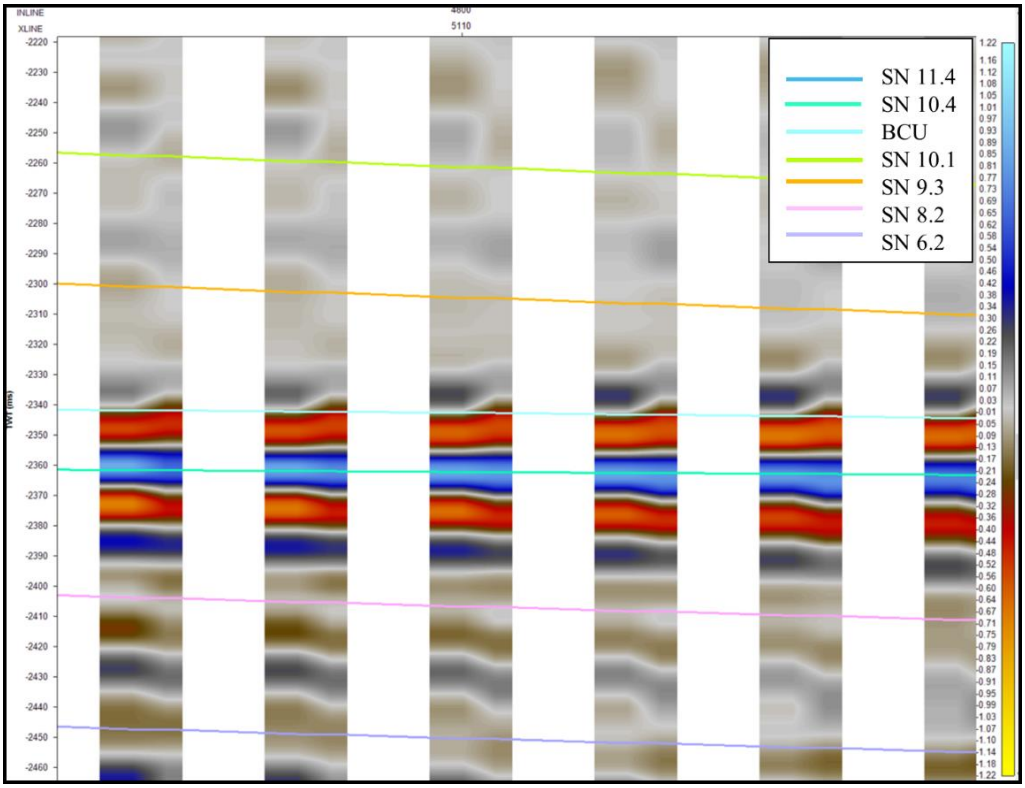

***Figure 6.8**: Comparison between gathers of far and mid (master) stack before time alignment.*

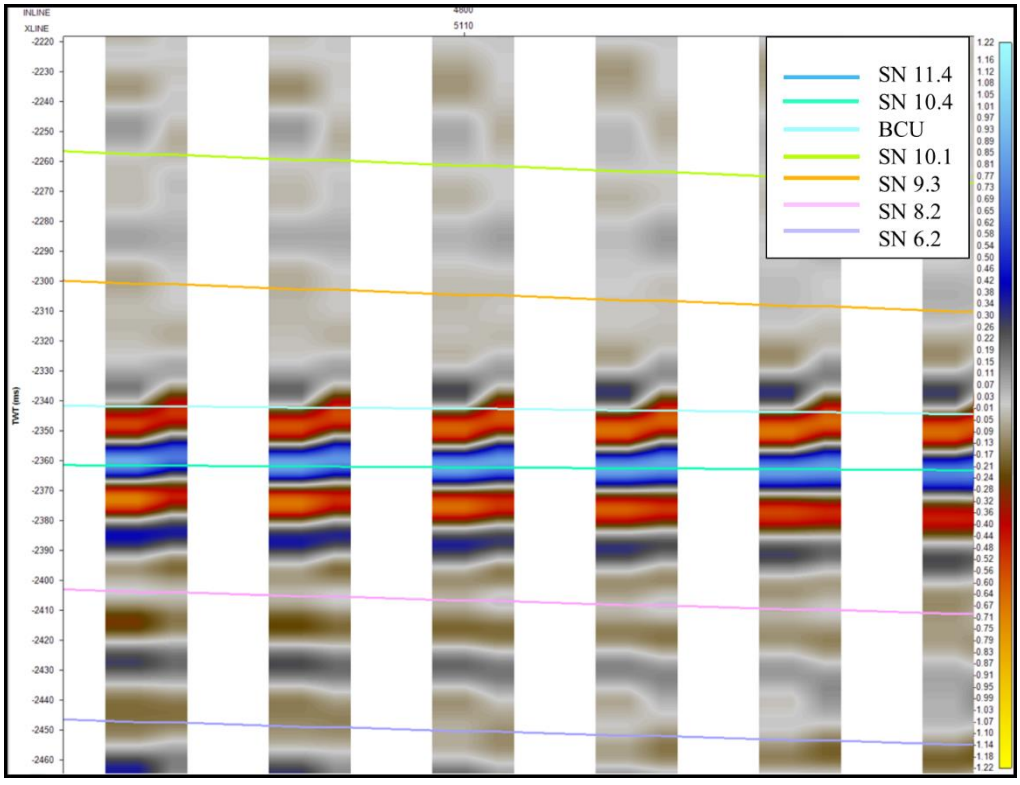

***Figure 6.9**: Comparison between gathers of far and mid (master) stack after time alignment.*

6.2 Reservoir Overview

An overview of the reservoir interval in both seismic and well log data has been presented here. The reservoir thickness varies in the study area, in addition lithological changes are prominent (Figure 6.10). The well log analysis and seismic analysis are further discussed in chapter 6.2.1 and 6.2.2 respectively.

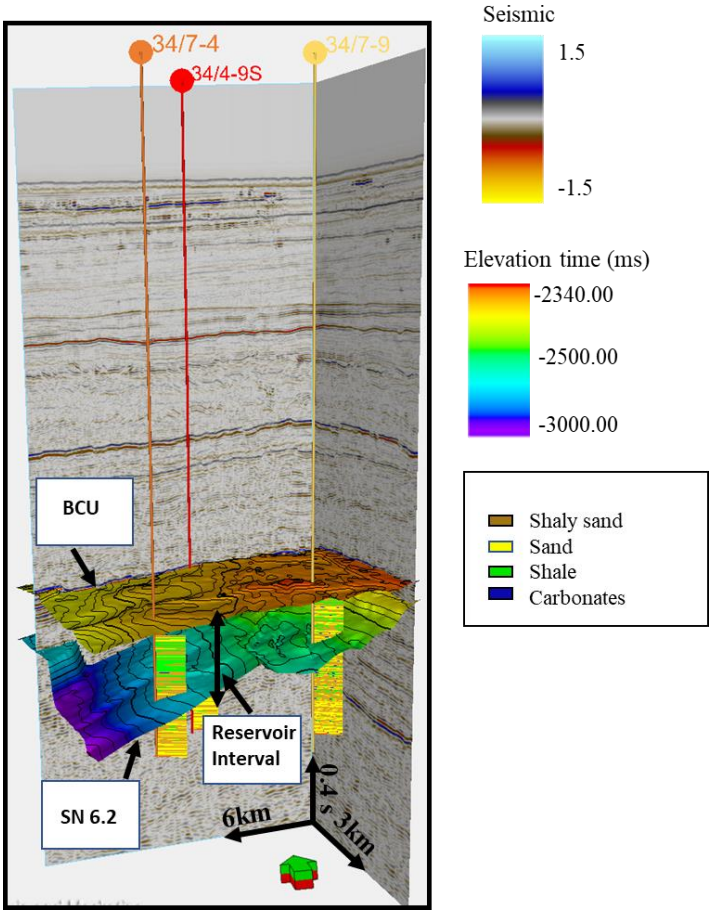

***Figure 6.10**: Reservoir interval in the study area.*

6.2.1 Well log analysis

Figure 6.11 displays the grouping of data points in the crossplot of neutron and density log colored by vshale. These various groups are highlighting different lithofacies type. The facies classification made using the provided facies flag logs are validated in the neutron-density crossplot (Figure 6.12).

Crossplot analysis of Acoustic Impedance (AI) and Shear/Gradient Impedance (GI) logs for well 34/4-9S show the separation of different lithofacies in impedance domain. There is a good separation between sand and rest of the lithofacies elastically (Figure 6.13).

Well interpretations of the study area are shown in Figure 6.14. An overview of the interpreted well log response of the reservoir, including the different reservoir units and fluid contact is given as follows:

- Gamma ray (GR) readings are lower for the sand compared to the shale and shaly sand. In addition, higher GR values are observed for rocks of high reservoir quality compared to rocks less favorable for oil production.

- The density-neutron combination (ρ, φN) delivers close to zero separation for brine saturated sand, and a negative separation for oil filled reservoir rocks. The shale and intervals of shaly sand with high percentage of shale are represented by a positive separation.

- The acoustic impedance (AI) is lower for the units in the vicinity of fluid contact than rest of the zone.

- The use of porosity (φ) and water saturation (Sw) logs are self-explanatory in that they indicate the quality of the reservoir rocks. The highest reservoir quality is observed for the SN 11 and SN10 in the area in the vicinity of well 34/4-9S. This area yields porosities and net to gross of about 25 % and 30% respectively (Seldal et al. 2008; Table 1).

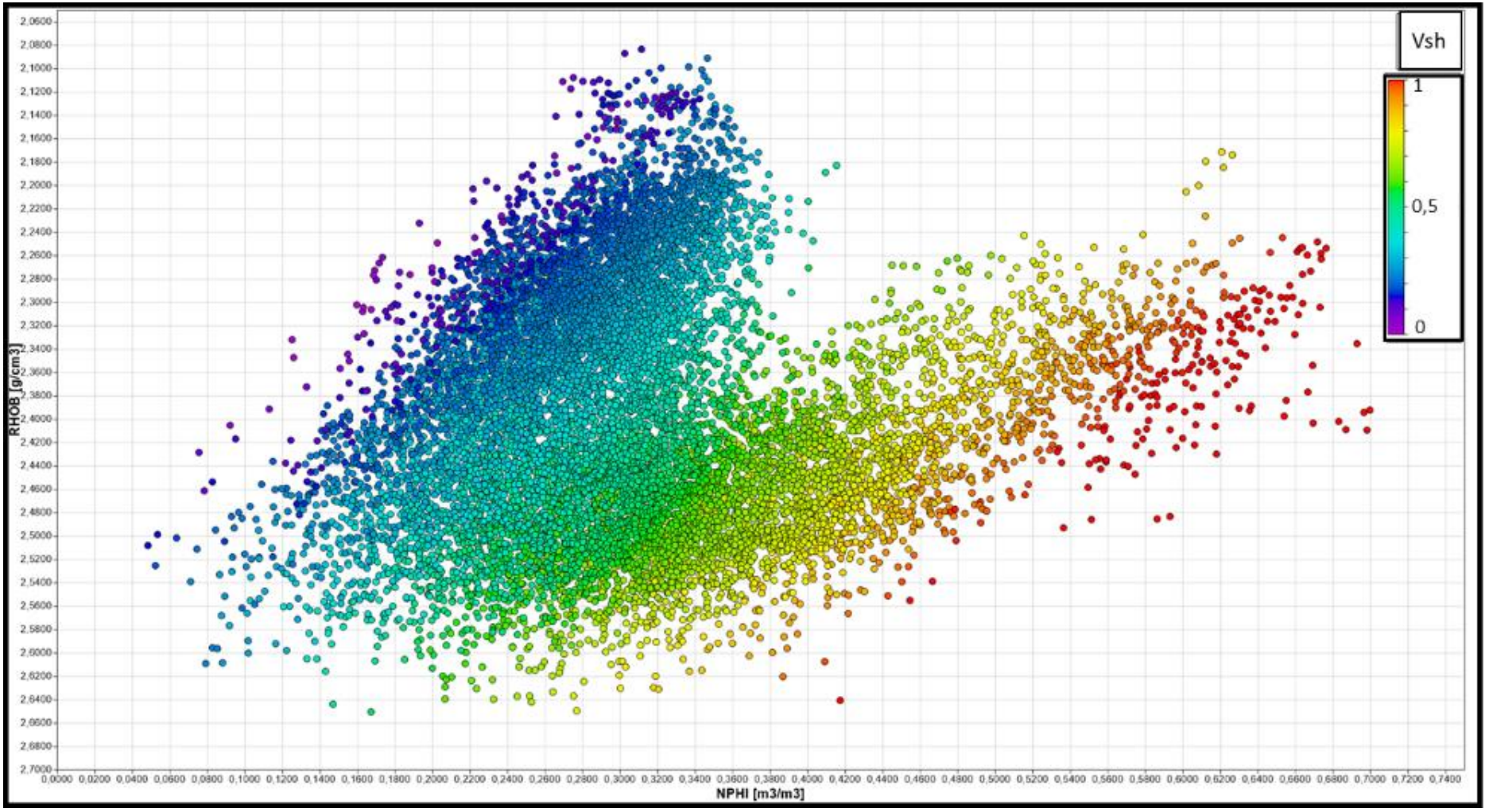

***Figure 6.11**: Crossplot of Neutron vs Density colored by Vshale.*

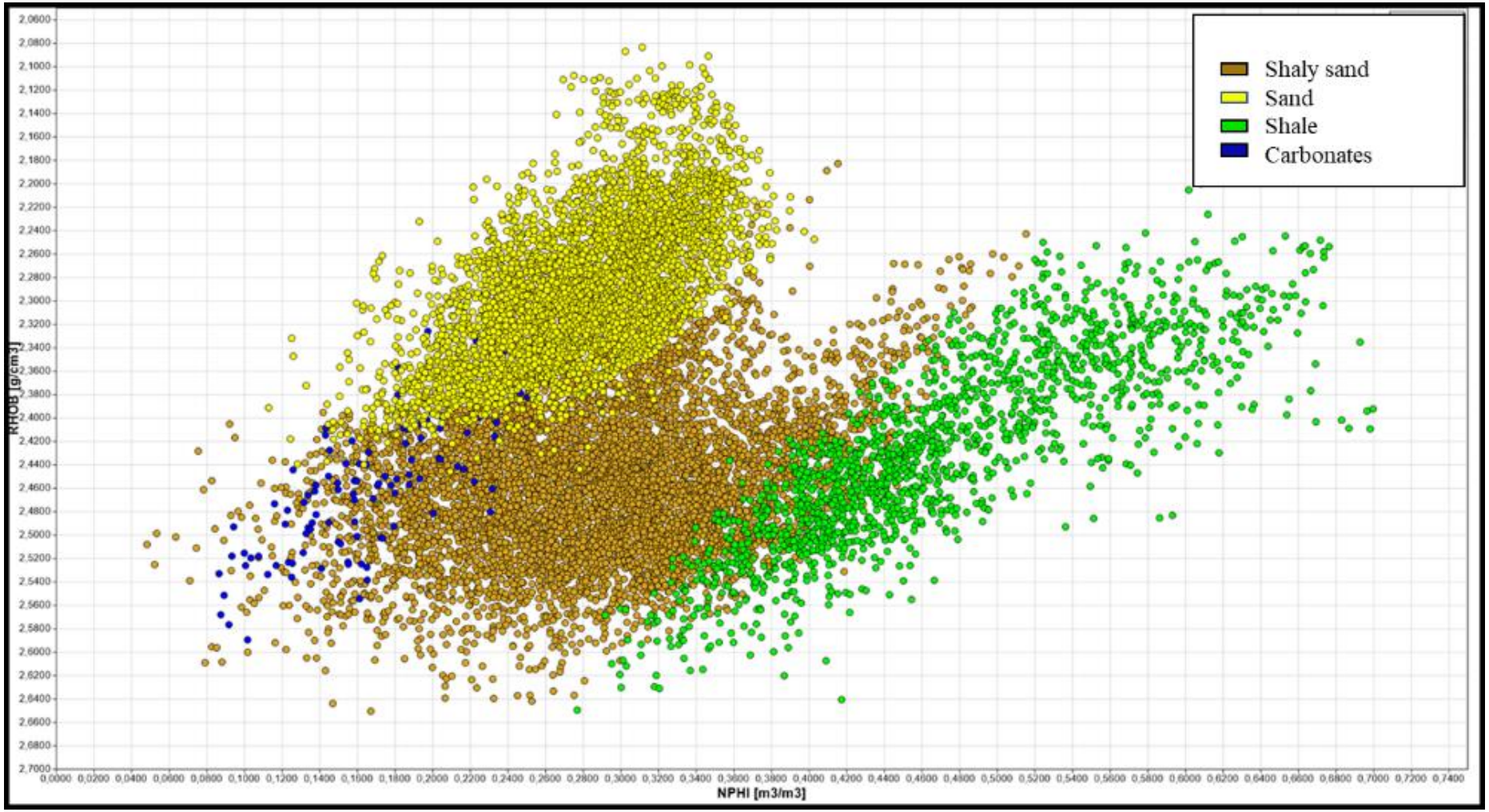

***Figure 6.12**: Crossplot of Neutron vs Density colored by Facies.*

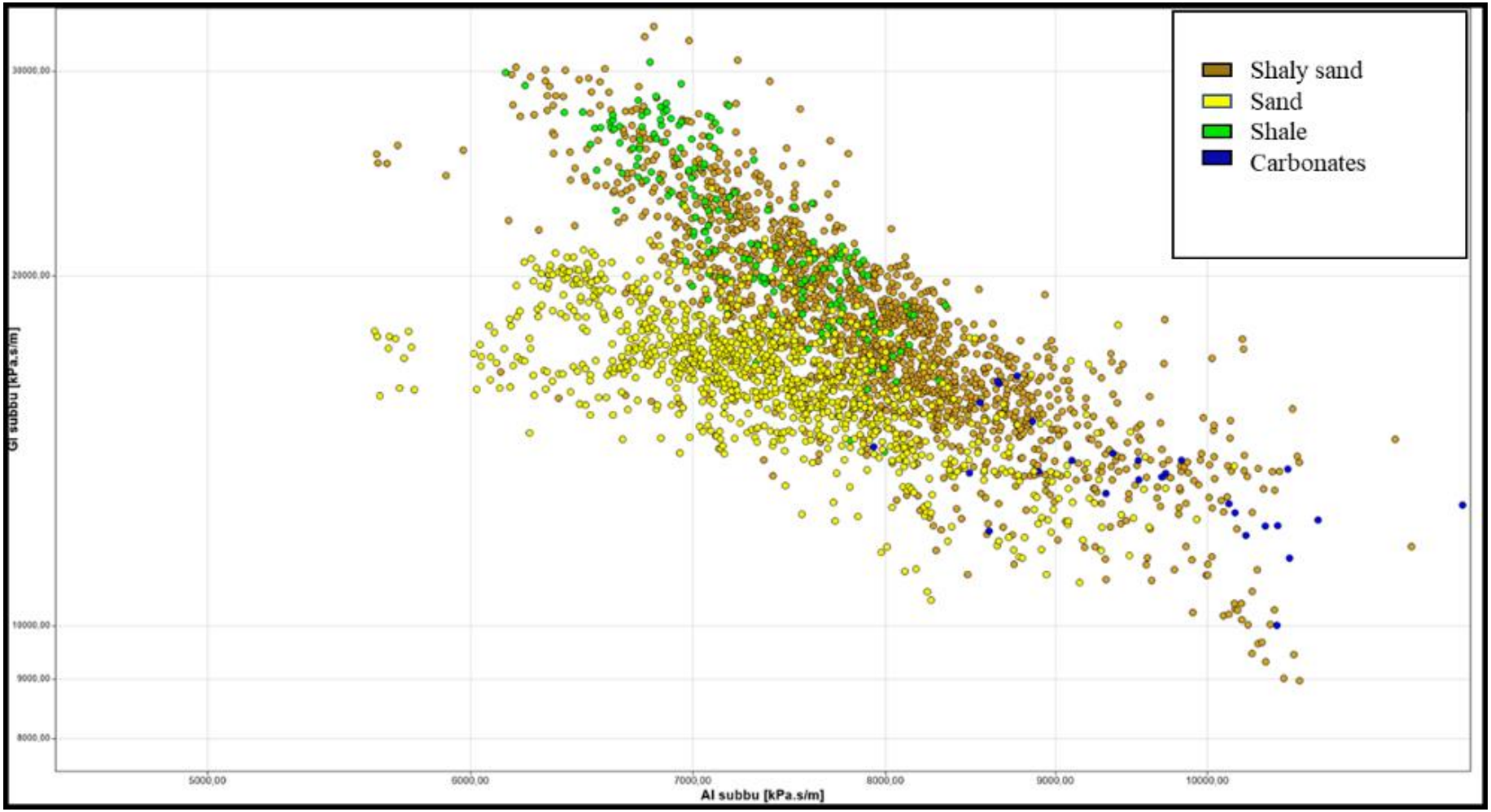

***Figure 6.13**: Crossplot of AI vs GI of only well 34/4-9S colored by Facies.*

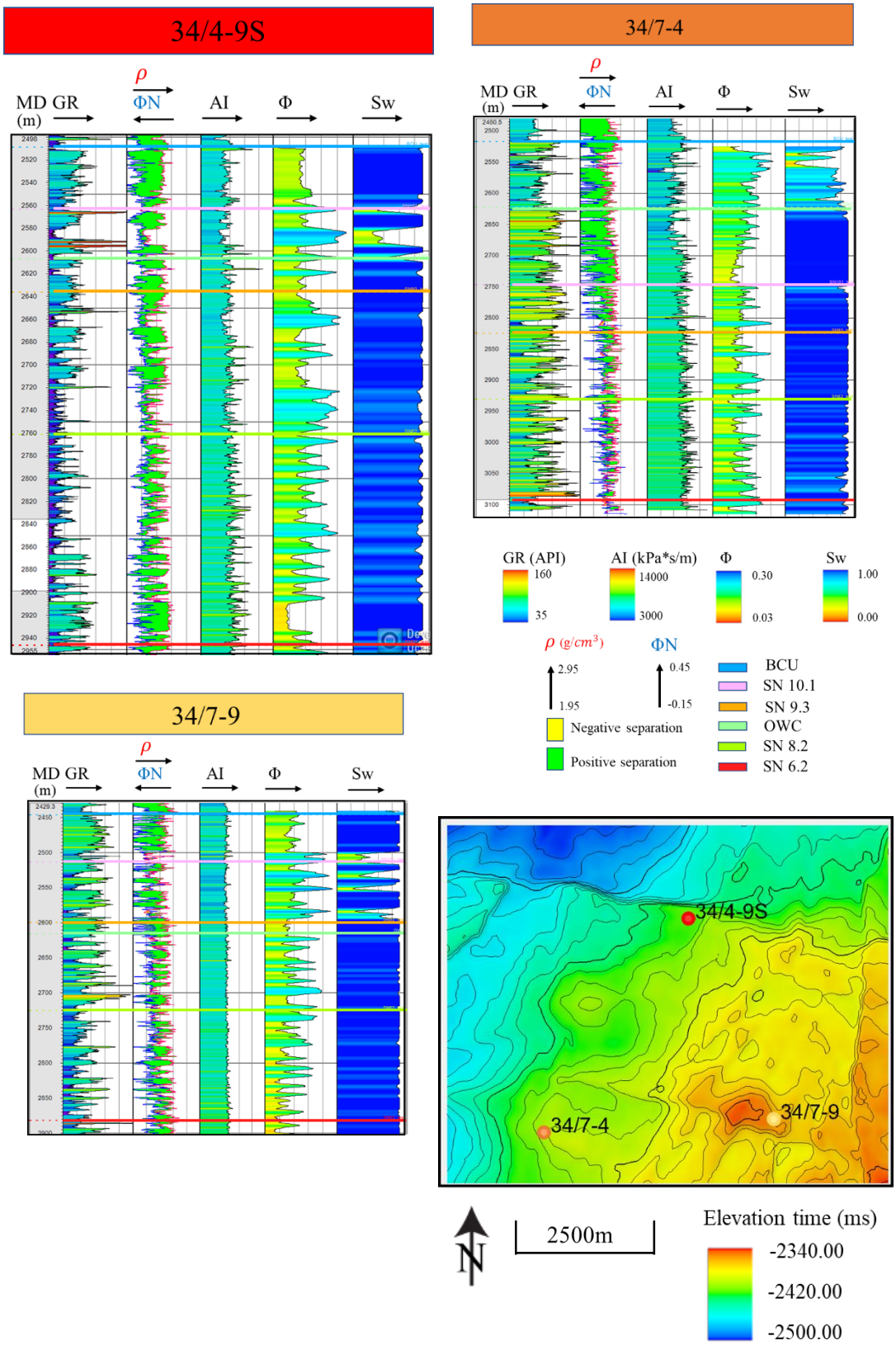

***Figure 6.14**: Well log interpretations based on three key wells covering the reservoir.*

6.2.2 Seismic analysis

Figure 6.16 a, figure 6.17 and figure 6.18 display the well ties that were performed for all the available wells. A Ricker wavelet with normal polarity was used (Figure 6.16 b). The match is good, having coefficient of correlation more than 0.50 in all the three wells present in the study area. The interpretations provided, point to changes in thickness in different parts of the study area (Figure 6.19). Corresponding surfaces were created from the interpretations (Figure 6.15)

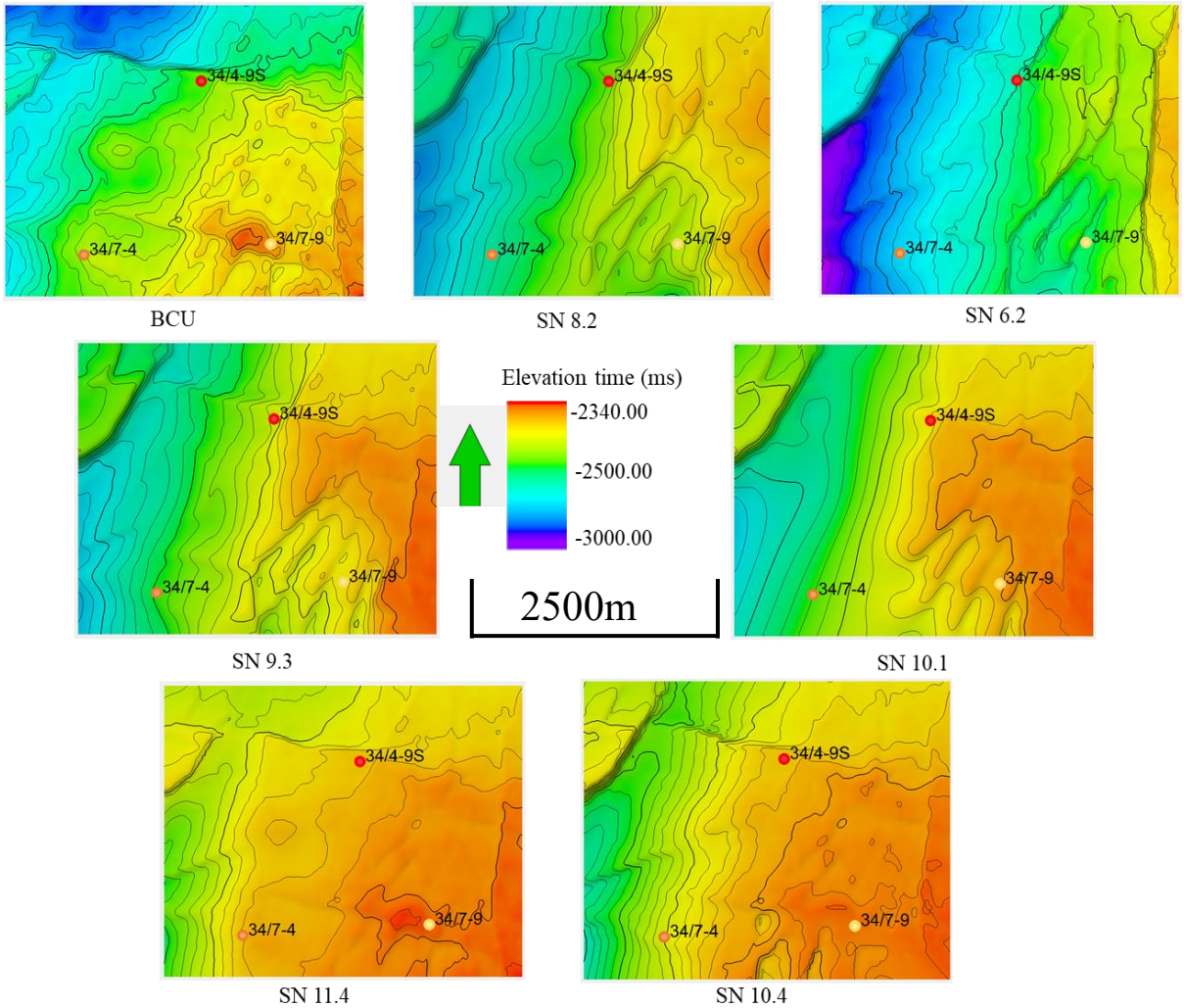

***Figure 6.15**: TWT structural map (surfaces) of the provided horizon marker data*

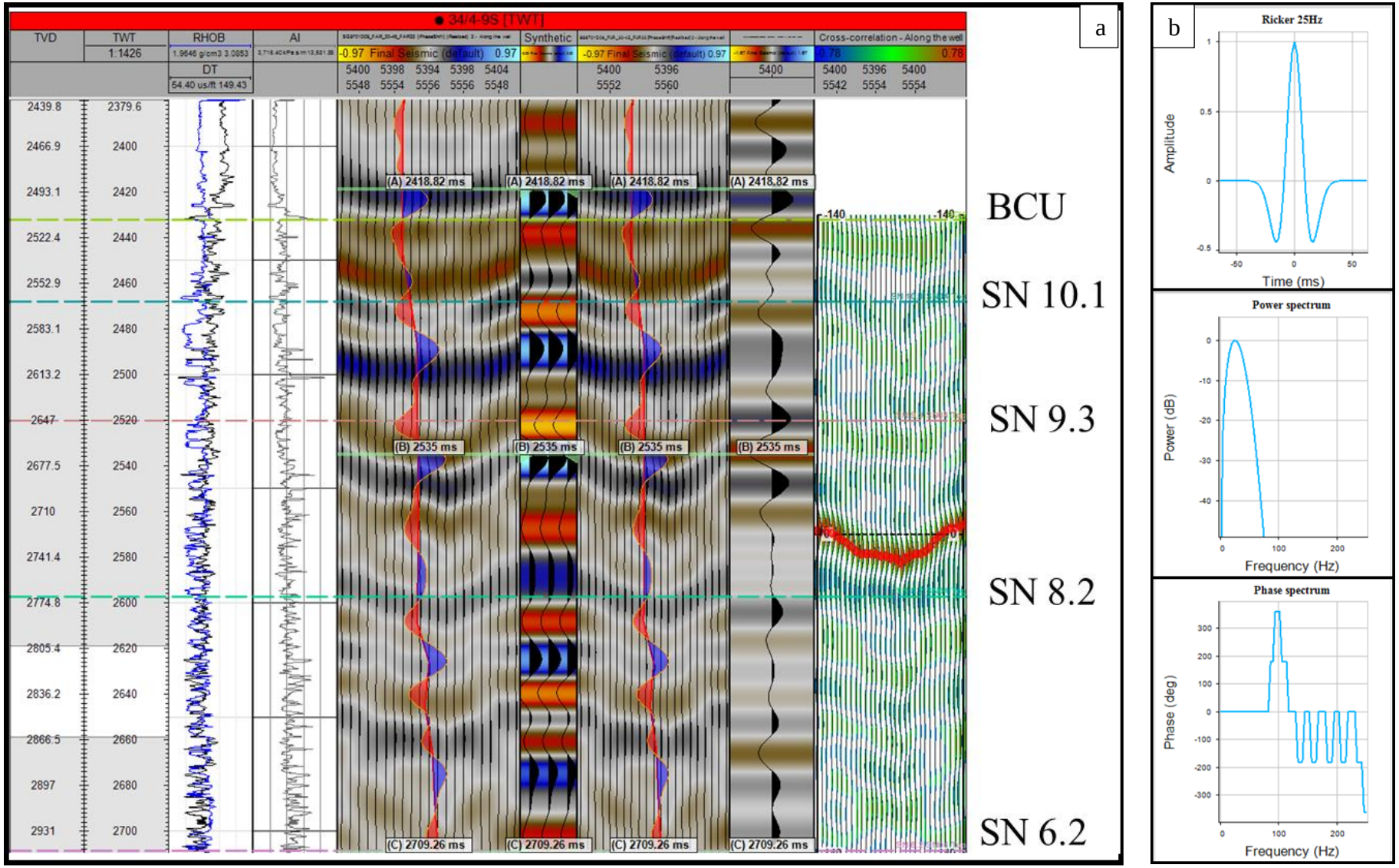

***Figure 6.16**: a.) Well tie section of well 34/4-9S b.) The wavelet used for the seismic ties of all the wells.*

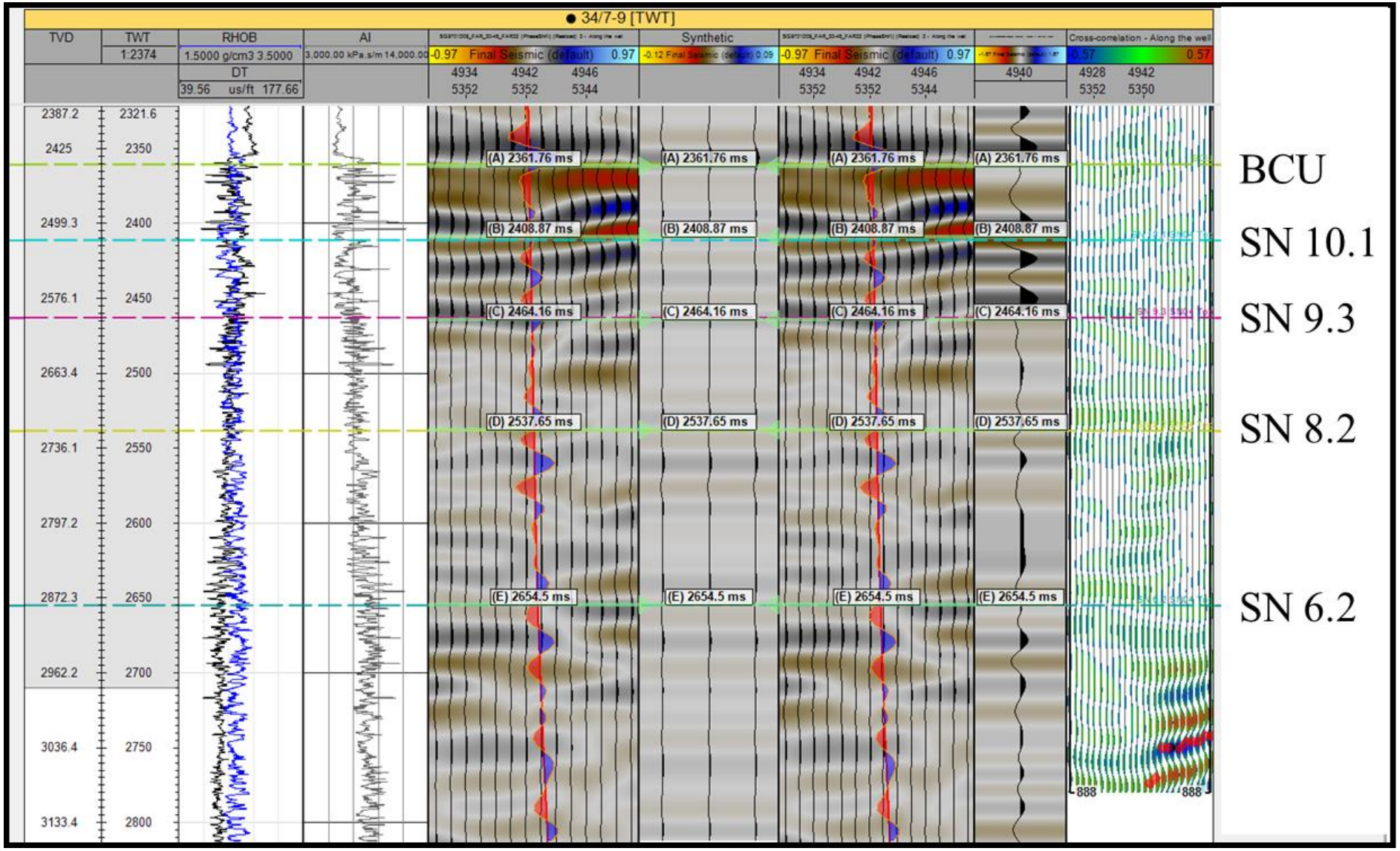

***Figure 6.17**: Well tie section of the well 34/7-9*

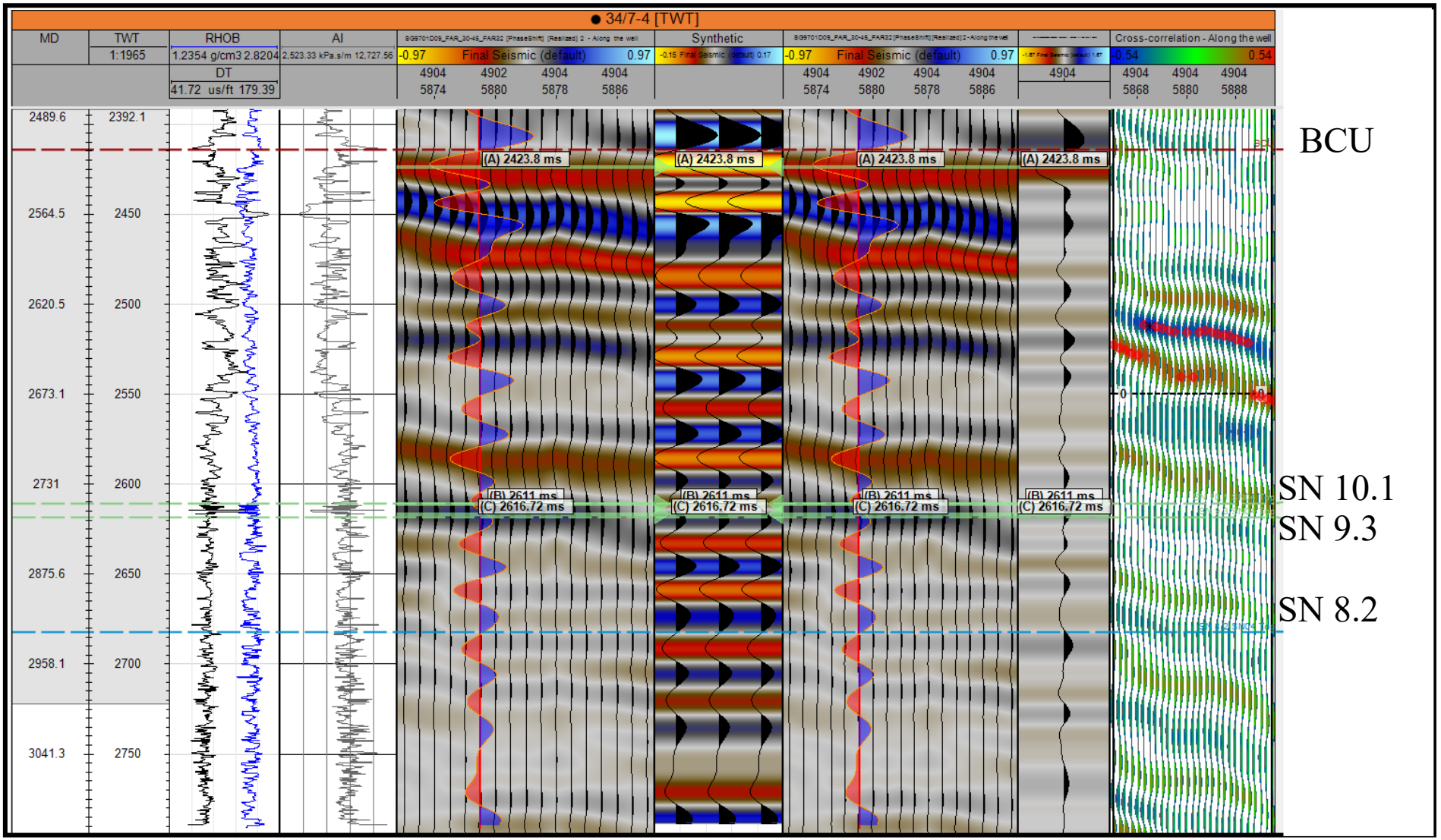

***Figure 6.18**: Well tie section of the well 34/7-4*

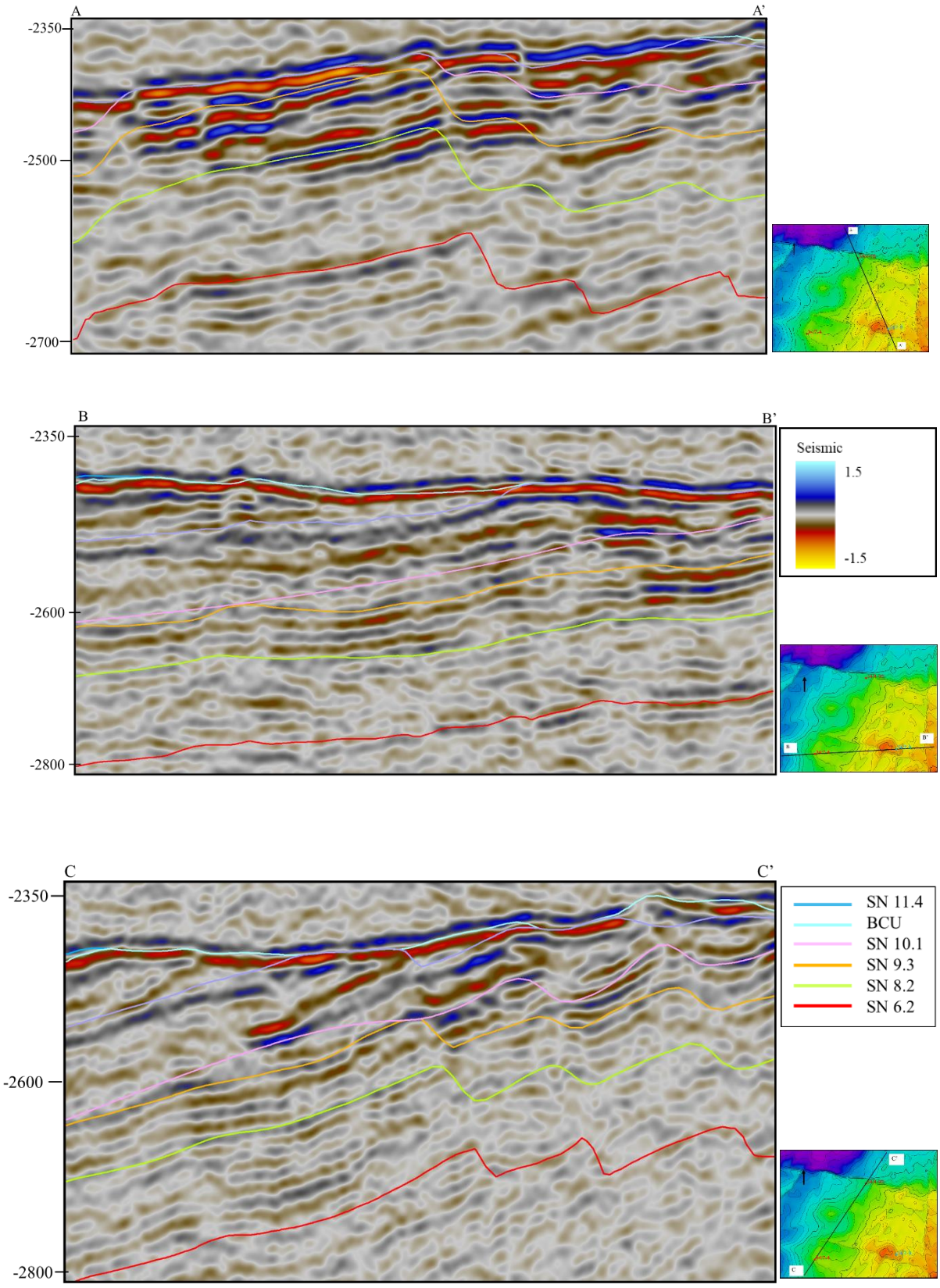

Figure 6.19: *Seismic sections A-A', B-B' and C-C' of the near stack seismic.*

6.3 Colored Inversion

An optimal operator with frequency corner points of 5-12-60-75 is used in the colored inversion process (Figure 6.20).

Figure 6.21 displays the color inverted intercept section generated from the near-mid stack. The acoustic impedance log is also displayed in the figure, filtered with the same frequencies to that of color inverted seismic. The hardening effect of top reservoir (BCU) is quite continuous and has a good match with the well log. The layers between well 34/4-9S and well 34/7-9 in the study area are sharply resolved with their boundaries. Specifically, in the interval of BCU to SN 9.3, the layers are well resolved, continuous and are consistent with the well log.

Figure 6.22 displays the color inverted intercept section generated from the mid-far stack. The acoustic impedance log is also displayed in the figure, filtered with the same frequencies to that of color inverted seismic. The hardening effect of BCU is similar to that of the near-mid color inverted intercept. The layers between well 34/7-4 and well 34/4-9S are more continuous but poorly resolved compared to that of inverted intercept of near-mid combination. However, there is a little decline in the resolution and better continuity of layers between well 34/4-9S and well 34/7-9 to that of the inverted near-mid intercept section. While comparing the color inverted near-mid and mid-far output, the changes in resolution and continuity of layers between well 34/7-4 and well 34/4-9S is stronger than that of between well 34/4-9S and well 34/7-9.

Figure 6.23 displays the color inverted gradient section generated from the near-mid stack. The gradient impedance log of well 34/4-9S is also displayed in the figure, filtered with the same frequencies to that of color inverted seismic. As expected, the

seismic section is quite noisy. The section between well 34/4-9S and well 34/7-9 is less noisy as compared to that of between well 34/7-4 and well 34/4-9S. Specifically, the noise content increases near the well 34/4-9S.

Figure 6.24 displays the color inverted gradient section generated from the mid-far stack. The gradient impedance log of well 34/4-9S is also displayed in the figure, filtered with the same frequencies to that of color inverted seismic. This seismic section is comparatively less noisy than that of the inverted gradient near-mid section. Better resolution and continuity of layers is observed between well 34/4-9S and well 34/7-9.

The provided interpretations were already on zero-crossing, thus the color inverted resulted the horizons to shift to the peaks/troughs.

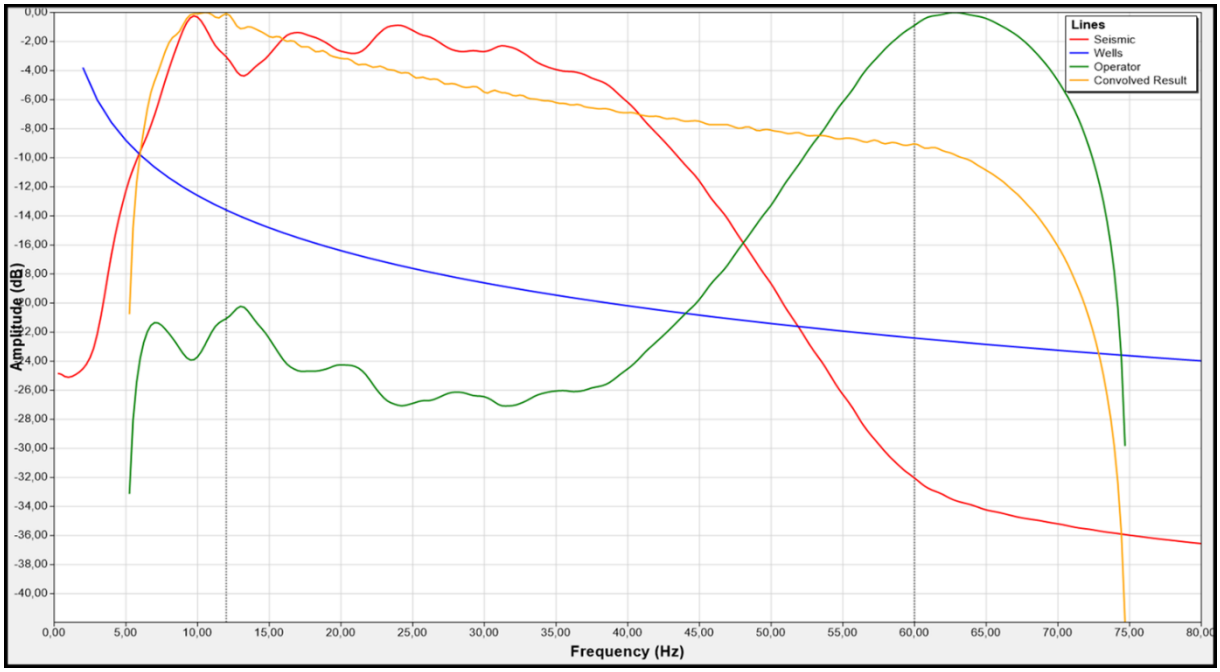

***Figure 6.20**: Operator used in Colored Inversion process.*

***Figure 6.21**: Crossection of intercept volume generated from near-mid stack displayed together with filtered AI log.*

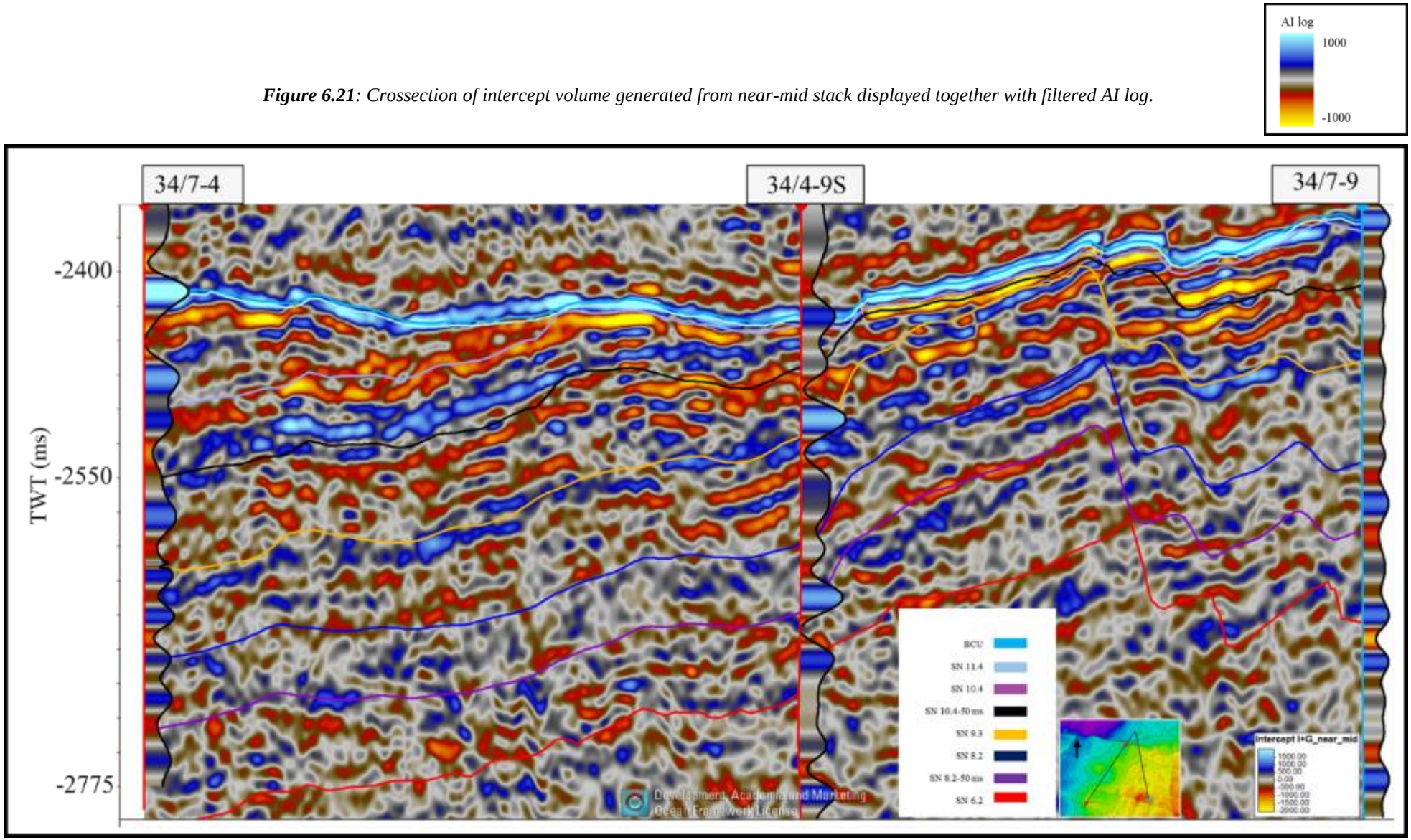

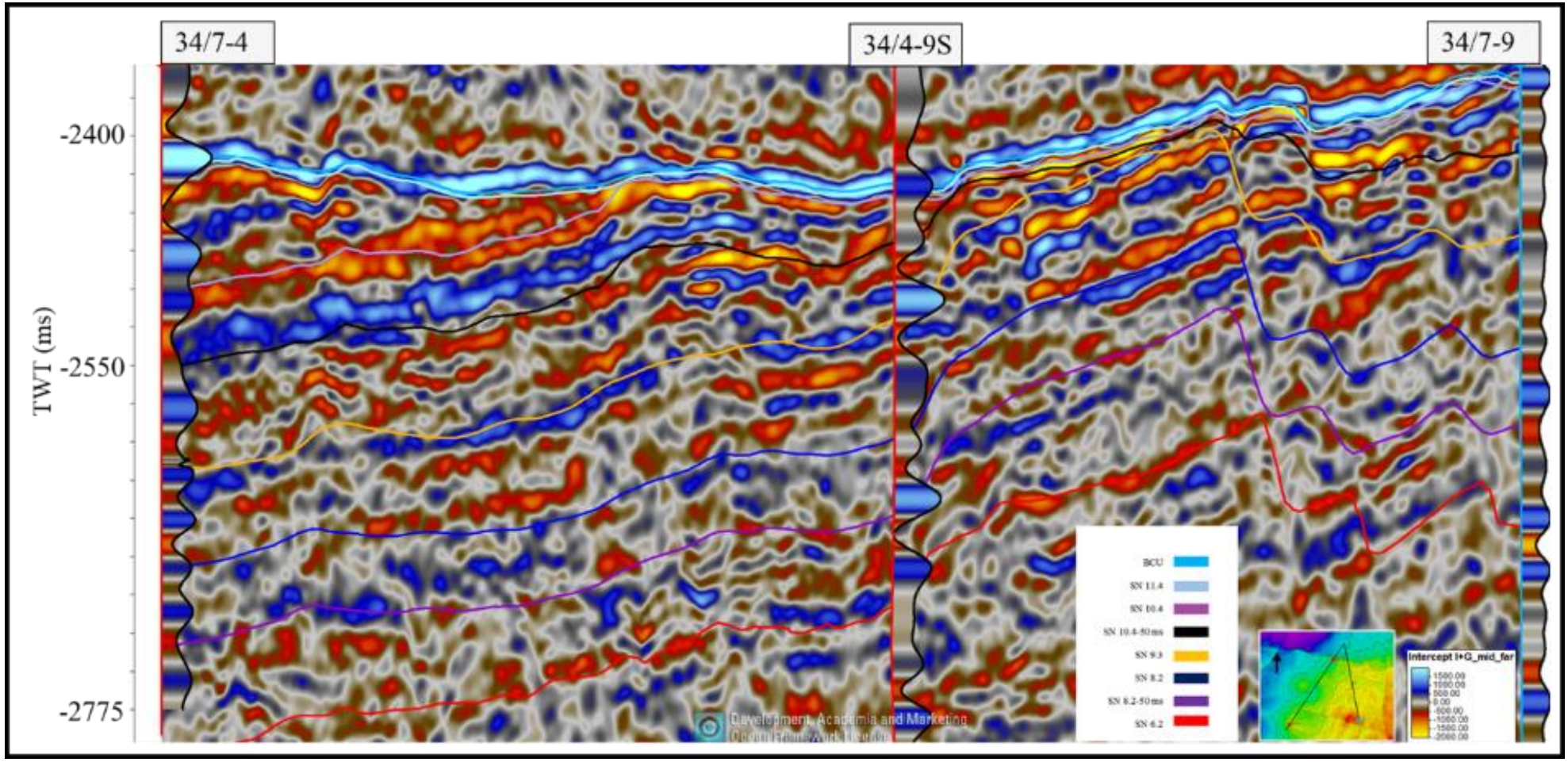

***Figure 6.22**: Crossection of intercept volume generated from mid-far stack displayed together with filtered AI log.*

***Figure 6.23**: Crossection of gradient volume generated from near-mid stack displayed together with filtered GI log.*

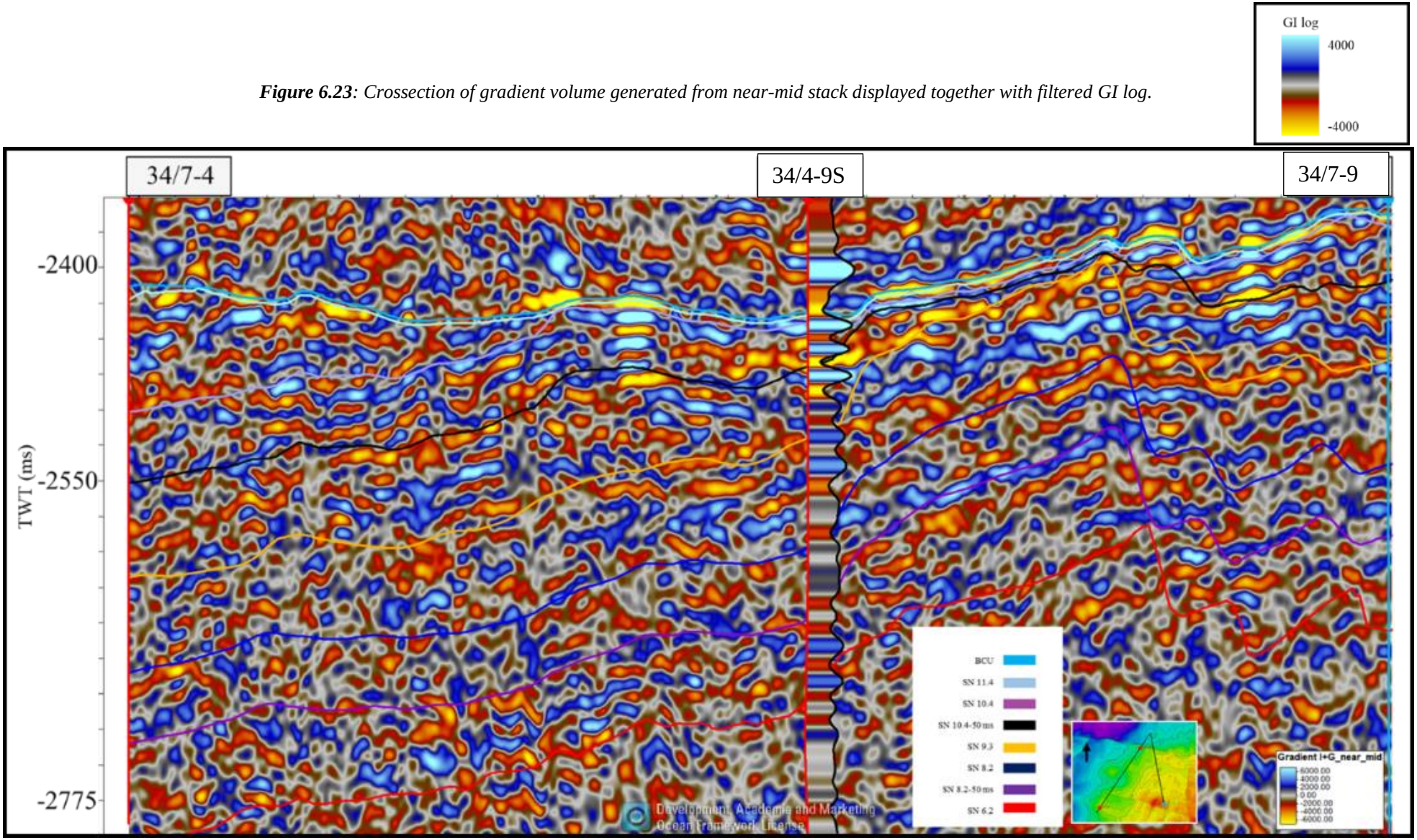

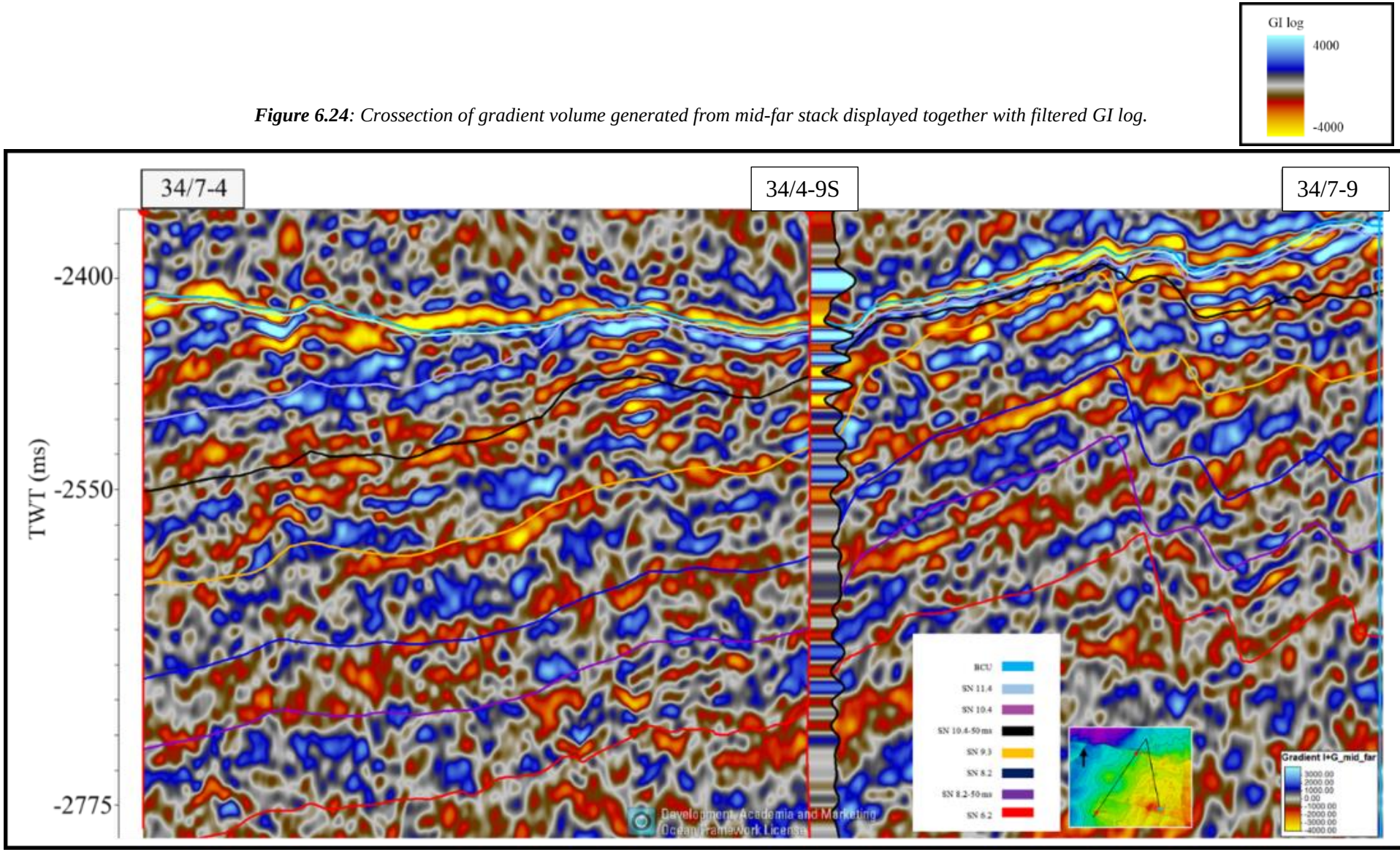

***Figure 6.24**: Crossection of gradient volume generated from mid-far stack displayed together with filtered GI log.*

6.4 Extended Elastic Impedance (EEI)

In figure 6.25, the target log Vshale, shows best correlation with EEI (42^0) well log. However, due to presence of anisotropy, different optimal chi angle is obtained for the two different stacks (near-mid and mid-far). EEI (10^0) from near-mid stack and EEI (20^0) seismic shows optimal correlation with EEI (42^0) well log.

Figure 6.26a shows the well section of well 34/4-9S with macrolayers (chapter 5.5.1), well logs and EEI (10^0) from both seismic and well log at seismic resolution. Both the EEI from seismic and well log have a good correlation. Figure 6.27 displays the seismic section of EEI (10^0), with all the wells and well logs such as volume of shale (Vsh), water saturation (Sw) are also displayed for comparison. It is observed that the reflectors in the areas where Vsh and Sw is low (suggesting hydrocarbons) gets brighter and is picked up well in all the wells. The background gets dimmer as compared to the fluid presence in the study area.

Figure 6.26b shows the well section of well 34/4-9S with macrolayers, well logs and EEI (20^0) from seismic and well log. The correlation of EEI (42^0) from well log with EEI (20^0) from mid-far is better than that of EEI (10^0) from near-mid. Figure 6.28 displays the seismic section of EEI (20^0), with all the wells and well logs such as volume of shale (Vsh), water saturation (Sw) are also displayed for comparison. It is noticed that the reflectors in the areas where Vsh and Sw is low (suggesting hydrocarbons) gets brighter and is picked up well in all the wells 34/4-9S and 34/7-4, but there is a misalignment in well 34/7-9. Additionally, the continuity of the reflectors is poor as compared to that of the near-mid output. But the background gets more dimmer as compared to that of EEI (10^0) from near-mid.

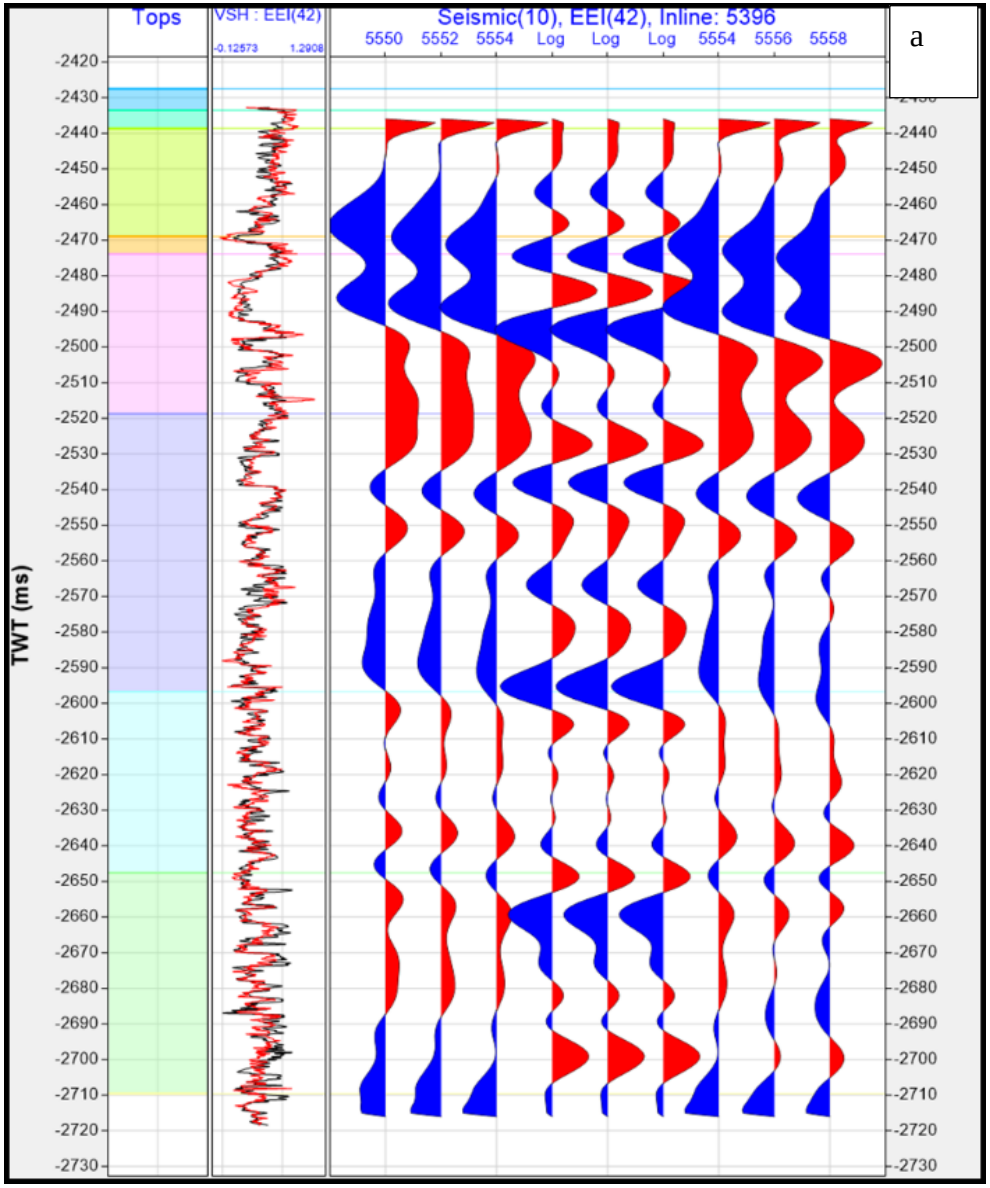

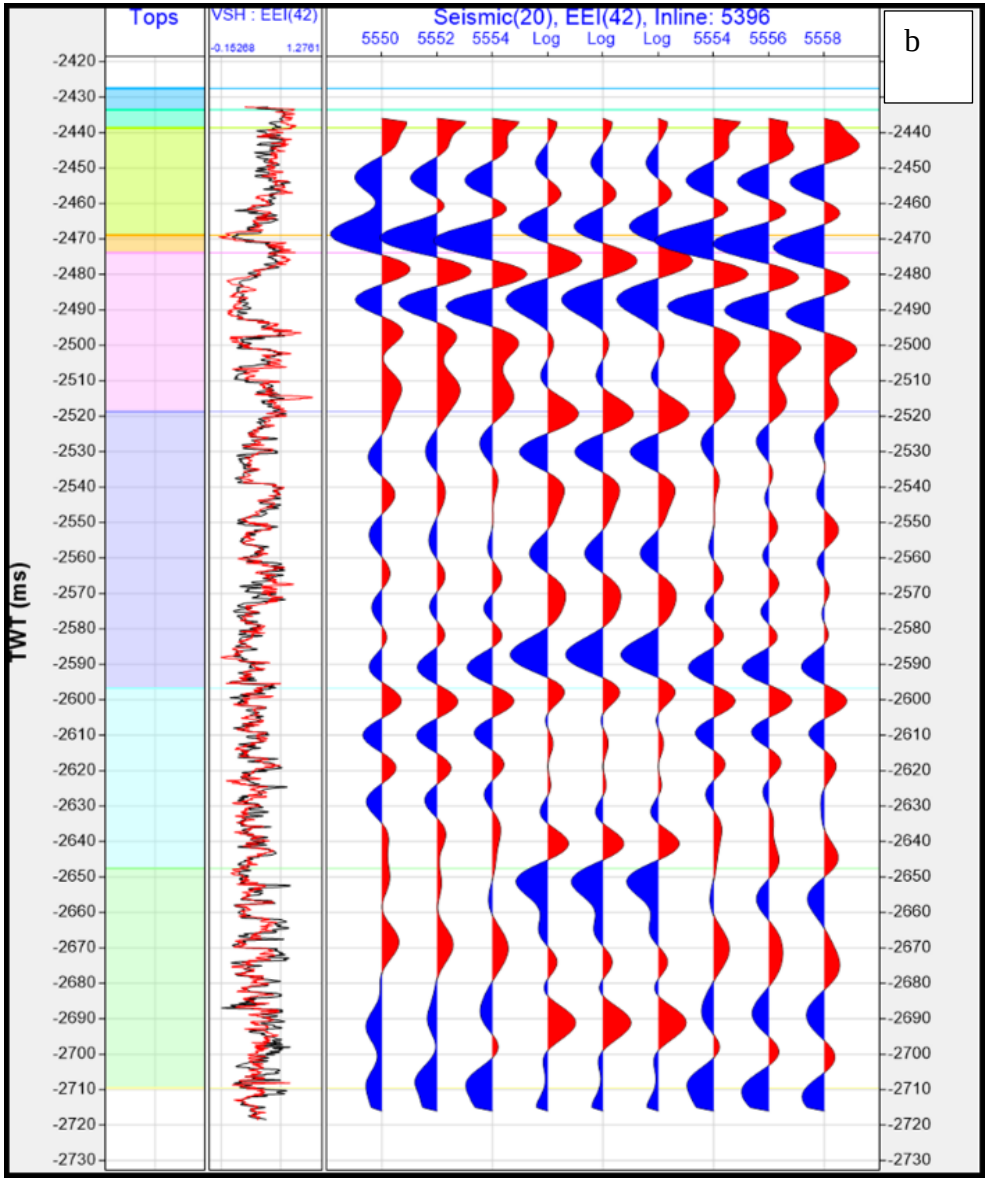

***Figure 6.25**: EEI angle analysis of a.) Near-Mid and b.) Mid-Far*

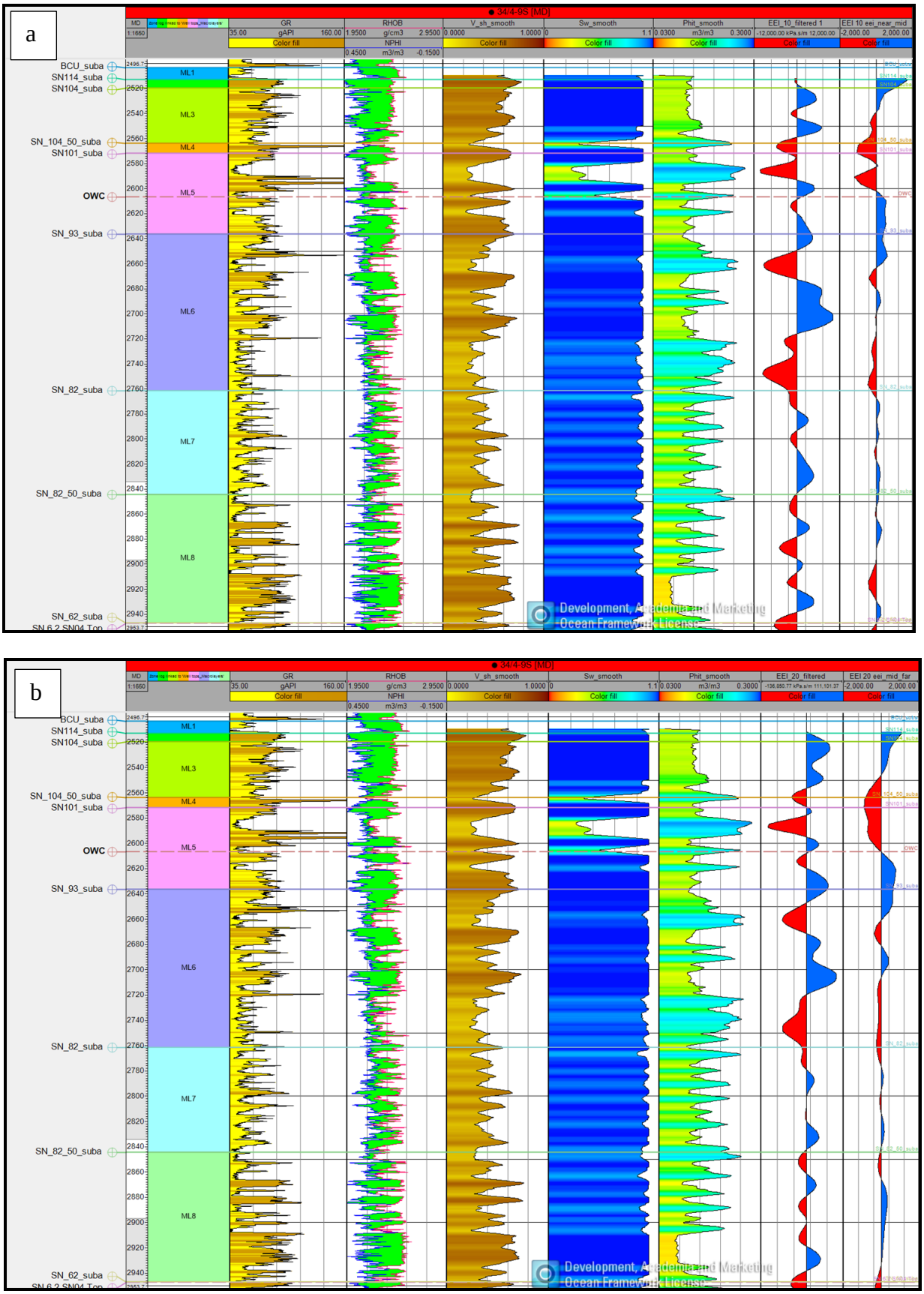

Figure 6.26: *Well section with Macrolayers (defined in Chapter 6.5) and a.) EEI 10^0 stack converted to log compared with filtered EEI (10^0) log. b) EEI 20^0 stack converted to log compared with filtered EEI (20^0) log*

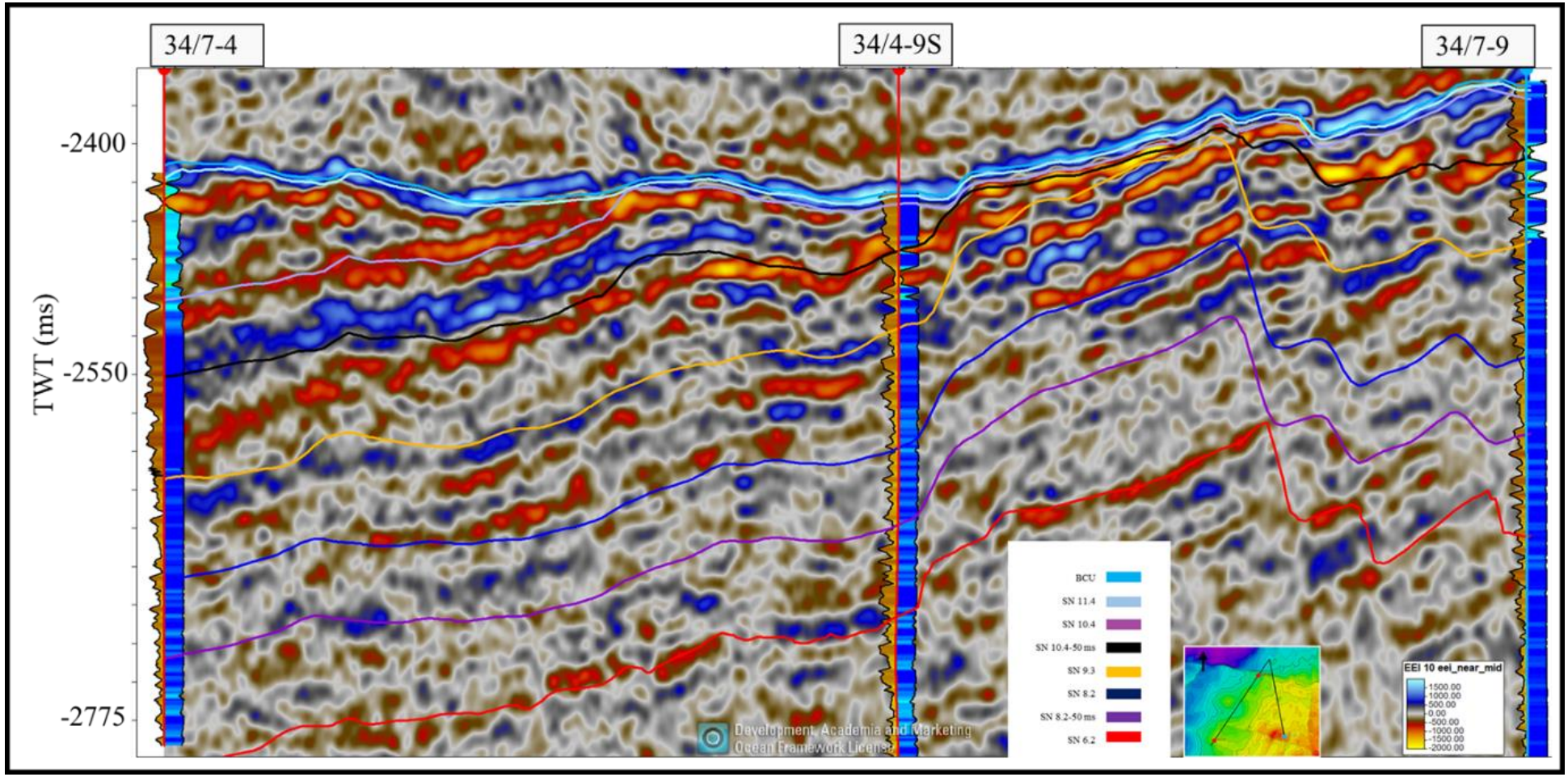

***Figure 6.27**: Crossection of EEI (10^0) generated from near- mid stack displayed together with Vsh and Sw logs.*

***Figure 6.28**: Crossection of EEI (20^0) generated from near- mid stack displayed together with Vsh and Sw logs.*

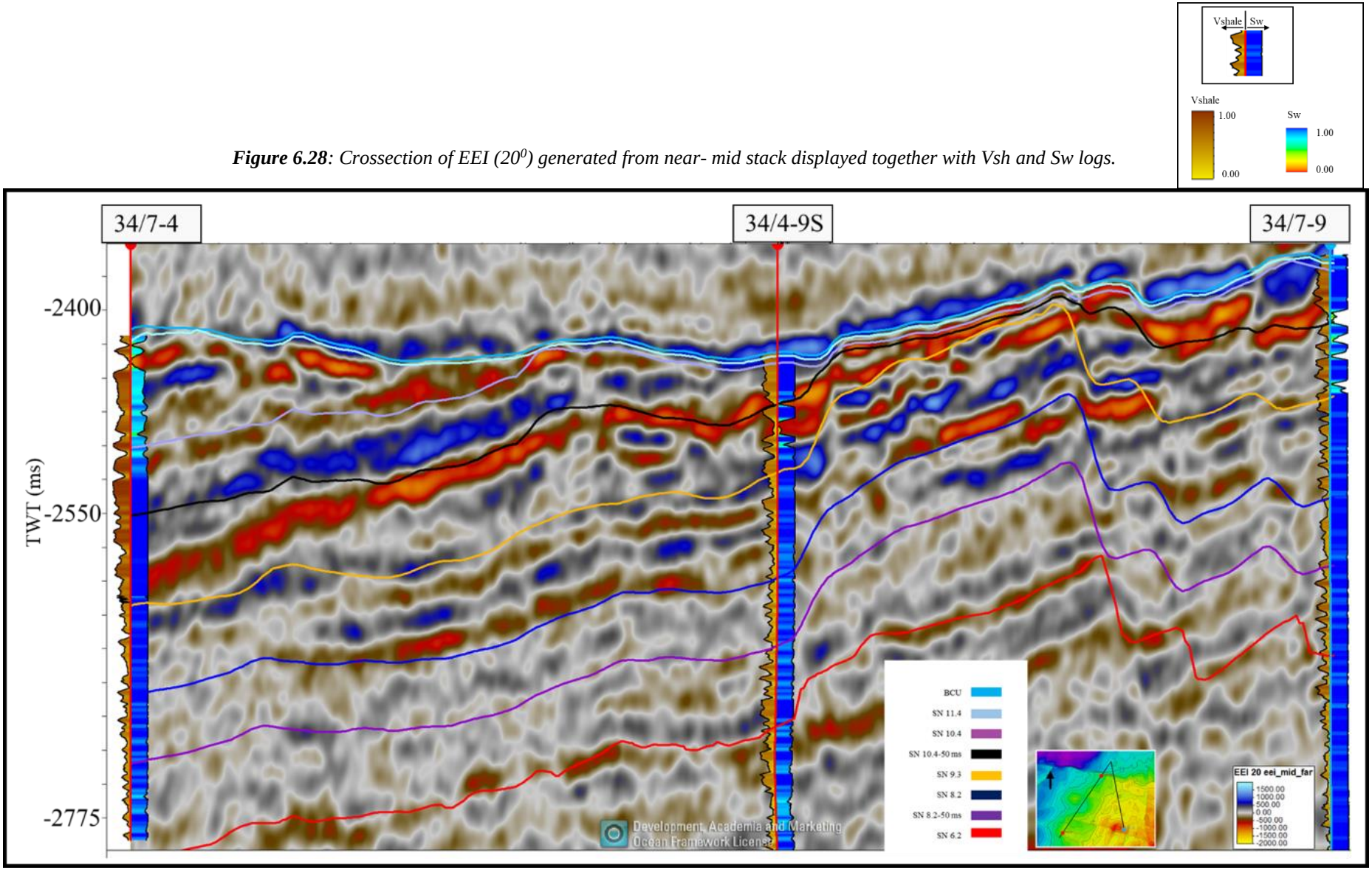

6.5 ODiSI

6.5.1 Rock Physics QC

Figure 6.29, 6.30 and 6.31 displays the global rock physics trends used for sand, shale and shaly sand respectively. The red data points are from the input well, while the black data points are for the pseudo well at that location. While setting up the trend for each lithofacies, care has been taken that the pseudo well data cloud boundaries (standard deviation lines) contains proportion of the real well data cloud. The rock physics trends are global and not defined based on each macrolayer.

The well log data from well 34/4-9S was used for QC purpose of the pseudo well log data generated from the rock physics trends. Figure 6.32 shows the input and pseudo well log data overlain against each other. It is noticed that pseudo Vshale, porosity, density, dry bulk modulus (K_dry) and shear modulus (G) log has a good match with the input as compared to other logs. Vp, Vs, GI log has some areas of misalignments with the input log.

Figure 6.33 displays different crossplots of petrophysical properties like Vp, density, AI, GI for both input and pseudo well. It is observed in the crossplot of density-Vp, that the separation of pseudo well data points for different facies follows the same trend as compared to that of the input well, however, there is a little mismatch in the range of the values of the properties for the pseudo well data points in comparison to input well. In addition, in the crossplot of AI-GI, the pseudo well data doesn’t have a major overlap between shaly sand and shale data points as the input data. However, the range of shaly sand and shale data points follow that of the input data, unlike the sand data points. Overall, the pseudo well data follows the input well data trend.

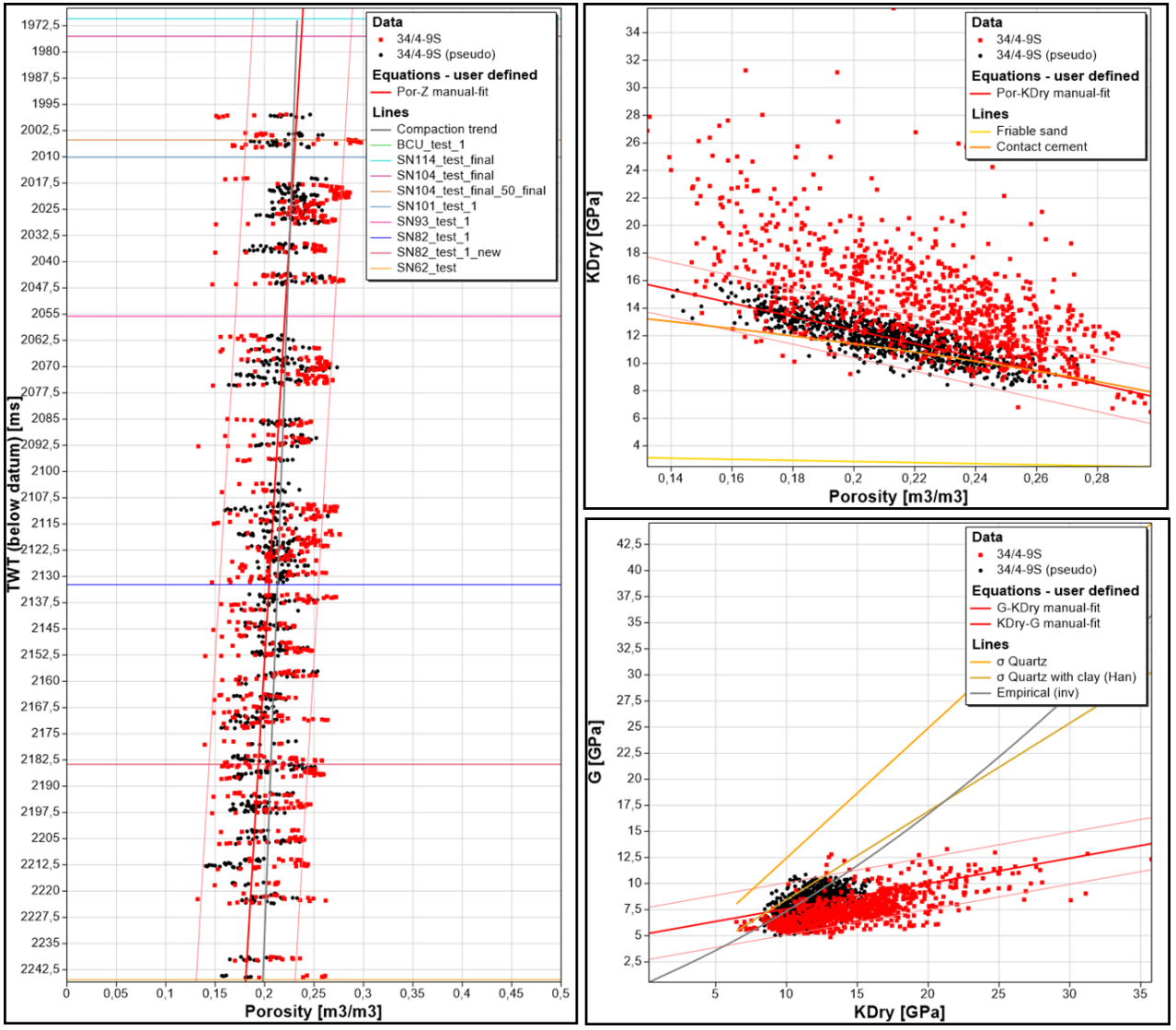

***Figure 6.29**: Rock physics trends for sand lithofacies.*

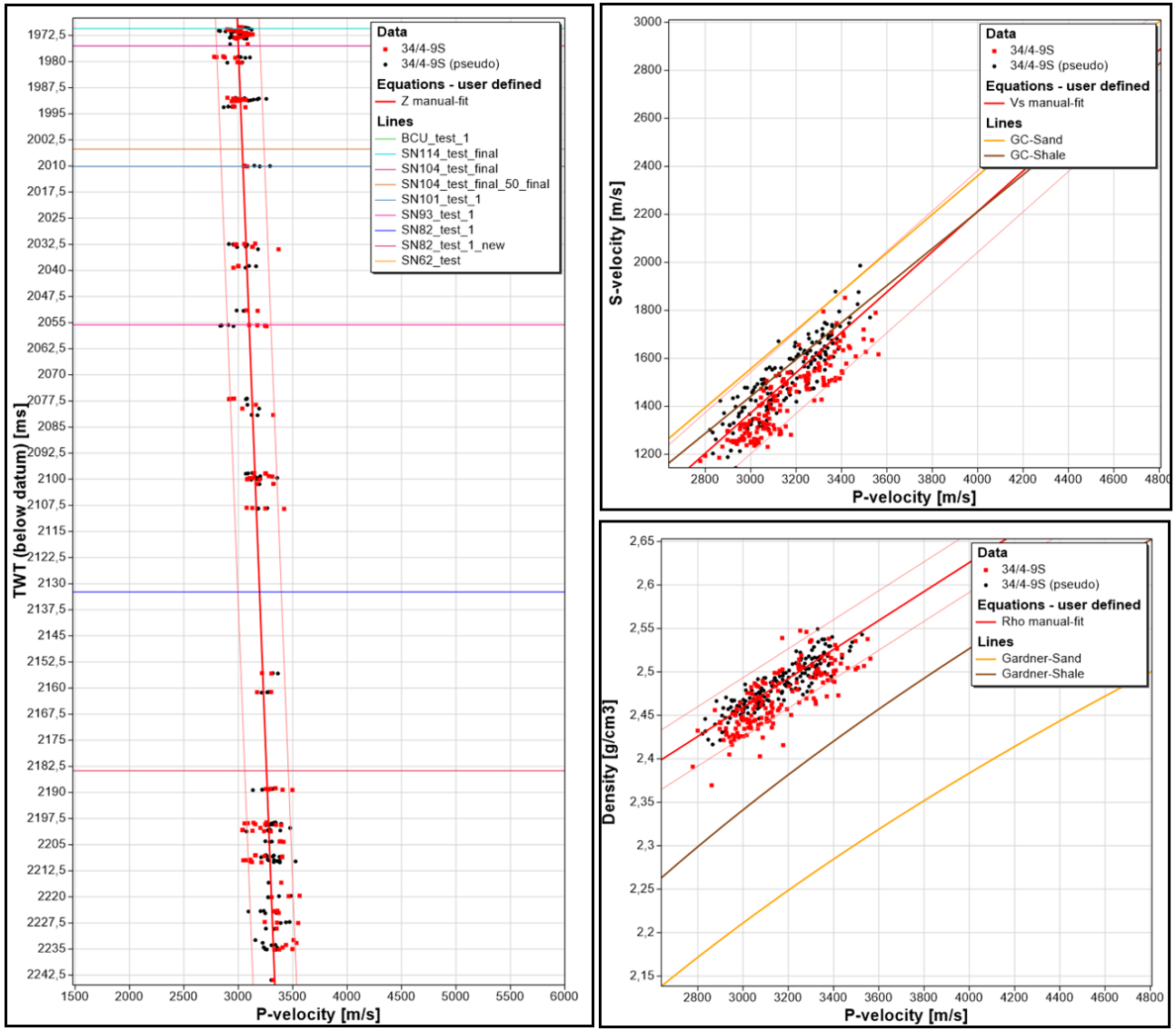

***Figure 6.30**: Rock physics trends for shale lithofacies.*

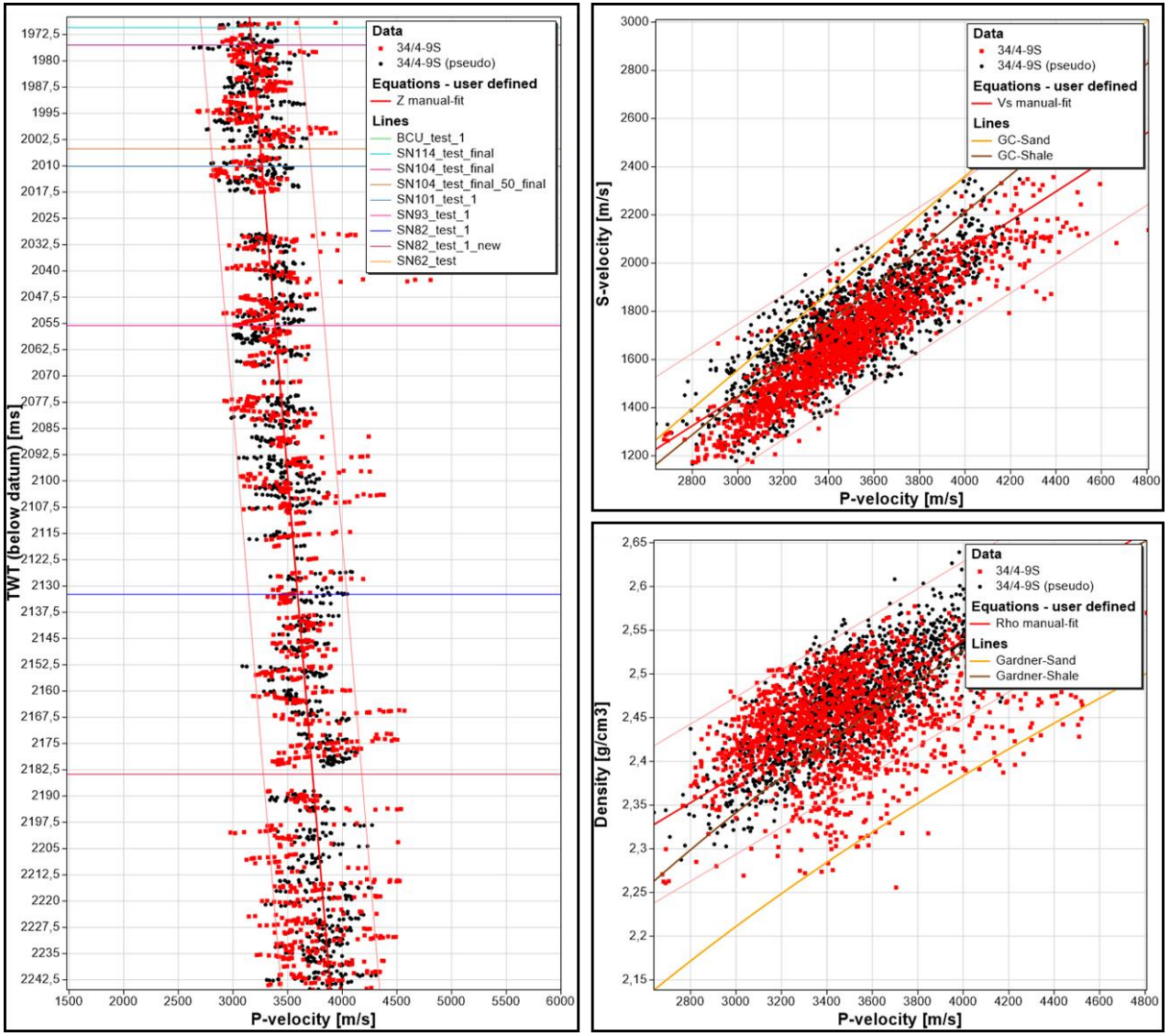

***Figure 6.31**: Rock physics trends for shaly sand lithofacies.*

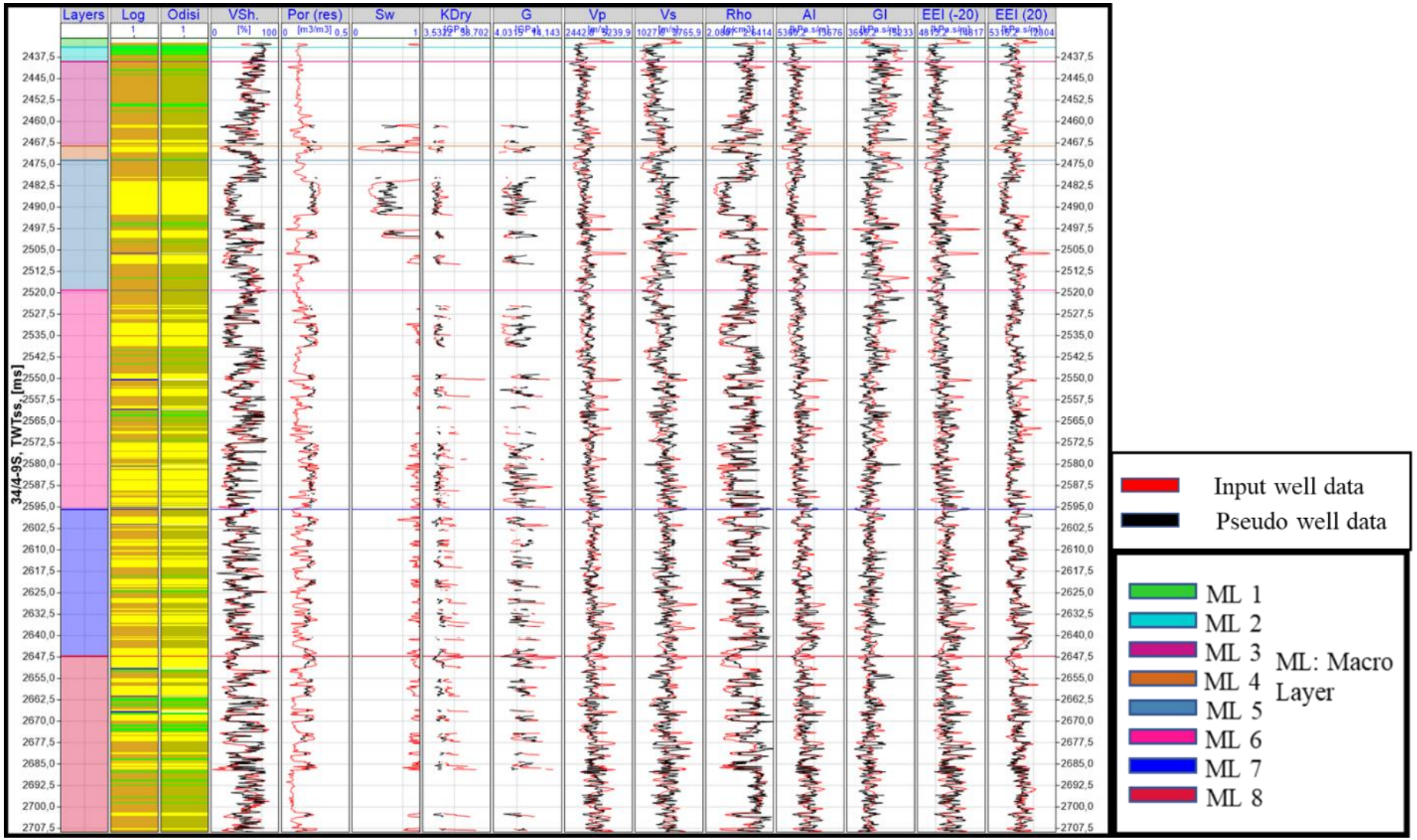

***Figure 6.32**: Petrophysical well log motif for both input and pseudo well.*

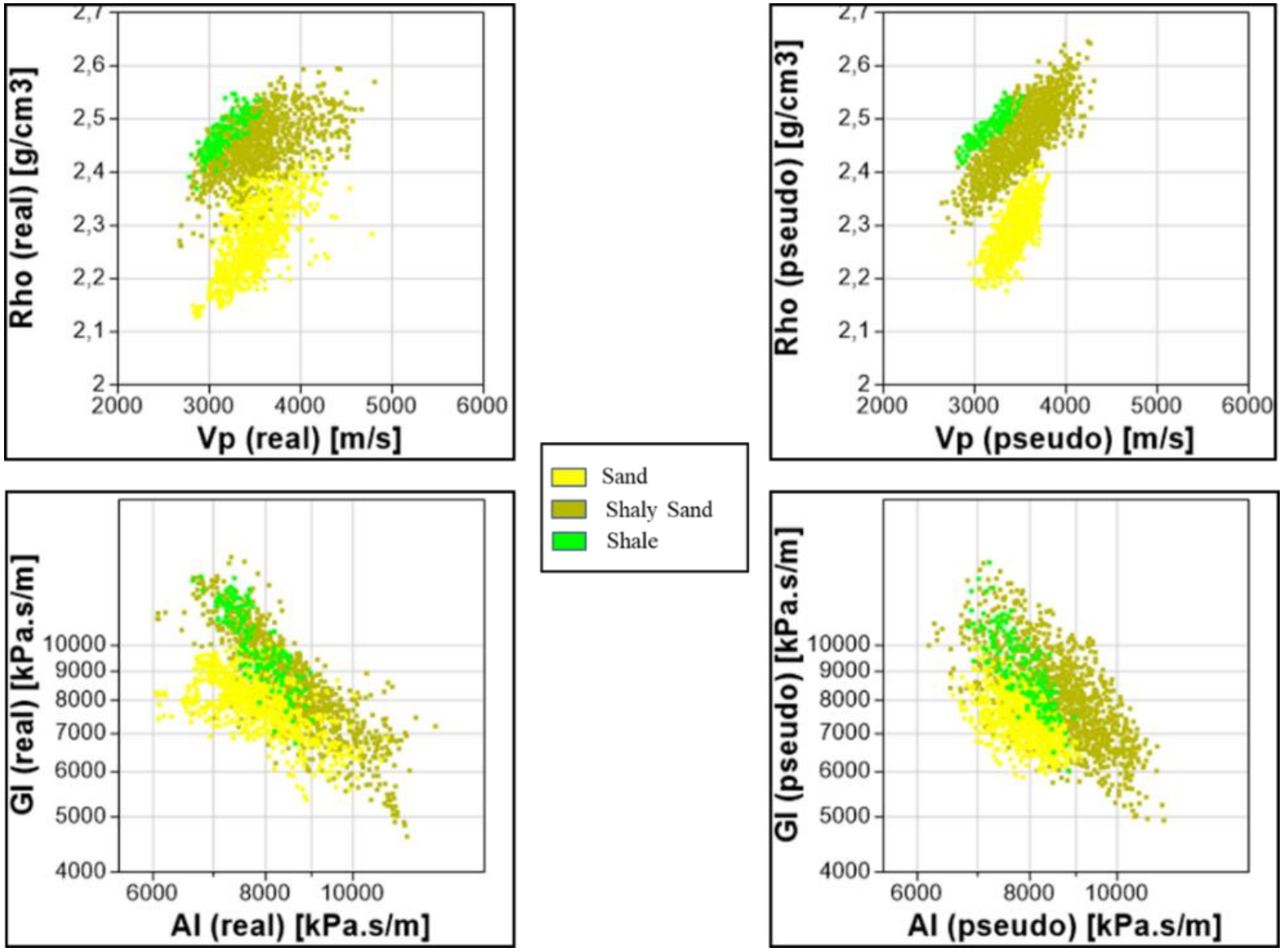

***Figure 6.33**: Crossplot of petrophysical parameters for both input and pseudo well*

6.5.2 Statistics QC

Figure 6.34 shows the transition probability matrix used for the facies transition in each macro layer for all the pseudo wells. The repeated facies (probability of appearing sand after sand) probability was intentionally assigned non zero values to introduce variability. The transitions were measured at the well location were observed, and subsequently modified to remove bias.

Figure 6.35 displays the values used to incorporate bed thicknesses of the facies in each macro layer for all the pseudo wells. The parameters are different in each macrolayer. Maximum thickness, proportion of each facies and an average bed thickness factor were assigned considering the maximum thickness and proportion of facies at the real well locations. However, the set of values measured and used were made to be different from

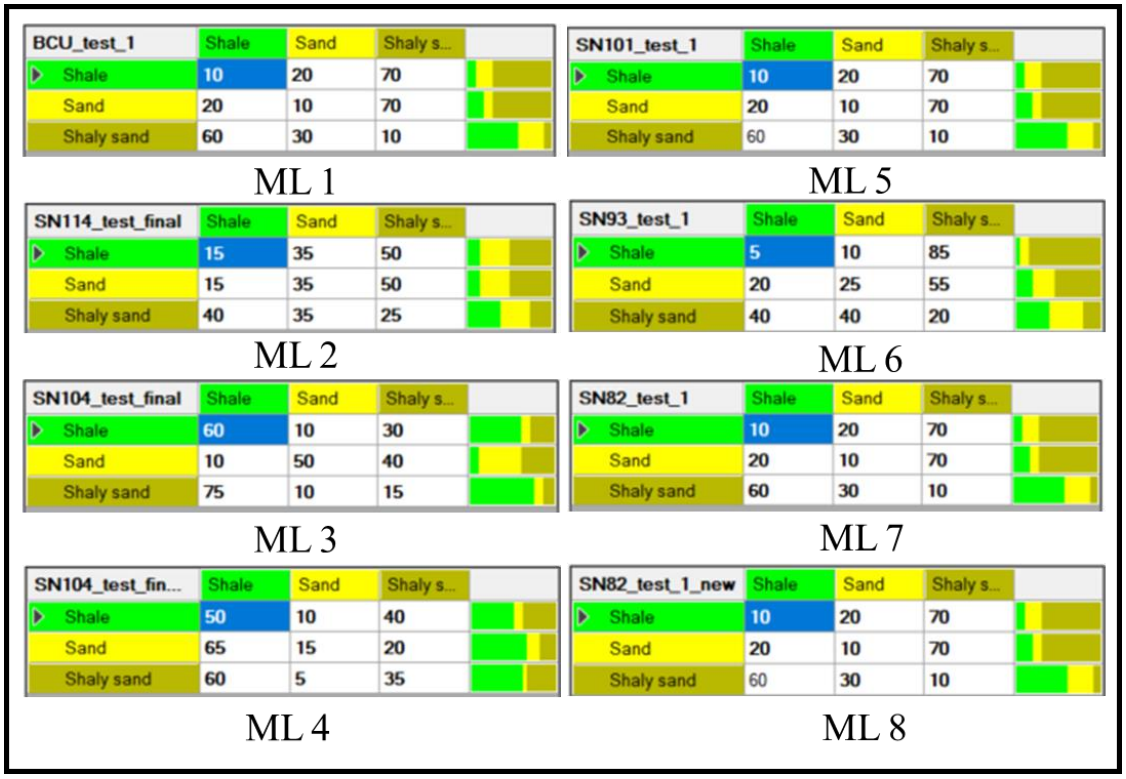

***Figure 6.34**: Facies transitional matrix for each macrolayer (ML).*

each other to avoid any bias. Minimum thickness and standard deviations for each facies were assigned as constant values of 0.5 ms and 5 respectively in all the macrolayers.

Figure 6.36 shows the lithology columns for 100 pseudo wells built at the well location of well 34/4-9S. Good amount of variability is observed in the pseudo wells. In addition, figure 6.36 displays the proportions of Net to Gross (NtG) in each macrolayer. It is noticed that all the macro layers have varied NtG.

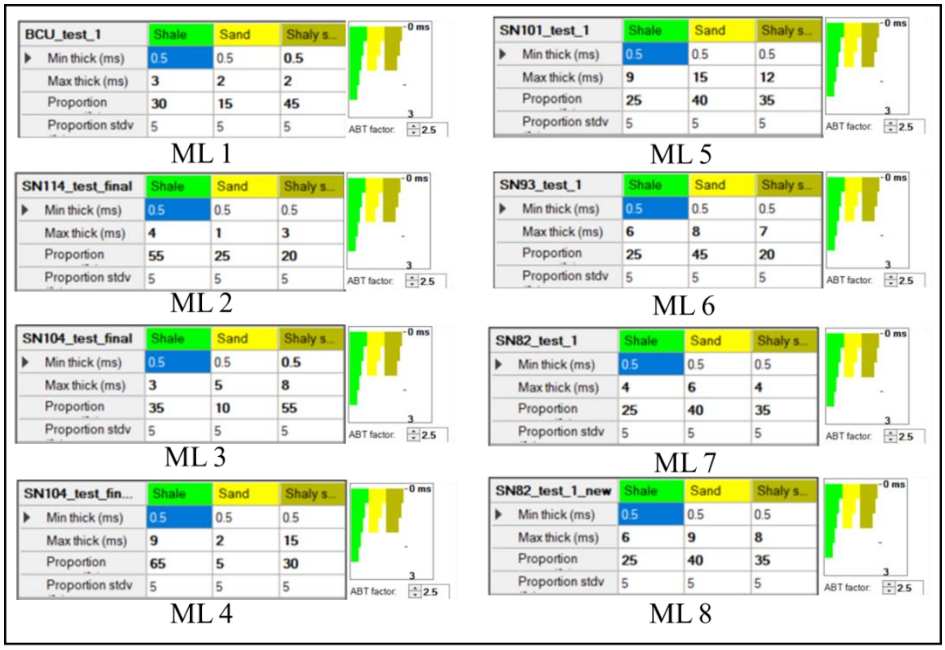

***Figure 6.35**: Facies proportions in each macro layer (ML).*

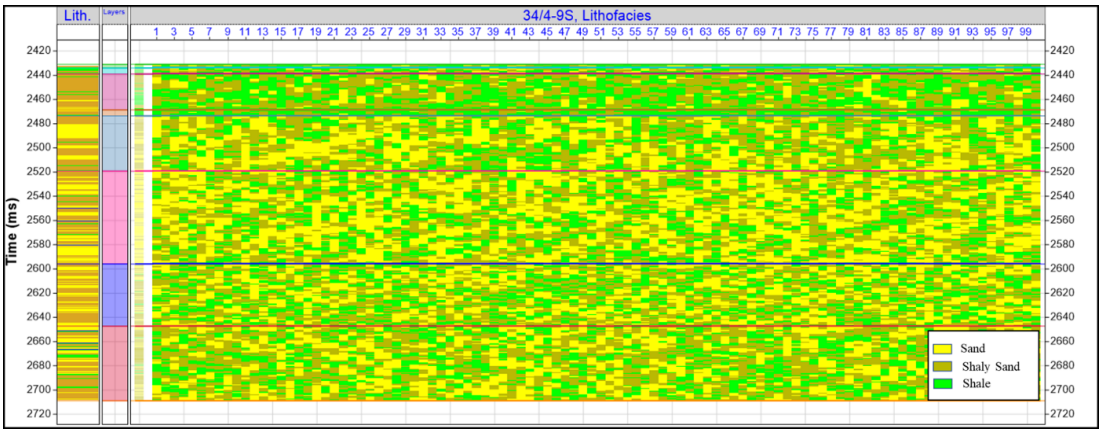

***Figure 6.36**: 100 pseudo wells with lithological column built from the Prior Model at the location of input well 34/4-9S*

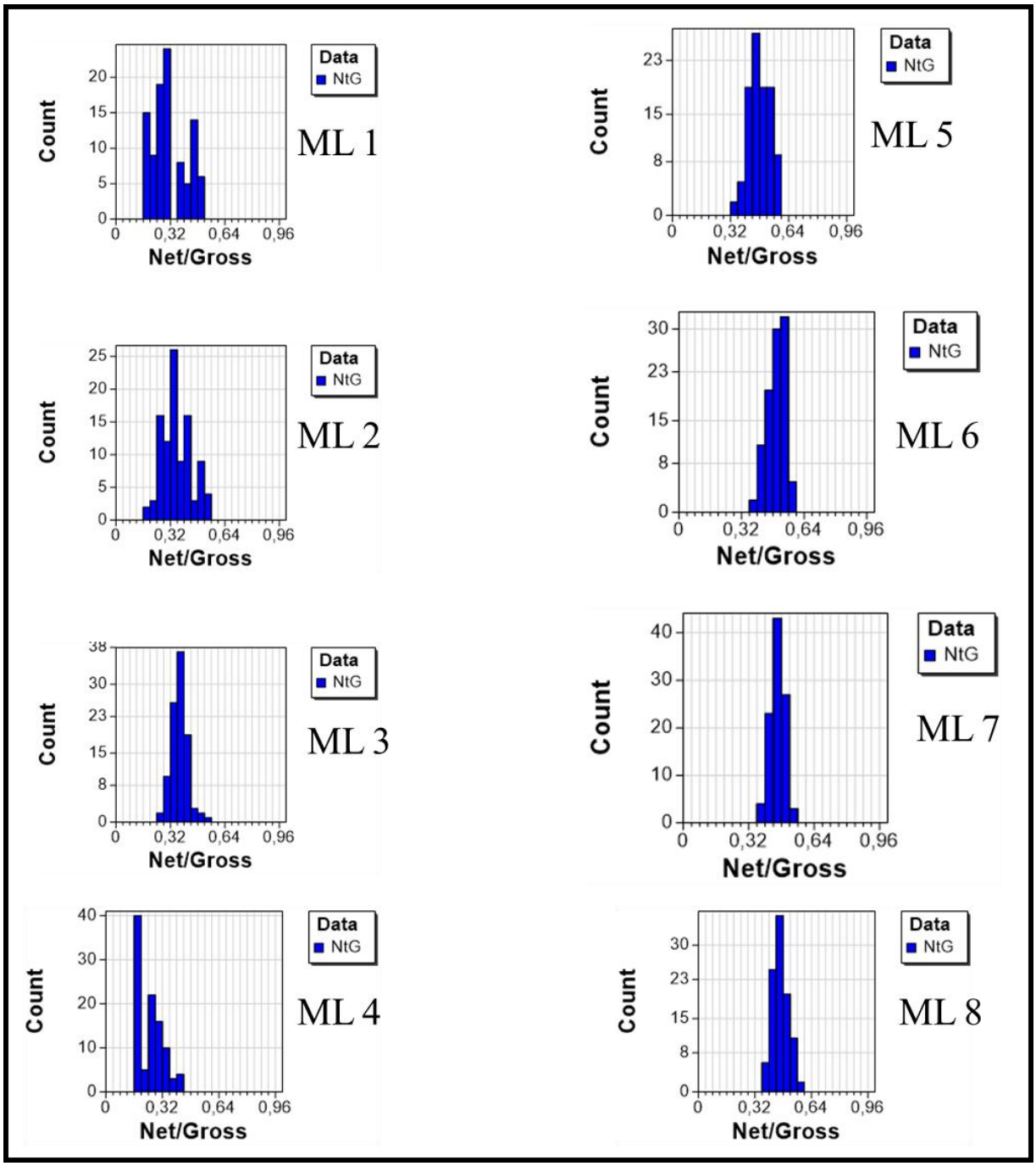

Figure 6.37*: Variability of parametrized Net to Gross in different macro layers (ML)*

6.5.4 Trace matching/ Inversion QC

10,000 pseudo wells are generated for each seismic trace, and the best 100 among them are used for averaging. The Inversion QC was performed by inverting the seismic trace at all the well locations using both the EEI volumes.

6.5.4.1 Inversion QC using EEI (10^0) at well location of 34/4-9S

Figure 6.38 displays the properties generated by inverting the trace of EEI (10^0) at the well location of well 34/4-9S. The results on the prediction of lithology at the well location in each macrolayer (ML) are as follows:

- ML-1, ML-2 and ML-4 don't have a good match with the input lithology, possibly due to the small width of these macrolayers at this location.
- The input lithology in ML-3 is dominated by shaly sand with small proportion of sand and shale. However, it predicts more shale in the macrolayer as compared to the input lithology. The predicted sand location is aligned with its input counterpart location.
- ML-5 is important as it contains the fluid contact. There is a good match of the predicted sand with the input sand. However, there are some misalignments towards the end of ML-5.
- The thin layers of shaly sand in ML-6 is not picked in the prediction. In addition, there are some misalignments, where sand is predicted in place of shaly sand and vice versa.
- ML-7 and ML-8 have decent match with some minor misalignments.

The results on the prediction of pseudo well logs and synthetics are as follows:

- The predicted volume of shale (Vsh) log has a poor match in ML-6, a little misalignment is observed in ML-4 and in the beginning of ML-5. It has a good match in the corresponding location of sand (fluid contact) in ML-5. In ML-7 and ML-8, the predicted values are lower than actual, but the log motif is similar, and they fall within the standard deviation (SD) lines.
- Predicted porosity, water saturation (Sw) and Vp log has a good match.
- Predicted Vs log is misaligned in ML-4 and early part of ML-5. It has a decent match in the other macrolayers.
- Predicted density log is mismatched in ML-4 and has some minor misalignments in the other macrolayers.
- The synthetic and seismic matches the motif, however there are some amplitude differences possibly due to incorrect scalar. The amplitude values get similar below ML-5 as observed in the residual.

6.5.4.2 Inversion QC using EEI (10^0) at well location of 34/7-9

Figure 6.39 displays the properties generated by inverting the trace of EEI (10^0) at the well location of well 34/7-9. The results on the prediction of lithology at the well location in each macrolayer (ML) are as follows:

- ML-1, ML-2 and ML-4 predicts only shaly sand and don't show a good match with the input lithology.
- ML-3 predicts more sand but in incorrect location. Thin layers of shale present in the input lithology are not predicted.

- ML-5 has a good match of sand and this macrolayer contains the fluid contact. Thin layers of shaly sand are also captured.
- ML-6 predicts more shale and less shaly sand. The predicted thin layers of shale are misaligned. The sand location predictions are good.
- ML-7 and ML-8 provides a good match with the input lithology.

The results on the prediction of pseudo well logs and synthetics are as follows:

- Vsh log predictions are a little higher in the end of ML-3 and ML-4. In ML-4 the input log is outside of the SD lines. ML-6 and ML-8 have a good match, whereas ML-6 is poorly matched.
- Porosity, Sw and Vp log shows a decent match.
- Density log has good match in all the macrolayers except ML- 3, ML-4 and ML-7.
- Synthetic has a good match with the seismic and the residual is minimal.

6.5.4.3 Inversion QC using EEI (10^0) at well location of 34/7-4:

Figure 6.40 displays the properties generated by inverting the trace of EEI (10^0) at the well location of well 34/7-4. The results on the prediction of lithology at the well location in each macrolayer (ML) are as follows:

- ML-1 and ML-2 has increased width at the well location as compared to the previous two, and it predicts thin layers of shale and shaly sand, but ML-1

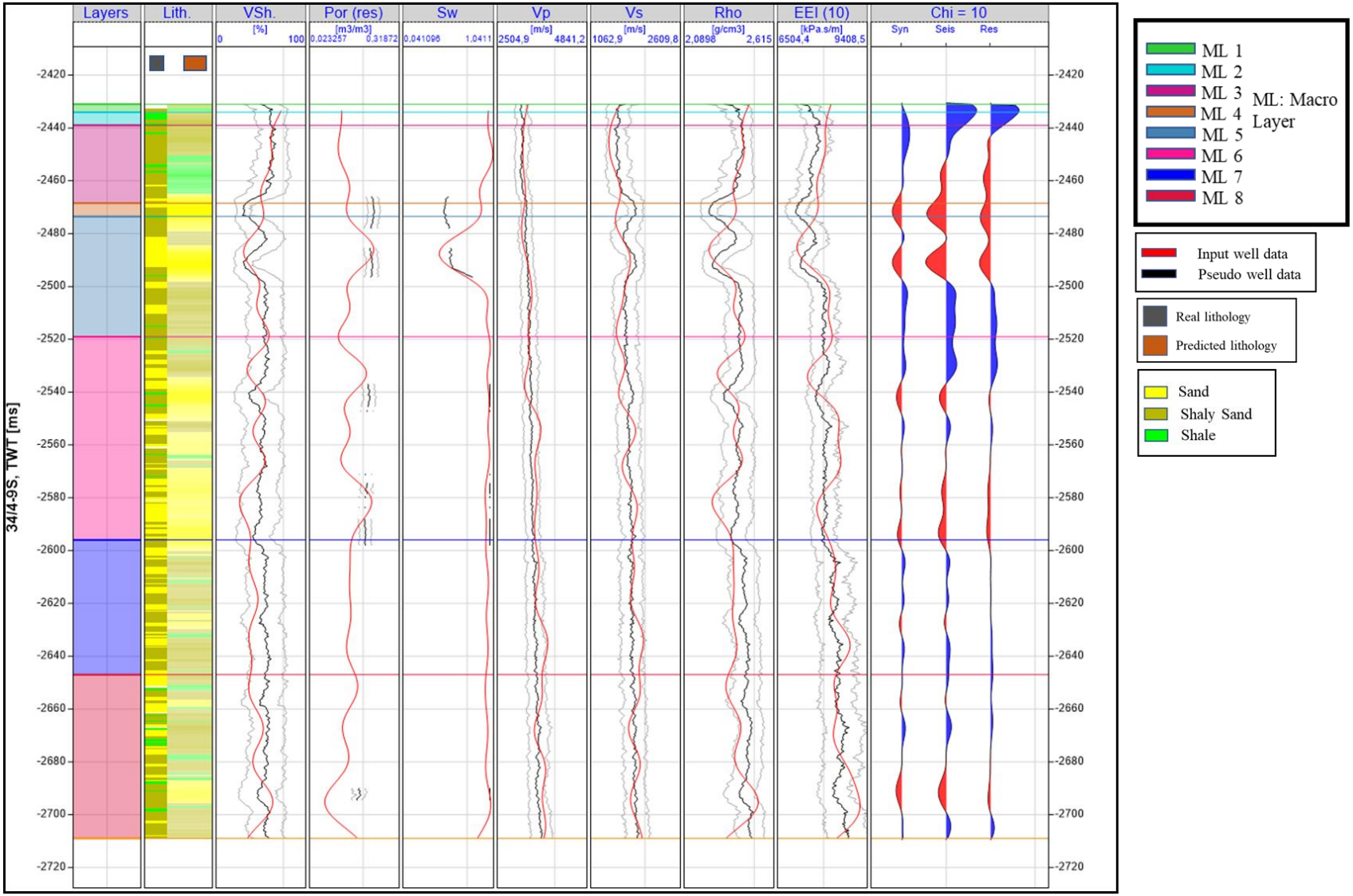

***Figure 6.38**: Properties generated by inverting a trace of EEI (10^0) at the location of well 34/4-9S.*

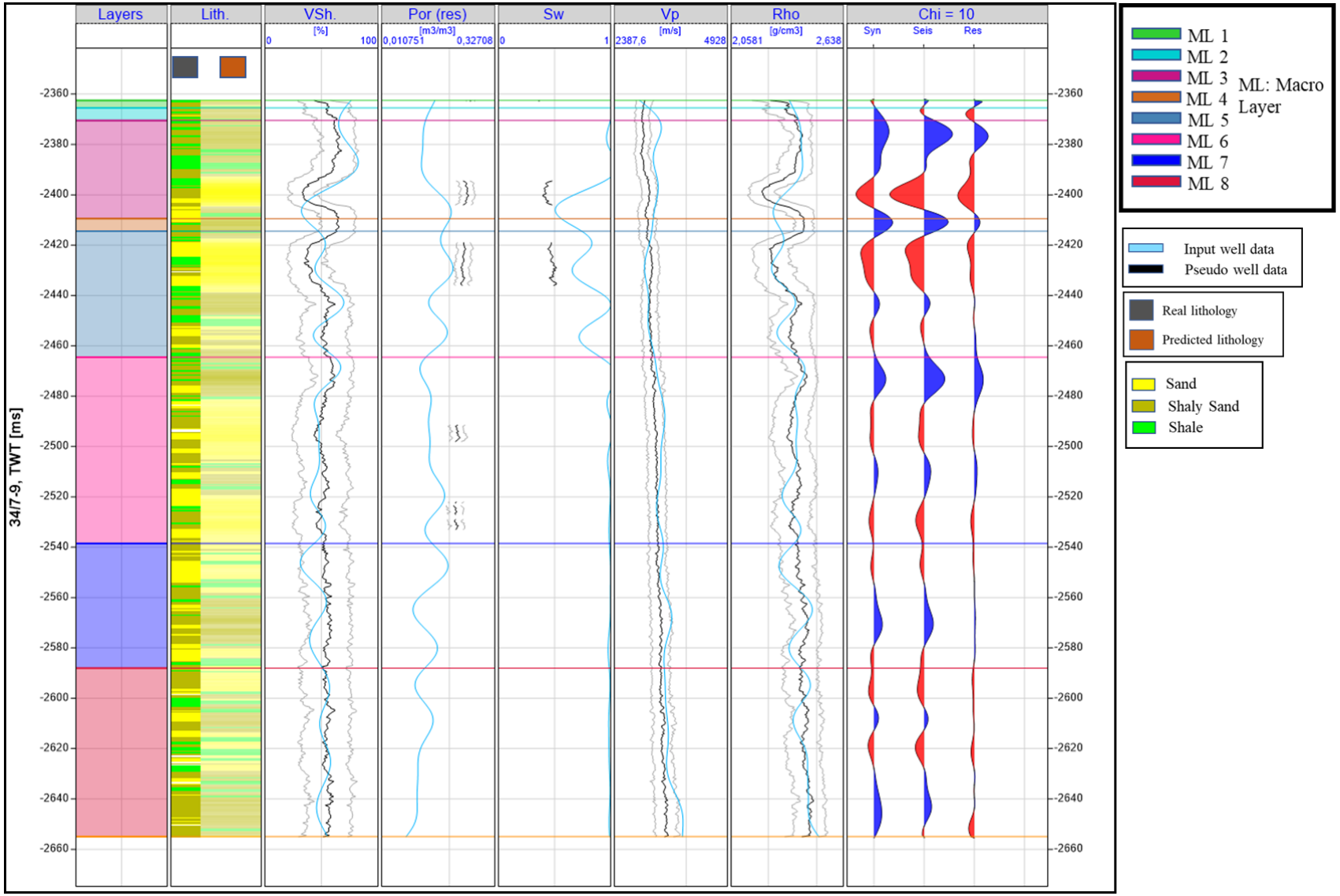

***Figure 6.39**: Properties generated by inverting a trace of EEI (10^0) at the location of well 34/7-9.*

doesn’t match well with the input lithology. ML-2 has a good match, it also contains the fluid contact. The predicted sands are thinner in ML-2 as compared to the input.

- The beginning part of ML-3 has a good match of sand and shale, however towards the end shale is predicted incorrectly in the place of shaly sand.
- ML-3 and ML-4 could not predict the thin layers of sand and shaly sands. The match quality is poor. ML-6 has a decent match of lithology.
- ML-7 could not predict thin layers of sand, whereas ML-8 predicts more thin layers of shale than required.

The results on the prediction of pseudo well logs and synthetics are as follows:

- Vsh log has a poor match in ML-1 and ML-2. The match quality degrades more in ML-3 and ML-4 as the input log is far from the SD lines. ML-6, ML-7 and ML-8 has a considerable match with some misalignments.
- Vp log has some misalignments in ML-2 and ML-3.
- Density log predictions have lower values than required in ML-2, ML-3 and ML-4, and there is a mismatch in ML-6, ML-7 and ML-8.
- Synthetic is not a good match as residual is quite large.

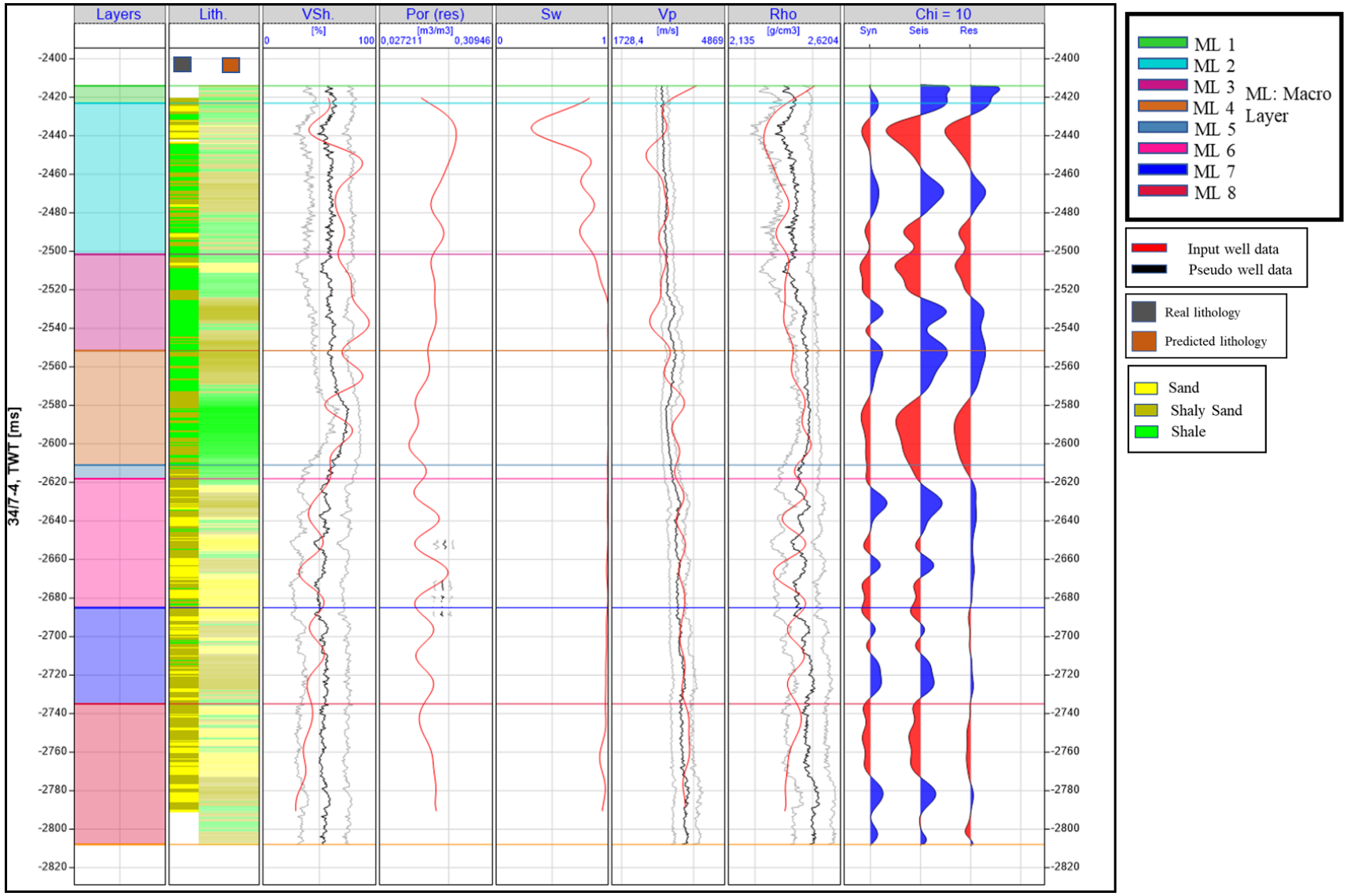

***Figure 6.40**: Properties generated by inverting a trace of EEI (10^0) at the location of well 34/7-4.*

6.5.4.4 Inversion QC using EEI (20^0) at well location of 34/4-9S

Figure 6.41 displays the properties generated by inverting the trace of EEI (20^0) at the well location of well 34/4-9S. The results on the prediction of lithology at the well location in each macrolayer (ML) are as follows:

- ML-2 captures thin layers making the match quality better than that of EEI (10^0).
- The shale prediction match is poor in ML-3, however the sand prediction gets better than that of EEI (10^0).
- Sand prediction in ML-5 is more than required. Sand is predicted in the locations of shaly sand. However, this macrolayer contains fluid contact and the match of sand prediction in the corresponding input sand locations is good.
- ML-6, ML-7 and ML-8 has misalignments and the match is not that good.

The results on the prediction of pseudo well logs and synthetics are as follows:

- Vsh log has poor match in ML-4, ML-6. ML-7 and ML-8 has lower values predicted. The match in ML-5 is quite good.
- Porosity, Vp and Sw log have a good match.
- Vs log has some misalignments in ML-6 and a poor match in ML-4.
- Density log has a poor match in all the macro layers except ML-7 and ML-8, but the values predicted in ML-7 and ML-8 are less than input.
- Synthetic and seismic has amplitude value differences, otherwise it is a good match.

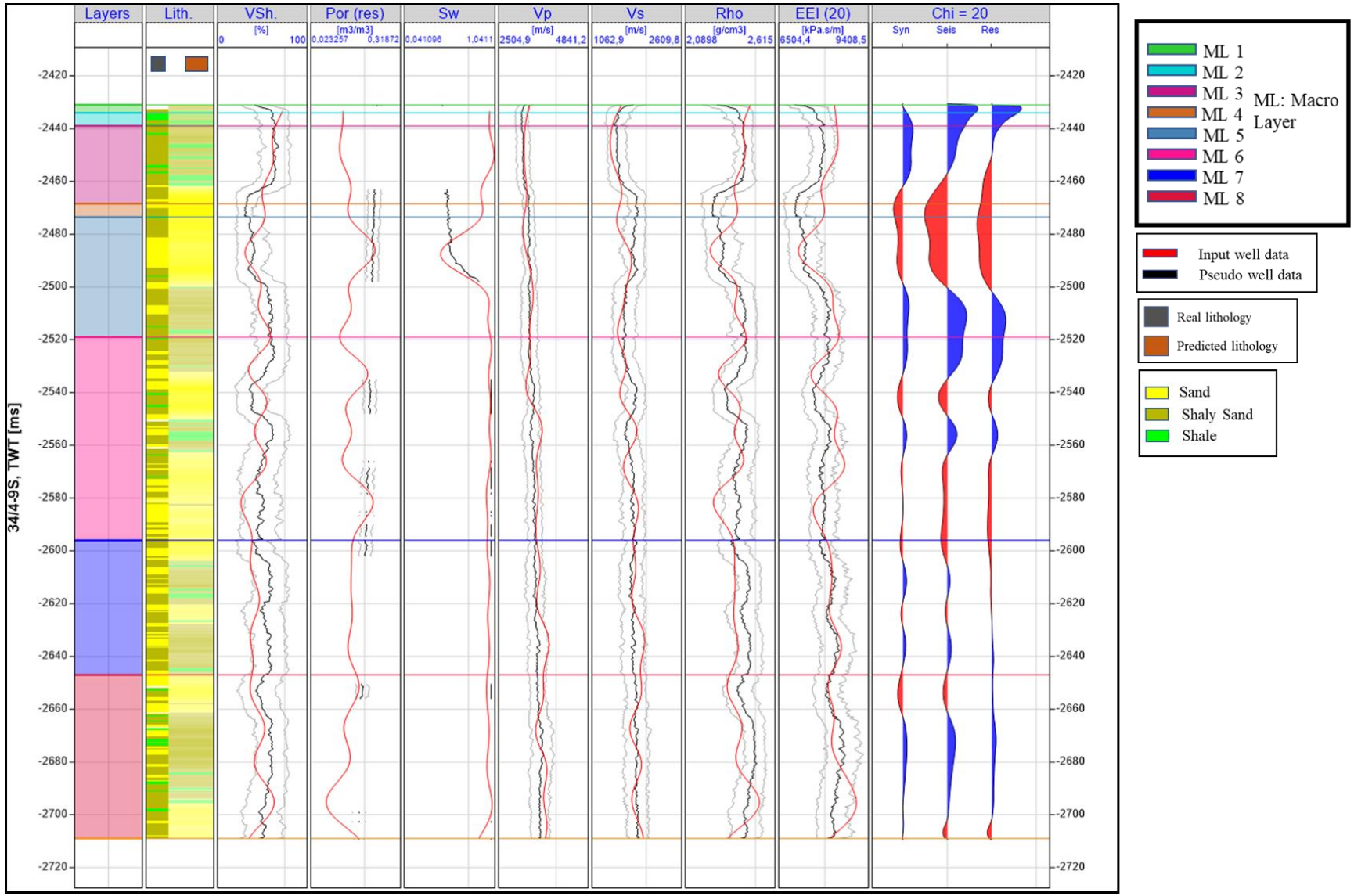

***Figure 6.41**: Properties generated by inverting a trace of EEI (20^0) at the location of well 34/4-9S.*

6.5.4.5 Inversion QC using EEI (20^0) at well location of 34/7-9

Figure 6.42 displays the properties generated by inverting the trace of EEI (20^0) at the well location of well 34/7-9. The results on the prediction of lithology at the well location in each macrolayer (ML) are as follows:

- ML-1 and ML-2 predicts shaly sand and shale respectively and no thin layers are captured thus being a poor match.
- ML-3 contains the fluid contact, and there is a misalignment in the sand prediction. ML-4 and ML-6 have a good match.
- Sand in ML-5 is matched quite well, however less shale is predicted than required. ML-7 and ML-8 has a very good match for sand with some misalignments.

The results on the prediction of pseudo well logs and synthetics are as follows:

- Vsh log has a poor match in ML-1, ML-2 and ML-3. Rest of the macrolayers have a decent match.
- Density log has a good match in all the macrolayers except ML-3 and ML-4.
- Synthetic is matched well with seismic and the residual is also small.

6.5.4.6 Inversion QC using EEI (20^0) at well location of 34/7-4

Figure 6.43 displays the properties generated by inverting the trace of EEI (20^0) at the well location of well 34/7-4. The results on the prediction of lithology at the well location in each macrolayer (ML) are as follows:

- ML-2 contains the fluid contact and it has a very good match.
- ML-3 has a poor match. It predicts sand in place of shale.

- ML-4 has a good match except that it predicts more sand than required. Good match of sand is observed in ML-6.
- ML-7 and ML-8 have misaligned predictions with poor quality of match for sand.

The results on the prediction of pseudo well logs and synthetics are as follows:

- Vsh log has decent match inn ML-1 and ML-2. However, ML-3 and ML-4 have poor match. The volume of shale values predicted in ML-6, ML-7 and ML-8 are lower.
- Vp log has poor match in ML-2 and ML-3 as the input log is out of the SD lines.
- Density log has poor match in ML-3 and some misalignments in ML-5, ML-6 and ML-8.
- Synthetic does not have a good match with the seismic. Huge difference of amplitude is present.

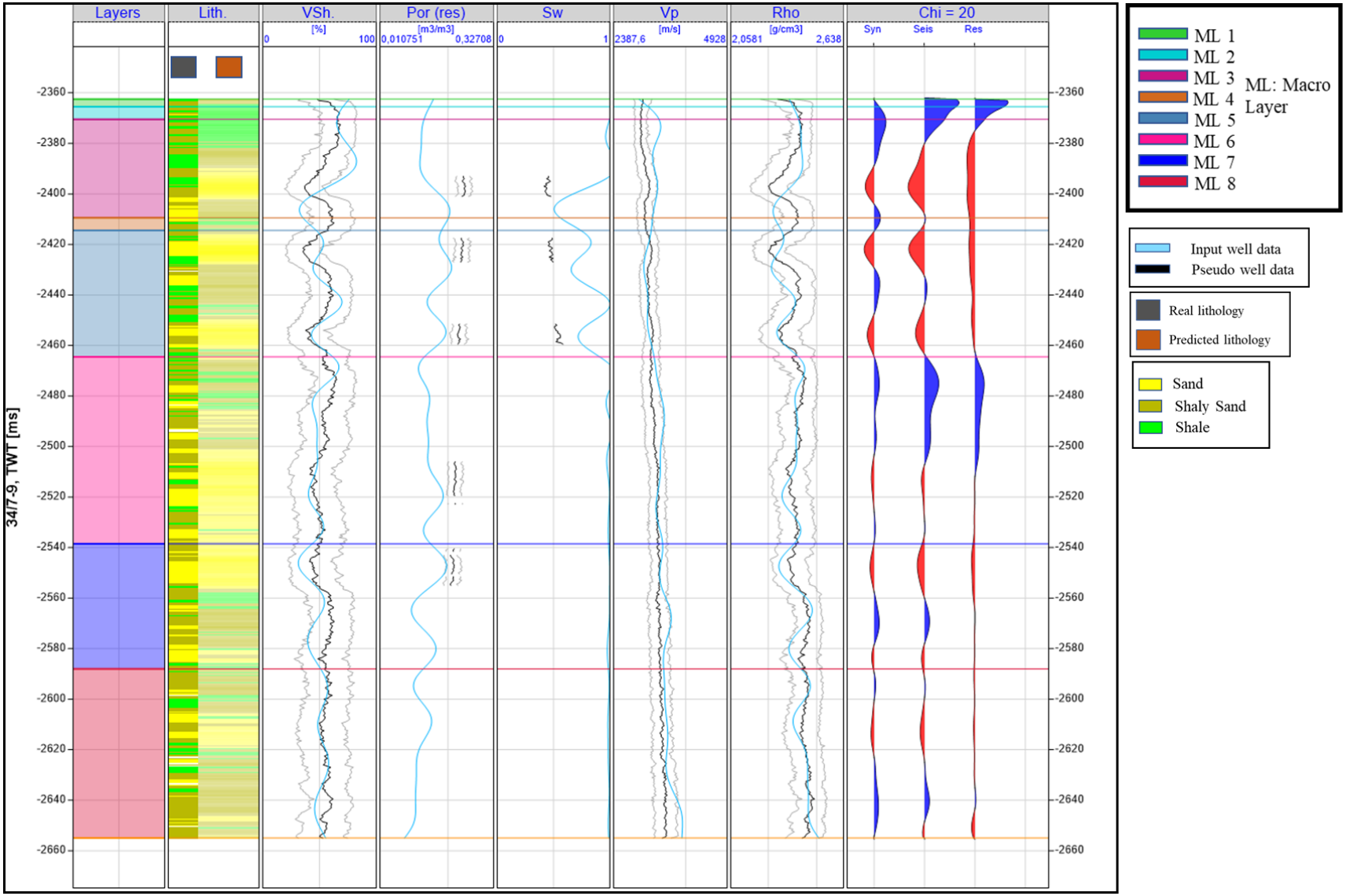

***Figure 6.42**: Properties generated by inverting a trace of EEI (20^0) at the location of well 34/7-9.*

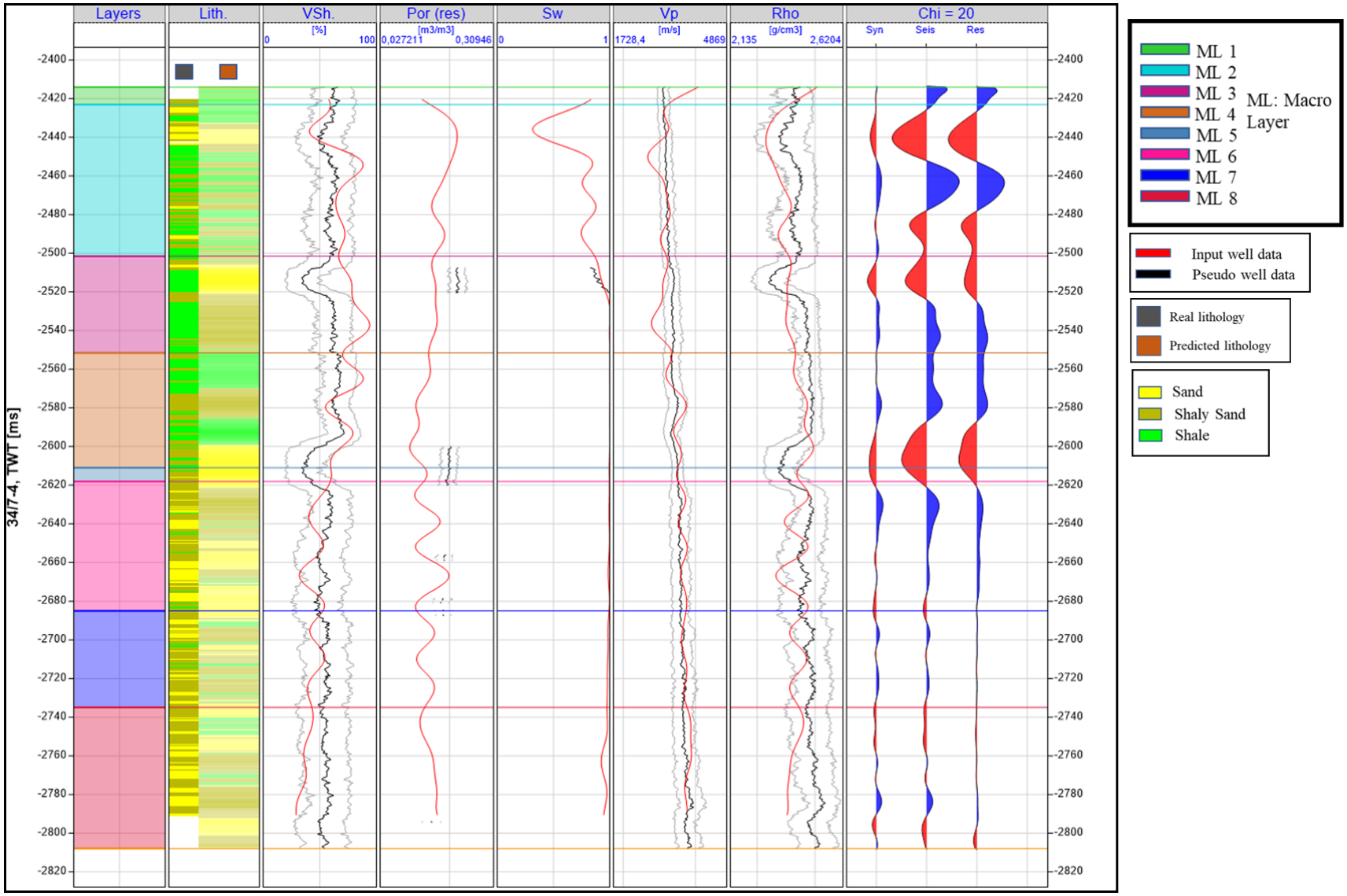

***Figure 6.43**: Properties generated by inverting a trace of EEI (20^0) at the location of well 34/7-4.*

6.5.5 Inversion realization

Inversion realization was initially performed on a 2D line passing through all the wells and then on entire individual EEI cubes separately to obtain several output volumes: Lithofacies probability, Net mean, Porosity and Water saturation. The results regarding the various reservoir properties such as lithofacies probabilities (lithofacies logs of the best matched pseudo wells are used in calculating the probability of each facies at each ample, at each trace location), net mean (1-Vshale, where Vshale is obtained by averaging the reservoir property of the best matched pseudo wells, sample by sample, at each trace location), porosity and water saturation are as follows:

6.5.5.1 Inversion realization of EEI (10^0)

Lithofacies probabilities: Figure 6.44 displays the lithofacies probabilities obtained by inverting a 2D line passing through all the wells. EEI (10^0) was used as the input seismic here. The facies log has also been displayed in the well location to validate the output. ML-2 being thick only in the vicinity of well 34/7-4, predicts a sand layer which is consistent with in the well 34/7-4 but is not continuous and poorly resolved. A layer containing both sand and shale predicted along in the ML-3 boundary is consistent with well 34/7-4 and 34/7-9. In the upper region of ML-4, the shale layer is inconsistent with the facies log of well 34/7-4. The sand layer of ML-4 near well 34/4-9S is consistent. In well 34/7-9, ML-4 is quite thin and is inconsistent with the facies log. The same layer in ML-4 changes facies type from sand to shale possibly due to the presence of fluid contact. The sand layer in ML-5 near the contact is consistent with the facies log of 34/4-9S and 34/7-9. The sand layers predicted in ML-6 are continuous and consistent with well location of 34/4-9S and 34/7-4. ML-7 and ML-8 have discontinuous layers

of different facies near well 34/7-4 but the sand layers in these macrolayers are consistent with well 34/7-9 and 34/4-9S.

Net mean: Figure 6.45 displays the net mean (net to gross) obtained by inverting a 2D line passing through all the wells together with the Vshale log. EEI (10^0) was used as the input seismic here. ML-2 predicts layer of medium net mean poorly resolved near 34/7-4. Low net mean layer in ML-3 is consistent in well 34/7-4 and misaligned in well 34/7-9. In the middle region of ML-4, low net mean layer is inconsistent in well 34/7-4, this low net mean layer in ML-4 transitions swiftly to high net-mean layer above the contact and is consistent with well 34/4-9S. ML-5 has consistent net mean layers in all the wells. ML-6 and ML-7 have consistent and continuous net mean layers in all the wells. The high net mean layer in ML-6 supports the boundary of fluid contact in well 34/7-9. ML-7 and ML-8 have inconsistent and discontinuous net mean layers.

Porosity: Figure 6.46 displays the porosity obtained by inverting a 2D line passing through all the wells together with the porosity log. EEI (10^0) was used as the input seismic here. Porosity is predicted only for sand facies as it is only the reservoir type facies. Changes in porosity based on depth is observed, however no lateral changes are observed. ML-2 doesn't produce any porosity layer inconsistent with well 34/7-4. ML-3 produces low porosity layers inconsistent in well 34/7-4 and 34/7-9, consistent in well 34/7-9. High and low porosity layers in ML-4 is consistent in all the wells. The high porosity layer in ML-5 is very consistent in well 34/4-9S and well 34/7-9, it also delineates the boundary of the contact in both the mentioned wells. Additionally, ML-6 also produces consistent and continuous porosity layers in all the wells. ML-7 and ML-8 have discontinuous and inconsistent porosity layers.

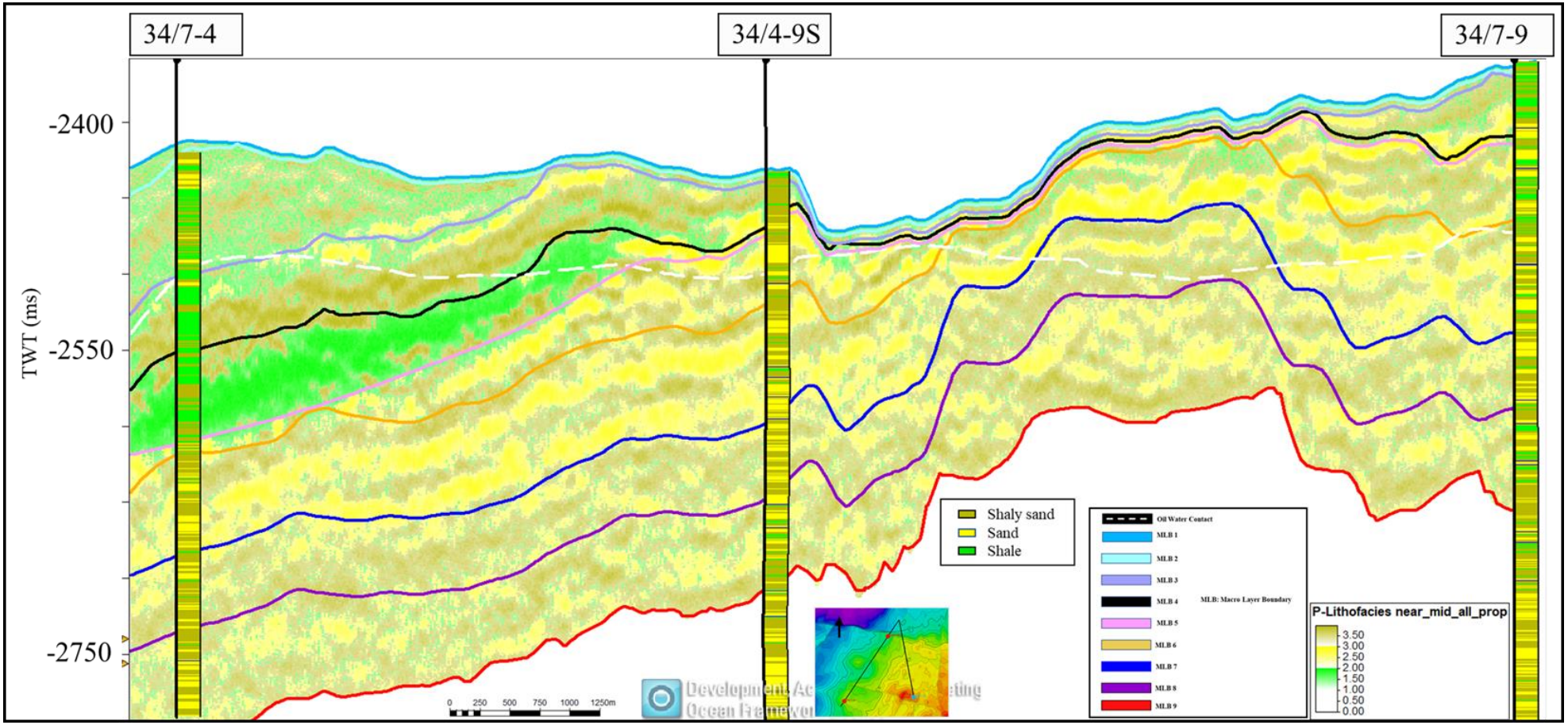

***Figure 6.44**: Lithofacies probabilities generated by inverting a 2D line of EEI (10^0) passing through all the wells together with their facies logs.*

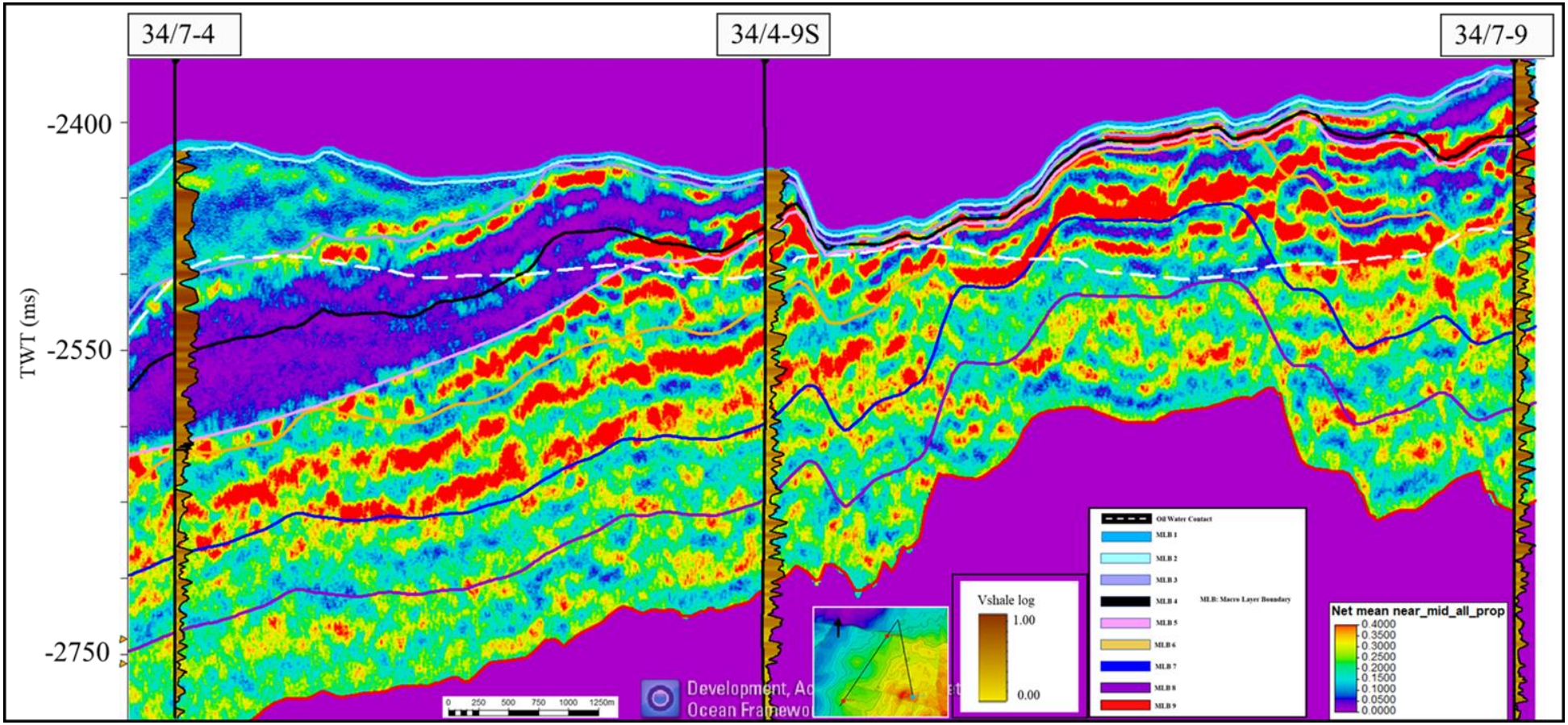

***Figure 6.45**: Net Mean (net to gross) generated by inverting a 2D line of EEI (10^0) passing through all the wells together with their Vsh logs.*

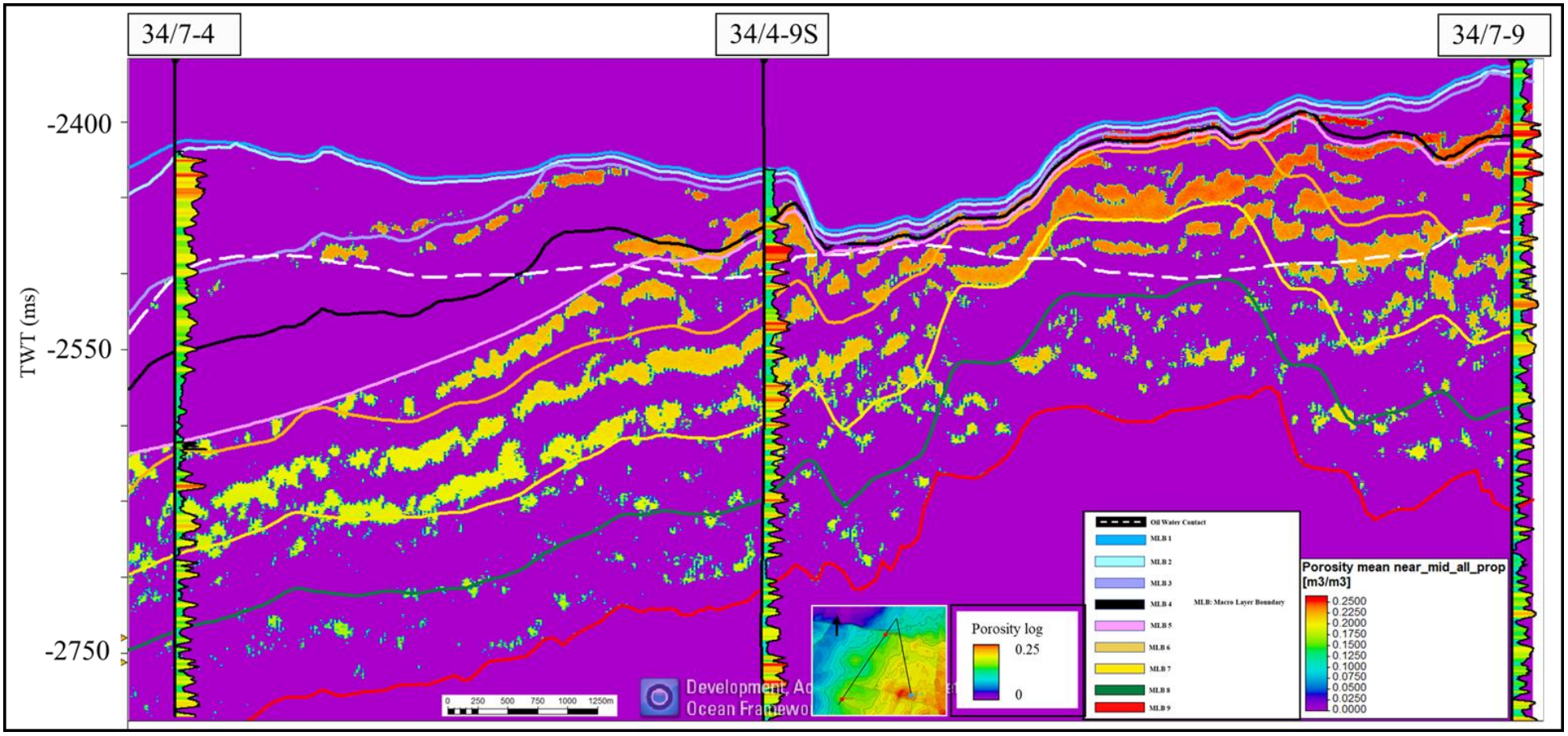

***Figure 6.46**: Porosity generated by inverting a 2D line of EEI (10^0) passing through all the wells together with their porosity logs.*

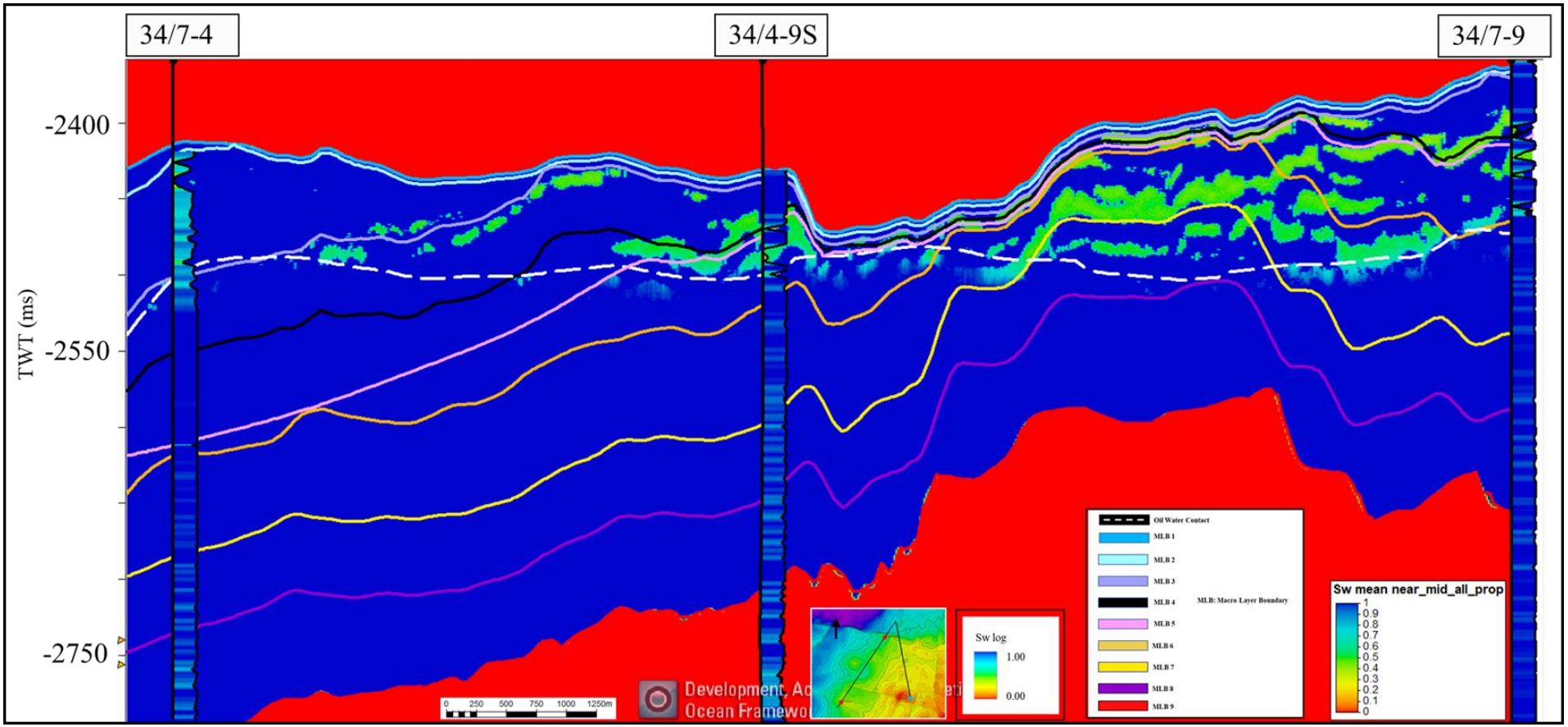

***Figure 6.47**: Water saturation generated by inverting a 2D line of EEI (10^0) passing through all the wells together with their Sw logs.*

Water saturation: Figure 6.47 displays the water saturation (Sw) obtained by inverting a 2D line passing through all the wells together with the water saturation log. EEI (10^0) was used as the input seismic here. The lateral changes in the water saturation layers are not observed. However, the water saturation layers are consistent with the fluid contact in all the wells except 34/7-4. In addition, all the Sw layers are consistent in well 34/4-9S. The Sw layer in ML-5 is consistent with well 34/7-9, although the Sw layer in ML-3 is inconsistent in the same well. The Sw layer in ML-2 and ML-3 is not predicted in well 34/7-4.

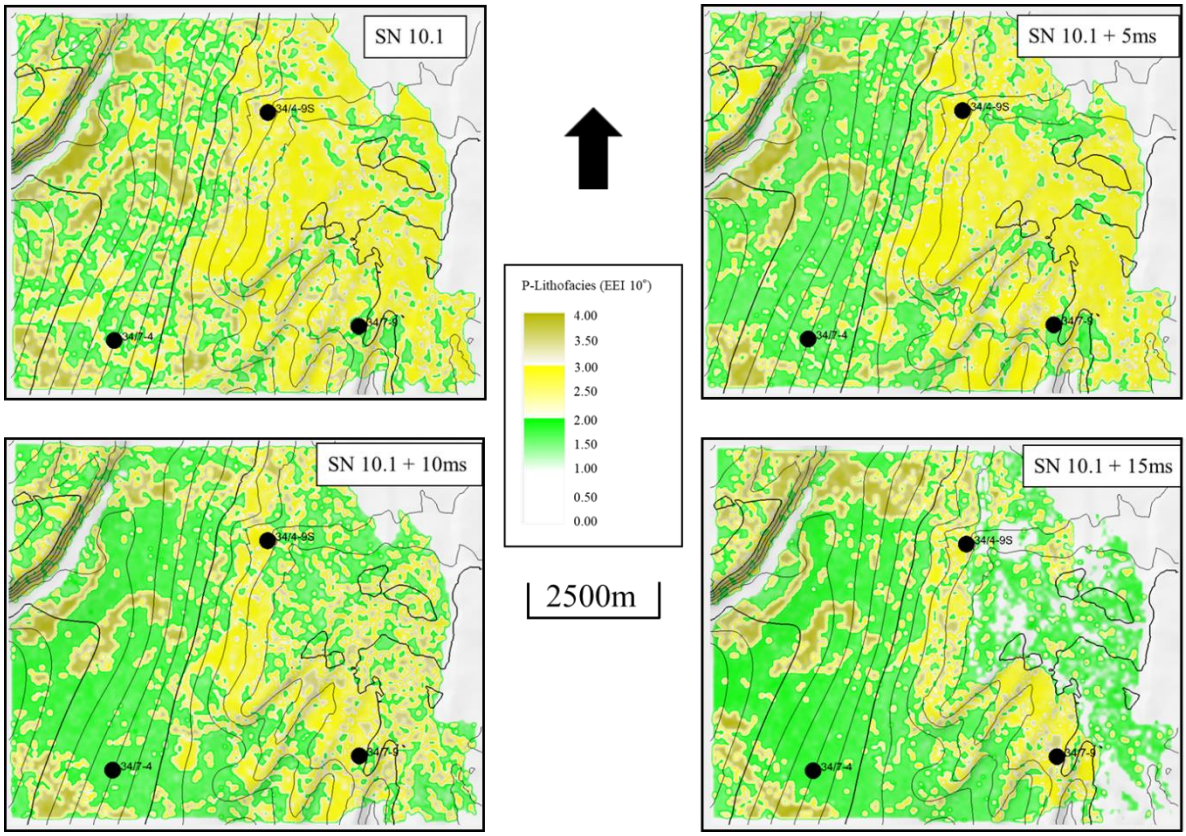

***Figure 6.48**: Lithofacies probability maps of SN10.1 with different offsets generated using EEI (10^0)*

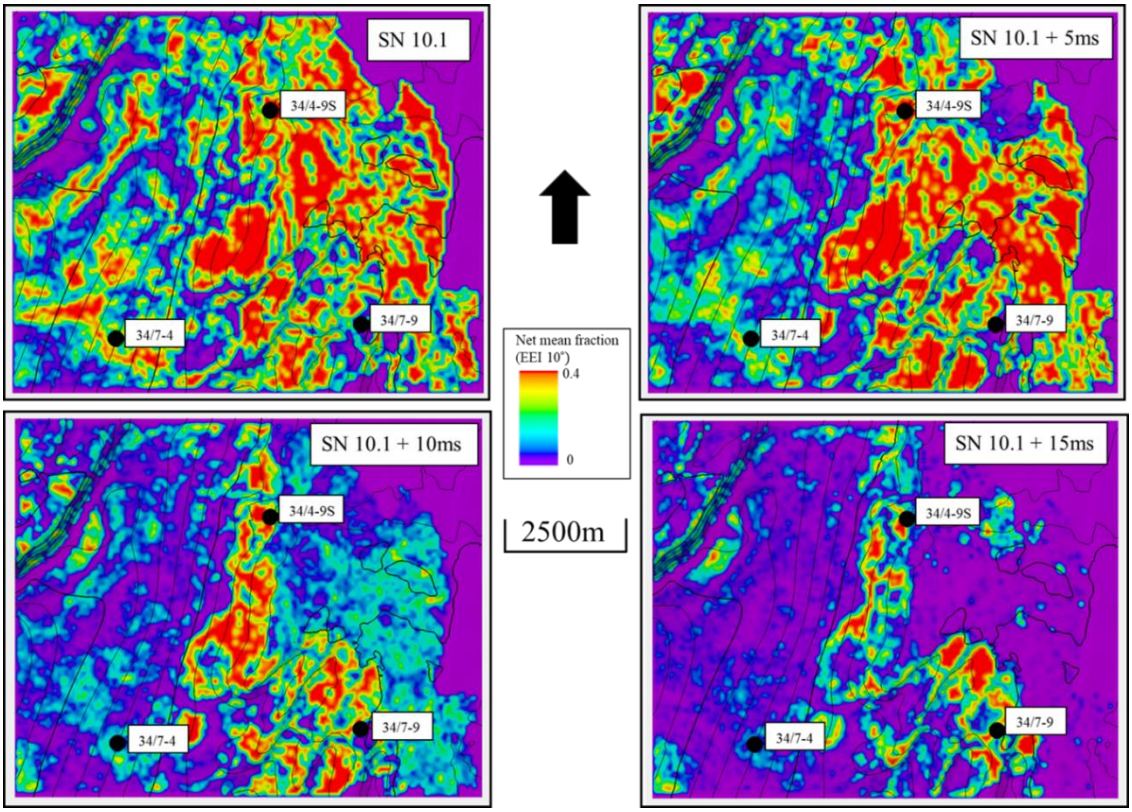

***Figure 6.49**: Net mean maps of SN10.1 with different offsets generated using EEI (10^0)*

6.5.5.2 Inversion realization of EEI (20^0)

Lithofacies probabilities: Figure 6.50 displays the lithofacies probabilities obtained by inverting a 2D line passing through all the wells. EEI (20^0) was used as the input seismic here. The facies log has also been displayed in the well location to validate the output. The sand layer in ML-2 near well 34/7-4 is more consistent and better resolved as compared to the output generated using EEI 10^0. However, sand layer predicted along in the ML-3 boundary becomes inconsistent with well 34/7-4 as compared to the previous corresponding output. In the upper region of ML-4, layers of shale and shaly sand becomes consistent with the facies log of well 34/7-4, although in the lower region a small layer of sand is predicted instead of shaly sand. The sand layer of ML-4 near well 34/4-9S is similarly consistent but more continuous. The change in facies type in

ML-4 sand to shale is gradual as compared to the previous corresponding result. The sand layer in ML-5 near the contact is consistent with the facies log of 34/4-9S and 34/7-9, connectivity of sand layers due to faulting is also captured well in this macrolayer. The sand layers predicted in ML-6, ML-7 and ML-8 have similar response like that of EEI (10^0). In general, the sand layers in this output are more continuous and consistent as compared to the previous output.

Net mean: Figure 6.51 displays the net mean obtained by inverting a 2D line passing through all the wells together with Vshale log. EEI (20^0) was used as the input seismic here. The medium net mean layer in ML-2 is consistent in well 34/7-4 and better resolved as compared to the previous corresponding output. High net mean layer in ML-3 is inconsistent in well 34/7-4 as compared to the previous corresponding output. The same layer in well 34/7-9 is consistent but is misaligned to the input well. In the middle region of ML-4, low net mean layer is inconsistent in well 34/7-4, this low net mean layer in ML-4 changes gradually to high net-mean layer above the contact and is consistent with well 34/4-9S. ML-5, ML-6, ML-7 and ML-8 have similar response to that of generated using EEI (10^0). Altogether, net mean layers in this output are more continuous and the boundary of the layers could be identified.

Porosity: Figure 6.52 displays the porosity obtained by inverting a 2D line passing through all the wells together with porosity log. EEI (20^0) was used as the input seismic here. Similar to the previous corresponding output, changes in porosity based on depth is observed, however no lateral changes are observed. ML-2 produces a porosity layer consistent with well 34/7-4 in comparison to the previous corresponding prediction. ML-3 produces high porosity layers consistent in well 34/7-4 and 34/4-9S, inconsistent

in well 34/7-9. The high porosity layer in ML-5 is very consistent in well 34/4-9S and well 34/7-9, it also matches the boundary of the contact in both the mentioned wells similar to the previous respective output. Rest of the macrolayers have a similar response of porosity as compared to that of EEI (10^0).

Water saturation: Figure 6.53 displays the water saturation (Sw) obtained by inverting a 2D line passing through all the wells together with the water saturation log. EEI (20^0) was used as the input seismic here. The water saturation layers are consistent with the fluid contact in all the wells unlike the previous corresponding output. The results are similar to that of EEI (10^0) in all the macrolayers except in ML-2 and ML-3. The Sw layer in ML-2 and ML-3 is consistent in well 34/7-4.

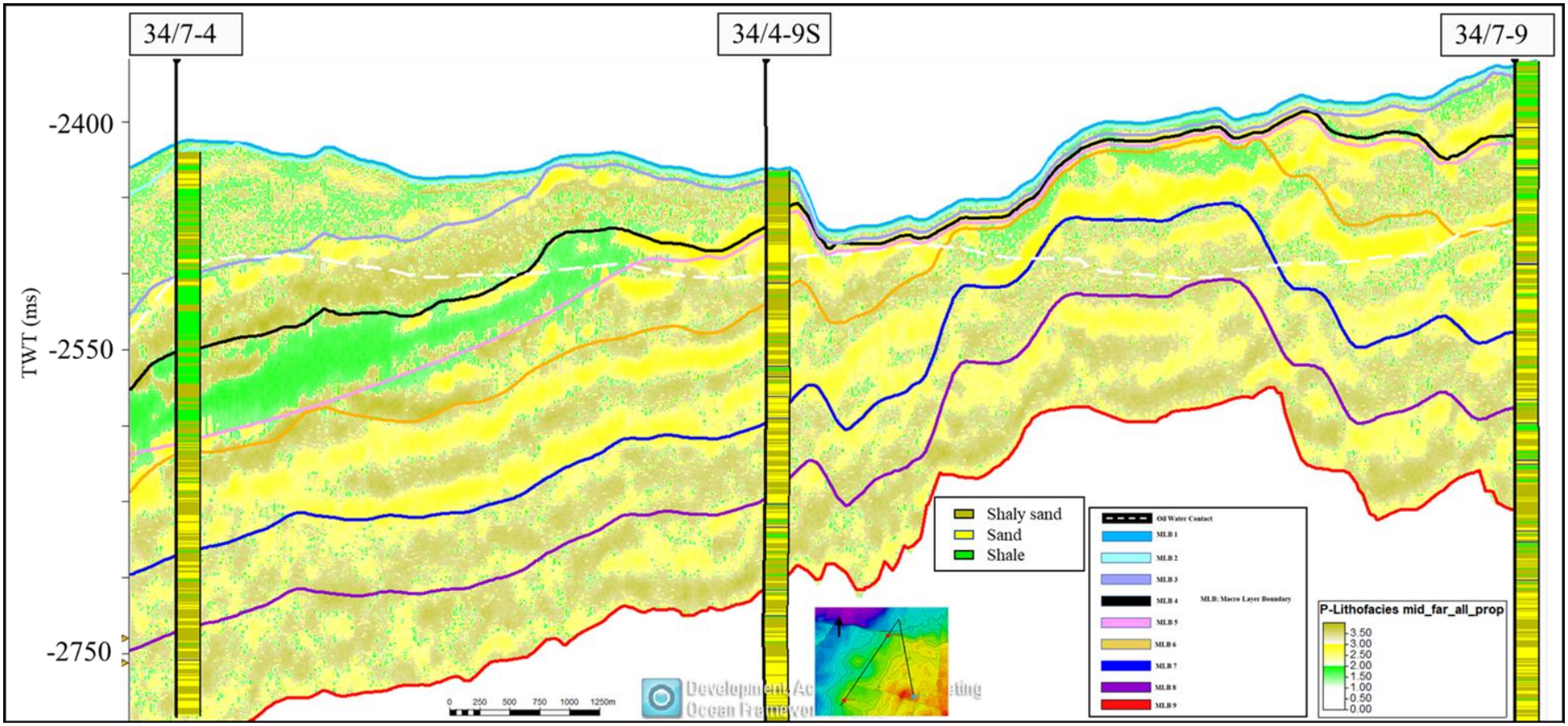

***Figure 6.50**: Lithofacies probabilities generated by inverting a 2D line of EEI (20^0) passing through all the wells together with their facies logs.*

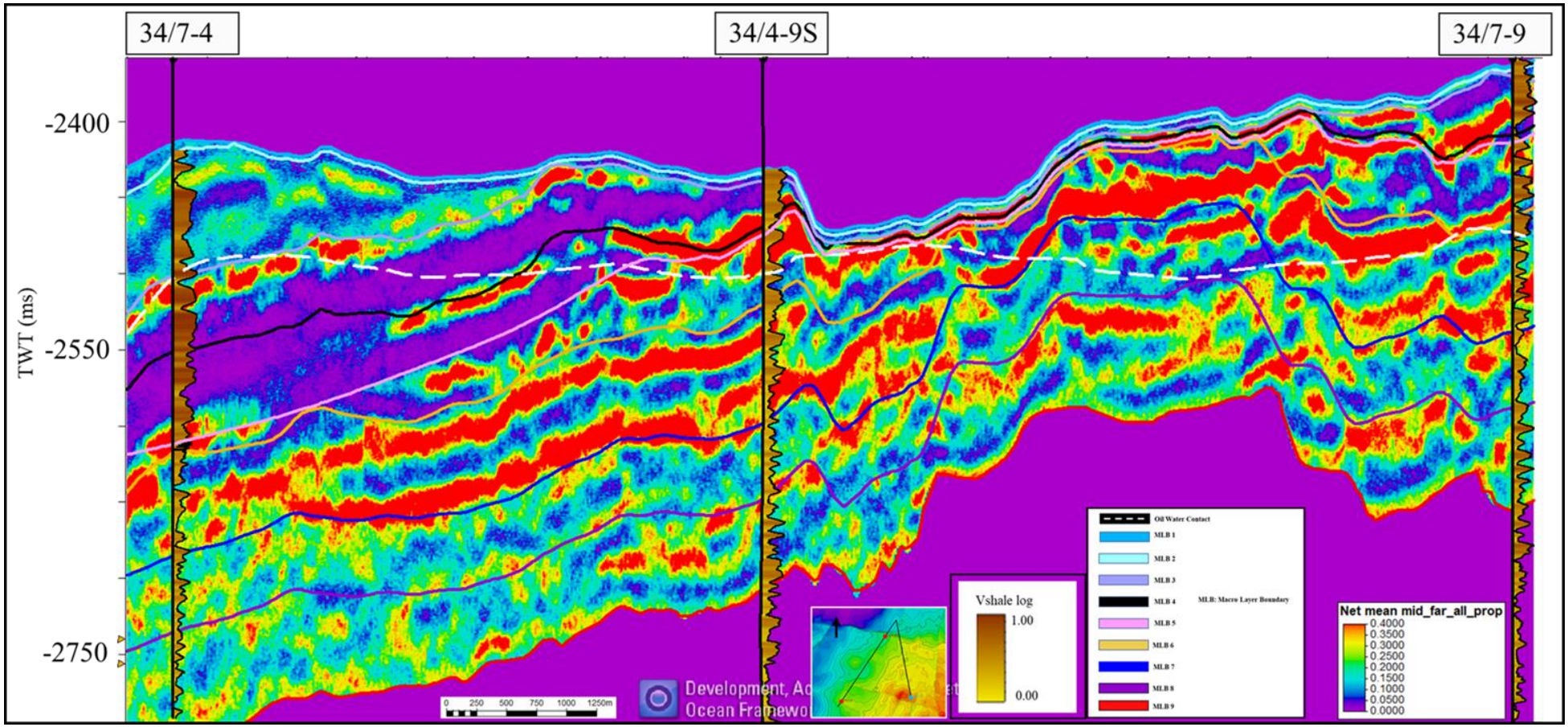

Figure 6.51*: Net Mean (net to gross) generated by inverting a 2D line of EEI (20^0) passing through all the wells together with their Vsh logs.*

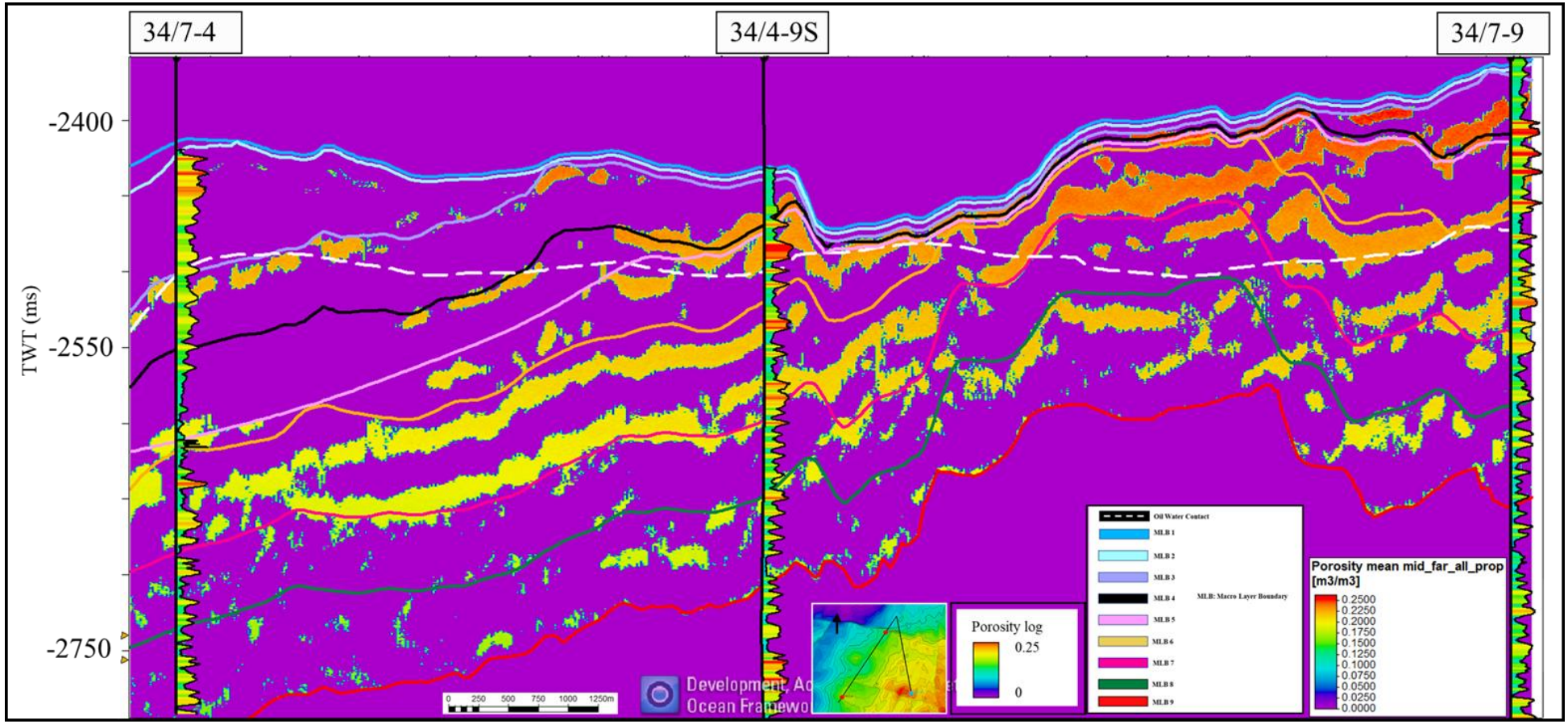

***Figure 6.52**: Porosity generated by inverting a 2D line of EEI (20^0) passing through all the wells together with their porosity logs.*

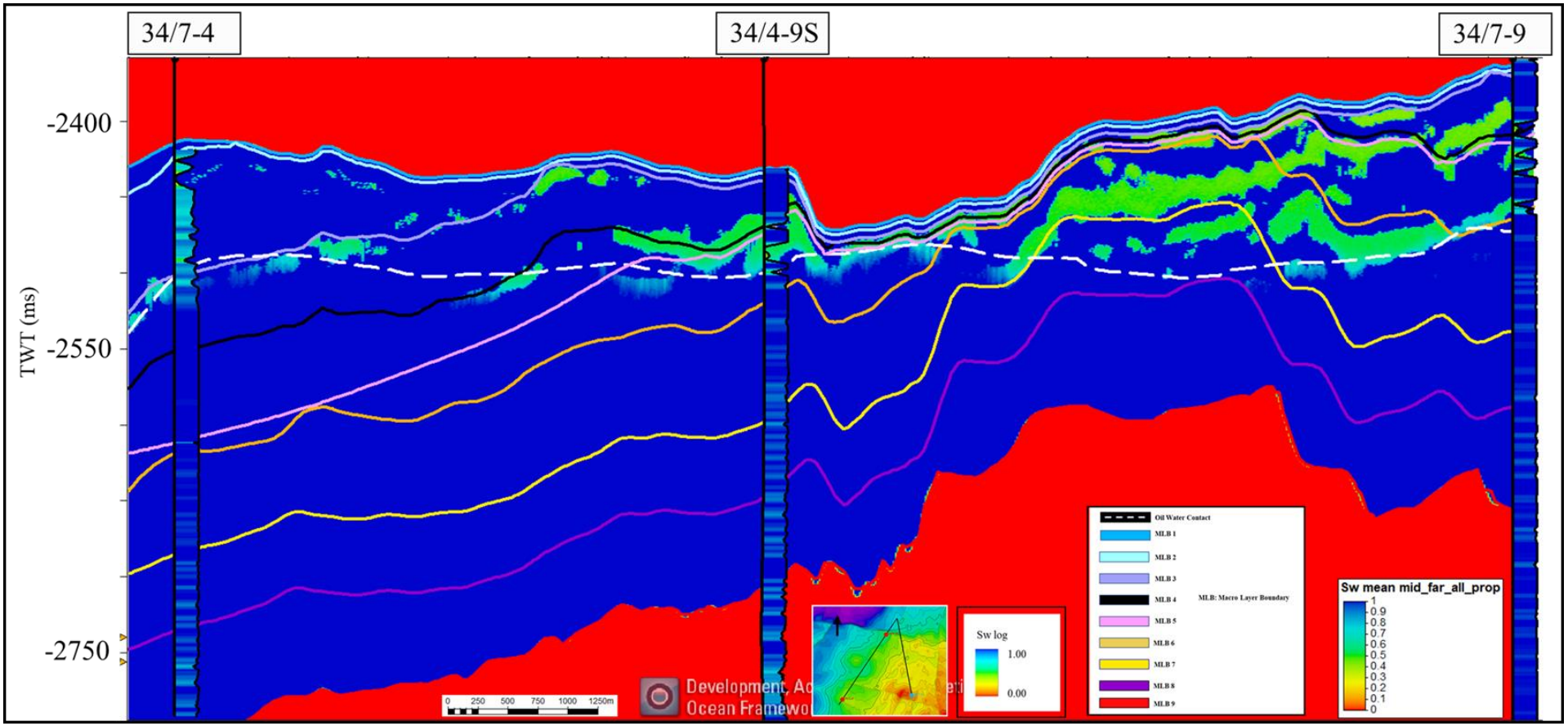

***Figure 6.53**: Water saturation generated by inverting a 2D line of EEI (20^0) passing through all the wells together with their Sw logs.*

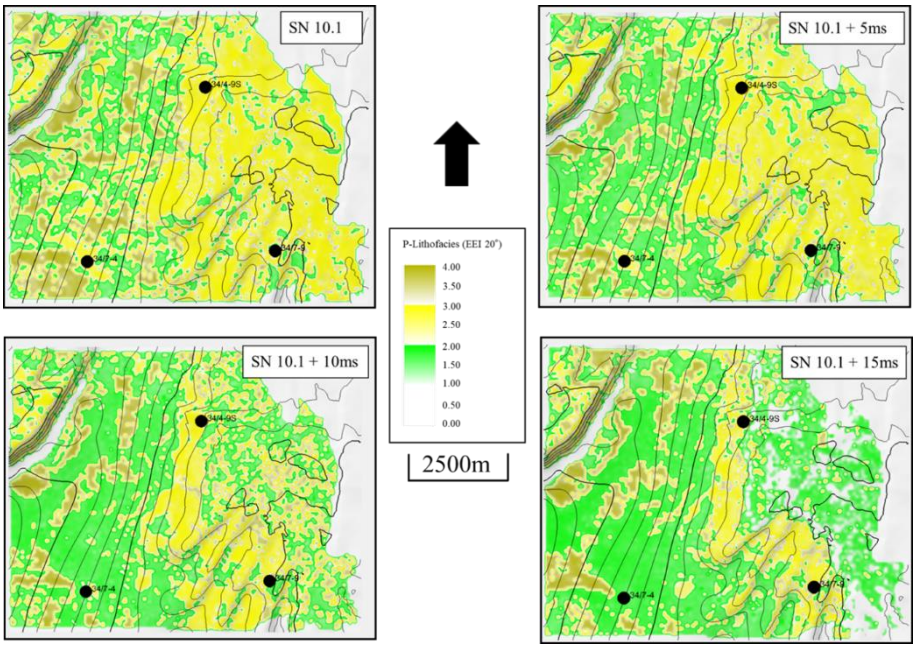

***Figure 6.54**: Lithofacies probability maps of SN10.1 with different offsets generated using EEI (20^0)*

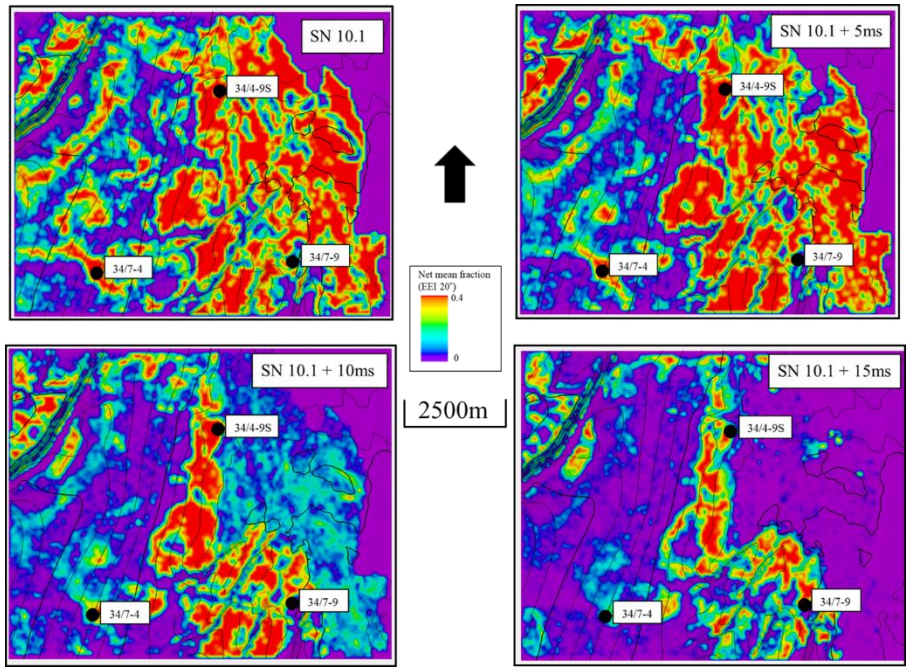

***Figure 6.55**: Net mean maps of SN10.1 with different offsets generated using EEI (20^0)*

7. Discussions

In this chapter, the results of this study are further discussed together with the previous studies conducted on the field. A summary of the results separated by different estimated reservoir properties is given in table 2.2 and table 3.2.

ODiSI was applied to two different EEI volumes and, based on the results obtained (discussed in chapter 6.5.5), the EEI volume from the mid-far stack combination produces better outputs as compared to the near-mid stack combination (Table 6; Table 7). The prior model was identical for both the cases, so the expected reason for different quality of results is the seismic data in near-mid stack. The input data used in ODiSI was EEI stacks. Figure 7.1 and figure 7.2 shows the difference between the raw data (near, mid and far angle stack) and the EEI stacks made from them It clearly shows that the EEI stacks are optimized as compared to the normal stacks. In addition, Figure 6.44 and figure 6.50 also suggest that the output (lithofacies probability) generated for both the combinations has close resemblance to the corresponding input EEI stacks.

In addition to that, certain points regarding the application of ODiSI as an inversion approach are discussed further.

In EEI 20^0 stack output, ODiSI successfully delineated the areas of high net sand within the area of investigation and these are consistent with all the wells (Figure 6.50). A review of the lithofacies and net volume outputs together highlights the extent of a high fraction of sand within the study interval. Potential reservoir can be found in the intervals slightly above SN10.1 zone and is characterized by the interchange between sand and shale (Figure 6.54; figure 6.55). ODiSI also shows presence of thicker, consistent sands above the contact (Figure 6.50).

ODiSI is able to distinguish and represent the presence of faults by committing to the input seismic without any input of spatial control (Figure 6.50; Figure 6.51). Interestingly, the fault interpretation was not a part of ODiSI parametrization process.

The results are consistent with the well data and demonstrate good lateral continuity at seismic resolution. As the process is a one dimensional trace by trace method with no spatial smoothing, lateral continuity assures the stability of the algorithm (Figure 6.50; figure 6.51).

ODiSi also allows for some uncertainity in the seismic data as it is observed that the individual synthetics at the well location are not exact matches to the seismic trace (Figure 6.38-6.40; figure 6.41-6.43). In addition, the synthetic volume created has differences with the input (Figure 7.1; figure 7.2). The conventional model for a seismic trace is signal component plus a noise component. However, post processing the noise is normally both coherent and partially correlated with the signal. Therefore, presence of noise can be a potential cause for amplitude differences. Although, in ODiSI a constant scalar is used for the entire seismic which can also be the cause of the differences as observed in the synthetic as compared to the input seismic.

Hansen and Magnus (1997) suggested that their inversion technique successfully predicted lithologies in the Snorre field but didn't mention anything about the associated uncertainities. Apart from predicting lithology, ODiSI provides a complete overview of the associated uncertainities which makes the results more meaningful.

Dahle et al. (2008) used a relationship between facies and seismic data which was applied in estimating the facies probabilities in the Snorre field. This approach was effective in obtaining facies probabilities. Although, in ODiSI no such relationship is

established, the seismic input and well data is handled separately here. In addition, ODiSI not only provides probability of facies but also volumes of NtG with their corresponding mean and standard deviation volumes. A good overview of the uncertainities in any estimated reservoir property can be obtained using ODiSI.

***Table 6**: Summary of results generated from near-mid combination.*

Seismic: EEI(10°)[Near-Mid]

Wells	Consistency	Continuity	Resolution	
34/7-4	Medium	Low	Low	Lithofacies probabilities
34/4-9S	High	Medium	Medium	
34/7-9	High	Low	Low	
Wells	**Consistency**	**Continuity**	**Resolution**	
34/7-4	Medium	Medium	High	Net to gross (net mean)
34/4-9S	Medium	Medium	Medium	
34/7-9	Medium	Low	Low	
Wells	**Consistency**	**Continuity**	**Resolution**	
34/7-4	Low	Low	Medium	Porosity
34/4-9S	High	High	Low	
34/7-9	Medium	Medium	Low	
Wells	**Consistency**	**Continuity**	**Resolution**	
34/7-4	Low	Low	Medium	Water saturation
34/4-9S	High	Low	Medium	
34/7-9	Medium	Medium	Low	

***Table 7**: Summary of results generated from mid-far combination.*

Seismic: EEI(20°)[Mid-Far]

Wells	Consistency	Continuity	Resolution	
34/7-4	Medium	High	Medium	Lithofacies probabilities
34/4-9S	High	High	High	
34/7-9	Medium	High	High	
Wells	**Consistency**	**Continuity**	**Resolution**	
34/7-4	Medium	High	High	Net to gross (net mean)
34/4-9S	High	High	High	
34/7-9	Low	Medium	Medium	
Wells	**Consistency**	**Continuity**	**Resolution**	
34/7-4	High	Medium	High	Porosity
34/4-9S	High	High	High	
34/7-9	Medium	High	High	
Wells	**Consistency**	**Continuity**	**Resolution**	
34/7-4	Medium	Medium	Medium	Water saturation
34/4-9S	High	High	High	
34/7-9	Medium	High	High	

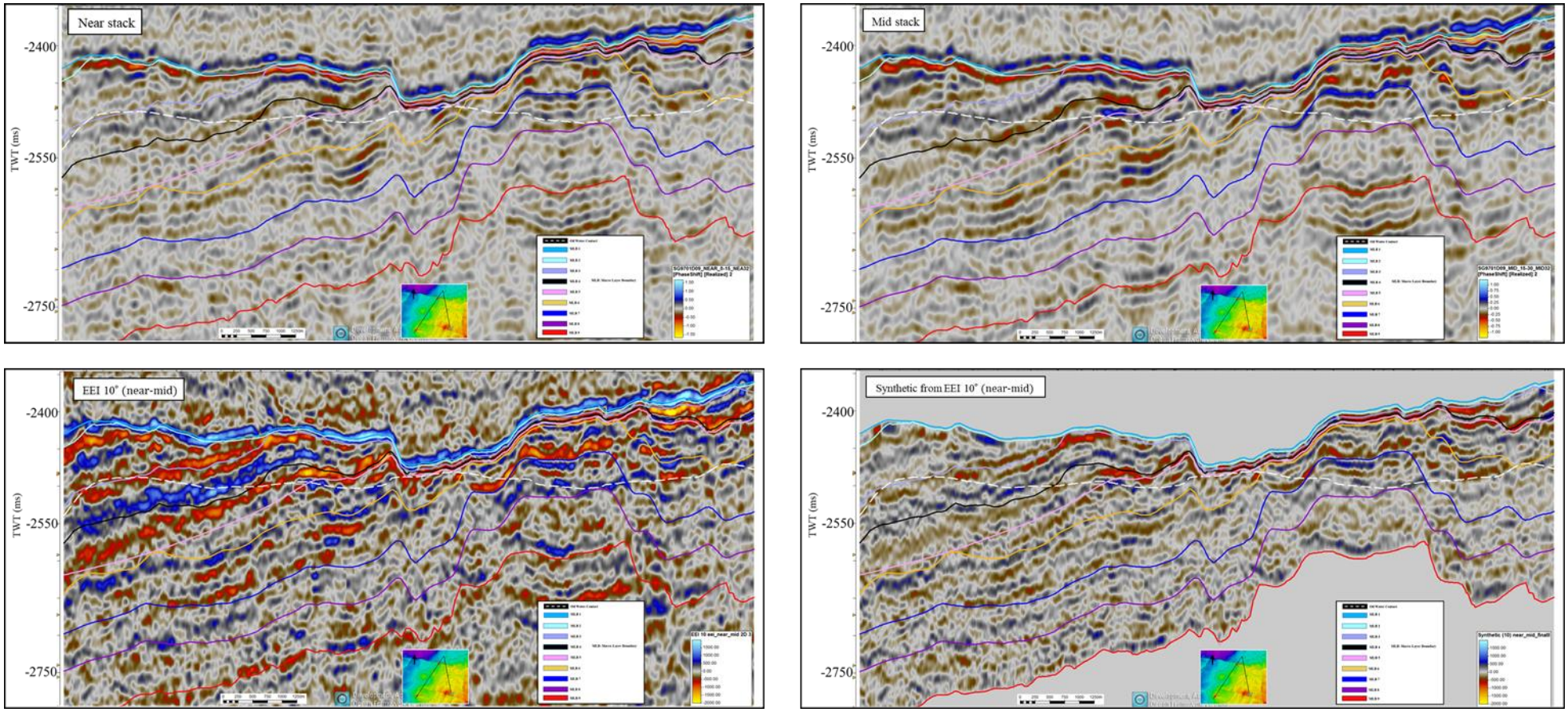

***Figure 7.1**: Near and Mid raw data with its corresponding EEI (10^0) and synthetic.*

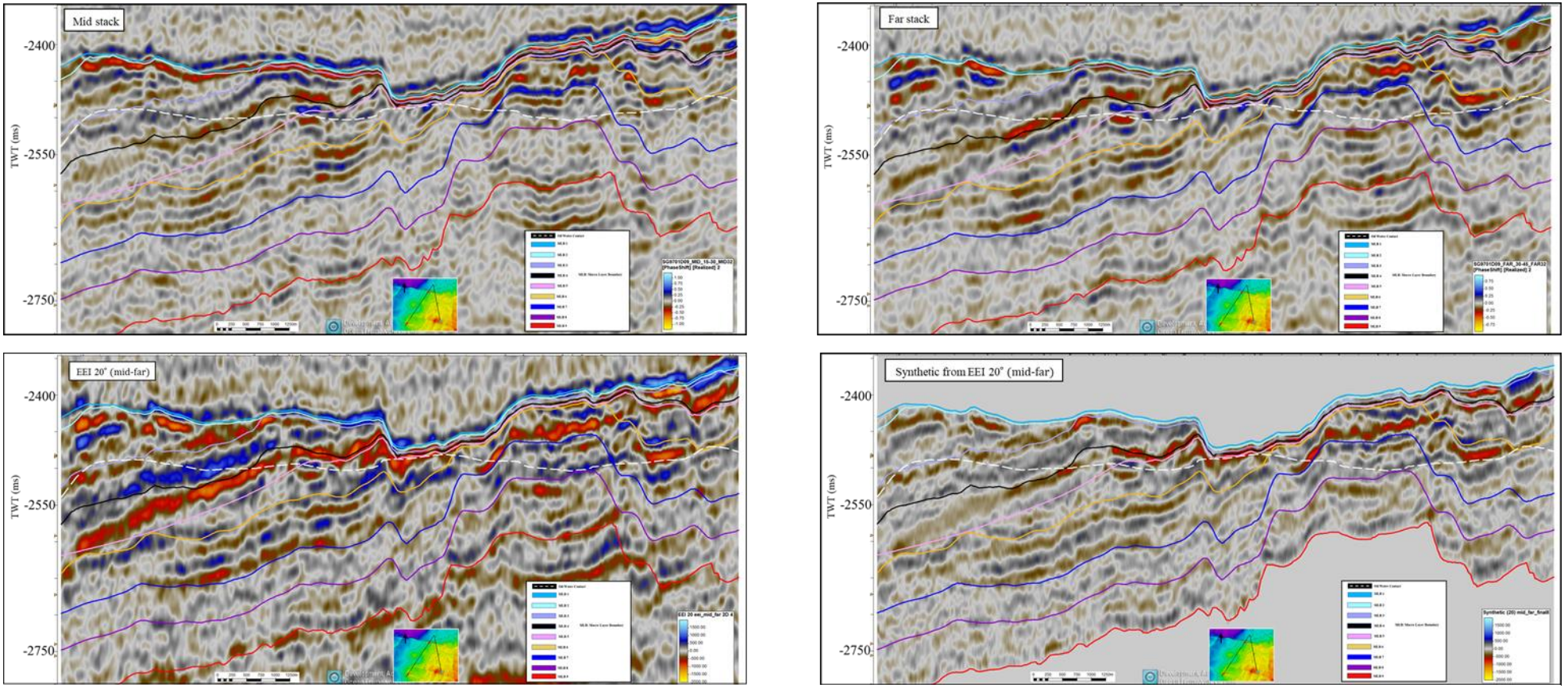

***Figure 7.2**: Mid and far raw data with its corresponding EEI (20) and synthetic.*

8. Conclusion

ODiSI as a process has been implemented to estimate reservoir properties by matching to large number of pseudo wells. Its application has been showed on the Snorre field, North Sea. Two sets of angle stacks were used to perform the study; one from near-mid stack and the other mid-far stack. The mid-far combination has provided better quality outputs as compared to the near-mid.

It has been demonstrated that the pseudo-wells produced results that were laterally stable and consistent with the wells. Based on the results of this study, it can be concluded that pseudo-well trace matching is a workable approach to seismic inversion. It has also been described how the process could capture uncertainties in the estimated reservoir property. This would help the process to be involved in a broader workflow and particularly add constraints for subsequent geostatistical modelling.

9. Future work recommendations:

The following are the future work recommendations for this study:

- Using the Lithofacies probability cube as one of the seismic attributes to infer connectivity between producer and injector well locations in two separate reservoir units and to increase confidence on the facies the well may encounter
- Using angle stacks of suitable angle range and run the inversion using same parametrization.
- Prediction of Vs log using rock physics in the other two wells and thereby including them in the ODiSI parametrization process.
- Running the same ODiSI node on different survey data to see how production history effects the results.
- Using the results obtained to build a facies model with more confidence.

10. References

Aki, K., & Richards, P. G. (1980). Quantitative seismology: W. H. Freeman and Co.

Ayeni, G., Huck, A., & de Groot, P. (2008). Extending reservoir property prediction with pseudo wells. First Break, 26(11), 57-62. doi:10.3997/1365-2397.2008017

Bosch, M., Carvajal, C., Rodrigues, J., Torres, A., Aldana, M., & Sierra, J. (2009). Petrophysical seismic inversion conditioned to well-log data methods and application to a gas reservoir. Geophysics, 74(2), O1-O15. doi:10.1190/1.3043796

Bosch, M., Mukerji, T., & Gonzalez, E. F. (2010). Seismic inversion for reservoir properties combining statistical rock physics and geostatistics; a review. Geophysics, 75(5), 75A165-175A176. doi:10.1190/1.3478209

Buland, A., & Omre, H. (2003). Bayesian linearized AVO inversion. Geophysics, 68(1), 185-198. doi:10.1190/1.1543206

Byberg, A. (2009). Importance of fault communication for predicted Snorre performance. University of Stavanger, Norway,

Caillet, G. (1993). The caprock of the Snorre Field, Norway: a possible leakage by hydraulic fracturing. Marine and Petroleum Geology, 10(1), 42-50. doi:https://doi.org/10.1016/0264-8172(93)90098-D

Castagna, J. P., Batzle, M. L., & Eastwood, R. L. (1985). Relationships between compressional-wave and shear-wave velocities in clastic silicate rocks. Geophysics, 50(4), 571-581. doi:10.1190/1.1441933

Christiansson, P., Faleide, J. I., & Berge, A. M. (2000). Crustal structure in the northern North Sea: An integrated geophysical study. In (Vol. 167, pp. 15-40).

Connolly, P. (1999). Elastic impedance. The Leading Edge, 18(4), 438-452. doi:10.1190/1.1438307

Connolly, P., & O'Brien, M. (2017). Probabilistic seismic inversion using pseudo-wells.

Connolly, P., Wilkins, S., Allen, T., Schurter, G., & Rose-Innes, N. (2005). Fluid and lithology identification using high-resolution 3D seismic data. Petroleum Geology: North-West Europe and Global Perspectives—Proceedings of the 6th Petroleum Geology Conference. In A. G. Doré & B. A. Vining (Eds.), (Vol. 6, pp. 1425-1433): Geological Society of London.

Connolly, P. A., & Hughes, M. J. (2013). Inversion by Trace matching. Paper presented at the 75th EAGE Conference and Exhibition incorporating SPE EUROPEC 2013.

Connolly, P. A., & Hughes, M. J. (2016). Stochastic inversion by matching to large numbers of pseudo-wells. Geophysics, 81(2), M7-M22. doi:10.1190/geo2015-0348.1

Dahl, N., & Solli, T. (1993). The structural evolution of the Snorre Field and surrounding areas. In (Vol. 4, pp. 1159-1166).

de Groot, P. F. M., Bril, A. H., Floris, F. J. T., & Campbell, A. E. (1996). Monte Carlo simulation of wells. Geophysics, 61(3), 631-638. doi:10.1190/1.1443992

Faleide, J. I., BjГ¨rlykke, K., & Gabrielsen, R. H. (2015). Geology of the norwegian continental shelf.

Fatti, J., Smith, G., Vail, P., Strauss, P., & Levitt, P. (1994). Detection Of Gas In Sandstone Reservoirs Using Avo Analysis - A 3-D Seismic Case-History Using The Geostack Technique. Geophysics, 59(9), 1362-1376.

Francis, A. (2006a). Understanding stochastic inversion: Part a (Vol. 24).

Francis, A. (2006b). Understanding stochastic inversion: Part b (Vol. 24).

Frette, L. U. (2018). Quantitative seismic interpretation using converted PS waves: A case study from the Oseberg South Field, North Sea. In N. Cardozo, S. Manral, & L. Schulte (Eds.): University of Stavanger, Norway.

Grana, D., & Della Rossa, E. (2010). Probabilistic petrophysical-properties estimation integrating statistical rock physics with seismic inversion. Geophysics, 75(3), O21-O37. doi:10.1190/1.3386676

Grana, D., Mukerji, T., Dvorkin, J., & Mavko, G. (2012). Stochastic inversion of facies from seismic data based on sequential simulations and probability perturbation method. Geophysics, 77(4), M53-M72. doi:10.1190/geo2011-0417.1

Grant, S. R. (2013). The Impact of Low Frequency Models on Reservoir Property Predictions. Paper presented at the 75th EAGE Conference & Exhibition incorporating SPE EUROPEC 2013.

Grant, S. R., & Dutton, B. J. (2016). Stochastic Inversion by Trace Matching - Reservoir Property Prediction Case Studies. Paper presented at the 78th EAGE Conference and Exhibition 2016.

Gunning, J., & Glinsky, M. E. (2004). Delivery: an open-source model-based Bayesian seismic inversion program. Computers and Geosciences, 30(6), 619-636. doi:10.1016/j.cageo.2003.10.013

Hafez, A., Majoor, F., & Castagna, J. P. (2014). Deepwater reservoir heterogeneity delineation using rock physics and extended elastic impedance inversion: Nile Delta case study. Interpretation, 2(4), T205-T219. doi:10.1190/INT-2014-0056.1

Halland, E. K., Riis, F., Magnus, C., Johansen, W. T., Tappel, I. M., Gjeldvik, I. T., . . . Pham, V. T. H. (2013). CO2 Storage Atlas of the Norwegian Part of the North Sea. In (Vol. 37, pp. 4919-4926).

Hameed, O. (2016). Reservoir Characterization of Triassic and Jurassic sandstones of Snorre Field, the northern North Sea., University of Oslo,

Helland-Hansen, D., Magnus, I., Edvardsen, A., & Hansen, E. (1997). Seismic inversion for reservoir characterization and well planning in the Snorre Field. Leading Edge (Tulsa, OK), 16(3), 269-273. doi:10.1190/1.1437616

Hollander, N. B. (1987). Geology of the Norwegian oil and gas fields (A. M. Spencer Ed.). London.

Horstad, I., Larter, S. R., & Mills, N. (1995). Migration of hydrocarbons in the Tampen Spur area, Norwegian North Sea: A reservoir geochemical evaluation. Geological Society Special Publication, 86(1), 159-183. doi:10.1144/GSL.SP.1995.086.01.12

Jorde, K., & Diesen, G. W. (1990). The Snorre Field: A major field in the northern North Sea. In (Vol. 74, pp. 1517-1518). Tulsa, OK: Tulsa, OK, United States: American Association of Petroleum Geologists.

Kemper, M., & Gunning, J. (2014). Joint Impedance and Facies Inversion-Seismic inversion redefined. First Break, 32(9), 89-95.

Ketzer, J. M., Morad, S., Nystuen, J. P., & De Ros, L. F. (2002). The role of the Cimmerian Unconformity (Early Cretaceous) in the kaolinitization and related reservoir-quality evolution in Triassic sandstones of the Snorre Field, North Sea. International Association of Sedimentologists Special Publications(34), 361-382.

Lancaster, S., & Whitcombe, D. (2000). Fast?track ?coloured? inversion. In SEG Technical Program Expanded Abstracts 2000 (pp. 1572-1575): Society of Exploration Geophysicists.

Lancaster, S. J., & Connolly, P. (2007). Fractal Layering as a Model for Coloured Inversion and Blueing (Vol. 2).

Larsen, A. L., Ulvmoen, M., Omre, H., & Buland, A. (2006). Bayesian lithology-fluid prediction and simulation on the basis of a Markov chain prior model. Geophysics, 71(5), R69-R78. doi:10.1190/1.2245469

Leguijt, J., Michelena, R. J., & Gringarten, E. (2009). Seismically constrained probabilistic reservoir modeling. Leading Edge (Tulsa, OK), 28(12), 1478-1484. doi:10.1190/1.3272703

Lervik, K.-S. (2006). Triassic lithostratigraphy of the northern North Sea basin. Norsk Geologisk Tidsskrift, 86(2), 93-116.

Neves, F. A., Mustafa, H. M., & Rutty, P. M. (2004). Pseudo-gamma ray volume from extended elastic impedance inversion for gas exploration. The Leading Edge, 23(6), 536-540. doi:10.1190/1.1766237

Ng, S., Dahle, P., Hauge, R., & Kolbjørsen, O. (2008). Estimation of facies probabilities on the Snorre field using geostatistical AVA inversion. In SEG Technical Program Expanded Abstracts 2008 (pp. 1971-1975): Society of Exploration Geophysicists.

Norwegian Petroleum Directorate. (2019). Retrieved 24. May. 2019, from NPD Factmaps http://factpages.npd.no/FactPages/default.aspx?culture=en&nav1=field&nav2=PageView|All&nav3=43718

Nystuen, J. P., & Fält, L.-M. (1995). Upper Triassic-Lower Jurassic reservoir rocks in the Tampen Spur area, Norwegian North Sea (Vol. 4).

Nystuen, J. P., Knarud, R., Jorde, K., & Stanley, K. O. (1989). Correlation of Triassic to Lower Jurassic sequences, Snorre Field and adjacent areas, northern North Sea. Paper presented at the Correlation in Hydrocarbon Exploration.

Riise, O., Elgenes, J., M. Frey-Martinez, J., Kjøsnes, Ø., & Buland, A. (2012). Detailed Lithology and Fluid Mapping of the Asterix Gas Discovery Using Bayesian Inversion Methodology.

Rimstad, K., Avseth, P., & Omre, H. (2012). Hierarchical Bayesian lithology/fluid prediction: A North Sea case study. Geophysics, 77(2), B69-B85. doi:10.1190/GEO2011-0202.1

Rolke, W. (1991). Continuous-time Markov processes as a stochastic model for sedimentation. Mathematical Geology, 23(3), 297-304. doi:10.1007/BF02065784

Russell, B. H. (1988). Introduction to Seismic Inversion Methods: Society of Exploration Geophysicists.

Schwarzacher, W. (1975). Sedimentation models and quantitative stratigraphy (Vol. 19). Amsterdam: Elsevier Scientific.

Seldal, M. (2008). Snorre Reservoir Development Plan 2008. Equinor.

Shuey, R. T. (1985). Simplification Of The Zoeppritz Equations. Geophysics, 50(4), 609-614. doi:10.1190/1.1441936

Simm, R., & Bacon, M. (2014). Seismic Amplitude: An Interpreter's Handbook. Cambridge: Cambridge University Press.

Smith, G. C., & Gidlow, P. M. (1987). Weighted Stacking For Rock Property Estimation And Detection Of Gas. Geophysical Prospecting, 35(9), 993-1014. doi:10.1111/j.1365-2478.1987.tb00856.x

Thorgersen, C. (2011). Using VSP to improve interpretation of ocean bottom seismic. The University of Bergen,

Tomasgaard, M. (2018). Time dependent signal of a chalk field: The South Arne Field, Danish North Sea. In N. Cardozo & L. Schulte (Eds.): University of Stavanger, Norway.

Tyiasning, S., & Cooke, D. (2015). A comparison of competing amplitude variation with offset techniques applied to tight gas sand exploration in the Cooper Basin of Australia. Interpretation, 3(3), SZ15-SZ26. doi:10.1190/INT-2014-0262.1

Ulvmoen, M., & Omre, H. (2010). Improved resolution in Bayesian lithology/fluid inversion from prestack seismic data and well observations. Part 1, Methodology. Geophysics, 75(2), R21-R35. doi:10.1190/1.3294570

Vernik, L., & Fisher, D. (2001). Estimation of Net-to-gross From P And S Impedance: Part I - Petrophysics. Paper presented at the 2001 SEG Annual Meeting, San Antonio, Texas.

Vollset, J., & Doré, A. G. (1984). A Revised Triassic and Jurassic lithostratigraphic nomenclature for the Norwegian North Sea. In NPD-bulletin (online), Vol. no. 3.

Wang, Y. (1999). Approximations to the Zoeppritz equations and their use in AVO analysis. Geophysics, 64(6), 1920-1927.

Wang, Z. (2001). Fundamentals of seismic rock physics. Geophysics, 66(2), 398-412. doi:10.1190/1.1444931

Westeng, K., Hope, T. A., & Rasmussen, A. E. (2014). Extended Elastic Impedance - A Time-efficient Workflow From Prestack Seismic Data, Through Rock Physics, To Reservoir Properties. Paper presented at the International Petroleum Technology Conference, Doha, Qatar. https://doi.org/10.2523/IPTC-17566-MS

Whitcombe, D. (2002). Elastic impedance normalization. Geophysics, 67(1), 60-62.

Whitcombe, D. N., Connolly, P. A., Reagan, R. L., & Redshaw, T. C. (2002). Extended elastic impedance for fluid and lithology prediction. Geophysics, 67(1), 63-67. doi:10.1190/1.1451337

Whitcombe, D. N., & Fletcher, J. G. (2001). The AIGI crossplot as an aid to AVO analysis and calibration. In SEG Technical Program Expanded Abstracts 2001 (pp. 219-222): Society of Exploration Geophysicists.

Zheng, Y. Y., & Grant, S. R. (2016). Reservoir Characterization through Integrated Stochastic Inversion. Paper presented at the Abu Dhabi International Petroleum Exhibition & Conference, Abu Dhabi, UAE. https://doi.org/10.2118/183529-MS

Ziegler, P. (1975). The geological evolution of the North Sea area in the tectonic framework of North-Western Europe. NorgesGeol Unders, v. 316, p.1-27.